Eidgenössische Technische Hochschule Zürich
Swiss Federal Institute of Technology Zurich

Technische Universität Wien
Vienna University of Technology

DIPLOMARBEIT

Coupling Superconducting Qubits to Tunable Cavities and Resolving the Lamb Shift in Circuit QED

performed at the
Laboratory for Solid State Physics
ETH Zürich

under supervision of
Prof. Dr. Andreas Wallraff

by
Andreas Fragner

Vienna, July 7th 2008

Abstract

The experiments presented in this thesis were carried out in a solid-state, electrical circuit analog of atomic cavity quantum electrodynamics in which a superconducting charge qubit is strongly coupled to a coherent microwave radiation field contained in a high quality factor transmission line resonator, an architecture that has become to be known as *circuit quantum electrodynamics* (QED) [1, 2, 3]. This system allows studying the interaction of individual photons with an artificial atom and to perform fundamental quantum optics experiments on an electrical chip [4, 5, 6]. Moreover, it has a strong, demonstrated potential for the realization of a solid-state quantum information processor [7, 8, 9].

In the framework of this thesis, two major experiments have been performed in a circuit QED architecture. First, on-chip quantum optics experiments are presented in which we were able to investigate the interaction of matter and light down to the level of single quanta, ultimately reaching the limit where a superconducting qubit dispersively interacts with the pure vacuum fluctuations of the electromagnetic cavity field. Here, the presence of virtual photons manifests itself as a small renormalization of the energy of the qubit in the form of the Lamb shift, which is observed in our experiments for the first time in a solid-state system. The transition from the strong dispersive to the resonant strong interaction is shown as a smooth, continuous overlap of cavity transmission and qubit spectroscopy data, in a region where the Lamb shift turns into the vacuum Rabi splitting of the cavity-qubit superposition states. The enhancement by the cavity leads to maximum observable Lamb shifts of up to 1.4 % relative to the qubit transition frequency. Following the vacuum field measurements, the photon number is subsequently increased. In this regime, some interesting results are presented that allow us to put the Lamb shift in a consistent picture and to resolve individual photon number states of the cavity, as first demonstrated experimentally in Ref. [5]. These measurements reveal that our qubit with limited anharmonicity couples more strongly to the vacuum field than to a single photon inside the cavity.

The second part of this thesis focuses on the development of a novel type of transmission line resonator. As opposed to conventional circuit QED cavities, the resonance frequency of these devices can be dynamically tuned with an external magnetic field [10, 11]. Flux-tunable transmission line resonators are systematically investigated in this thesis, ranging from a thorough theoretical analysis to detailed experimental studies in which the tuning behavior of both the resonance frequency as well as the quality factor is determined. Tuning ranges of up to 2.5 GHz are observed and it is shown that the behavior of the quality factor can be controlled by choosing adequate design parameters. Finally, a first experiment is presented in which we demonstrate the successful strong coupling of a superconducting transmon qubit to a flux-tunable cavity.

Contents

1 Introduction

The origins of quantum mechanics can be traced back to the beginning of the 20th century when the quantized, discrete nature of light and radiation was revealed by Planck and Einstein [12, 13]. Quantum theory has triggered an unprecedented scientific and technological revolution that ultimately led up to today's age of information. It has evolved into one of the most successful physical theories ever developed and is believed to describe our world on both microscopic as well as macroscopic scales. Throughout the last century, we have reached an ever deeper understanding of the quantum nature of our world and the experimental and theoretical advances have made it possible to test quantum theory in its most fundamental forms.

Cavity Quantum Electrodynamics

Cavity quantum electrodynamics (QED) provides a prototype system for studying quantum mechanics on the level of single quanta [14, 15, 16, 17]. By means of coupling an individual quantum two-level system, such as an atom or a quantum bit (*qubit*), to the electromagnetic field contained inside a cavity, the interaction of matter and light can be resolved in a highly controlled fashion, allowing to observe the absorption and emission of single photons - the quantum particles of the electromagnetic field. The field inside a cavity is strongly modified in comparison to free space, which in turn makes it possible to either suppress or strongly enhance the process of spontaneous emission of photons by an atom. In that sense, the quantum nature of the system can be preserved on much longer time scales than in free space. Over the course of the last two decades, cavity QED has become an active area of research in physics and the realization of such systems using atoms and optical mirrors has allowed for a number of hallmark experiments such as the observation of the vacuum Rabi mode splitting [18].
In this thesis we realize a solid-state, electrical circuit analog of atomic cavity QED. Here, an *artificial* atom in the form of a superconducting charge qubit is strongly coupled to the electromagnetic field contained in a coplanar transmission line cavity, an architecture now known as *circuit quantum electrodynamics* [1, 2, 3].

Circuit Quantum Electrodynamics

Circuit QED represents one of the most beautiful examples of how two seemingly disparate scientific disciplines can be connected and combined in an elegant and prosperous way. The quantum-mechanical concepts of atomic cavity QED are applied to superconducting circuits to arrive at an architecture that both serves as a high-accuracy testbed for fundamental quantum theory as well as a promising candidate for the realization of a *quantum information processor*.

Circuit QED equally draws from quantum physics as well as electrical engineering and represents an area of research where science and technology merge. Over the course of the last five years, this novel system has generated a number of fascinating experiments in regimes, that are in fact much more difficult to reach with traditional atomic cavity QED [2, 4, 5, 9, 6, 19]. Building on these recent developments, this thesis presents quantum optics experiments in which we are able to investigate the interaction of matter with the pure quantum fluctuations of the electromagnetic field, ultimately reaching the limit where a superconducting artificial atom solely interacts with the *virtual* photons inside a cavity.

The Quantum Vacuum

Quantum theory predicts that empty space is not truly empty. Even in the absence of any particles or radiation, that is in pure vacuum, virtual particles constantly pop into and out of existence. This effect is commonly referred to as vacuum field fluctuations and can ultimately be traced back to energy-time uncertainty in quantum mechanics. In an electromagnetic field, the presence of virtual photons manifests itself as a small renormalization of the energy of a quantum system, known as the Lamb shift. This shift has been measured for the first time in a hydrogen atom [20] and is now being established as an ultra-high precision test of the theory of quantum electrodynamics [21]. The interaction with these vacuum fluctuations is the underlying reason for the spontaneous emission of radiation from any excited quantum system [22]. Moreover, the same effect also triggers the well-known process of vacuum Rabi oscillations in cavity QED [15, 16, 18]. In this thesis, we present the first experimental observation of the Lamb shift in a solid-state system and resolve the quantum fluctuations of the vacuum field inside a cavity.

Superconducting Quantum Devices

The complete circuit QED architecture is realized in the form of macroscopic superconducting circuits. It is a central theme of this thesis that these quantum electrical circuits can effectively behave in the very same way as real atoms, acting as so-called artificial atoms that can be coupled to electromagnetic fields inside a cavity. Superconductivity represents a prime example of a macroscopic quantum effect. At low temperatures, the electrons in a circuit condense into so-called Cooper pairs which can in turn form a coherent macroscopic state of matter that is described by a single quantum-mechanical wave function. In that sense, it becomes possible for superconducting circuits, consisting of billions of atoms, to essentially behave just like single atoms. In circuit QED, we exploit these effects and harness their potential to realize macroscopic devices that exhibit quantum-mechanical properties. This thesis focuses on two specific superconducting quantum devices, superconducting charge qubits and superconducting quantum interference devices. In particular, the development of a novel type of flux-tunable superconducting cavity is presented, which has the potential to add a new dimension to circuit QED experiments.

Quantum Information Processing

Apart from the fundamental physical interest in studying the interaction of matter and light, circuit QED has a strong, demonstrated potential for the realization of a solid-state *quantum information processor*. Classical information, as it is processed in today's computers, is based on *bits* as elements for doing logic operations. A classical bit can take two values, either zero or one, and can in principle be encoded in any *classical* system that has two distinct states, such as the two sides of a coin or the voltages on a transistor. On the contrary, a *quantum bit* is encoded in a two-state *quantum* system and can not only take the two values zero or one, but in a certain sense it can be in both states simultaneously. This possibility of creating so-called superposition states is the underlying principle of quantum information. A quantum computer is in many ways superior to its classical counterpart. For instance, it can solve certain problems exponentially faster than any classical computer possibly could [23, 24, 25] and the *entanglement* between two qubits can be used to realize communication protocols that are secure by the laws of nature [25, 26]. Today, many different quantum systems have been proposed and implemented as possible candidates for quantum computation, most notably trapped ions [27, 28], electron spins in quantum dots [29, 30], molecular spins in nuclear magnetic resonance [31, 32] and superconducting circuits [33, 34, 35]. In particular, the high degree of control and the long time scales on which quantum states can be preserved in cavity QED systems have made this architecture a natural candidate for testing the concepts of quantum information processing. In the circuit QED analog, the artificial atom is realized in the form of a superconducting charge qubit and the electromagnetic field it couples to represents an effective means for distributing its quantum information content and converting it into so-called *flying* qubits such as photons [9].

Thesis Overview

Throughout this thesis, we will systematically explore the different concepts and regimes of circuit quantum electrodynamics. In the first part, the underlying theory for realizing quantum devices based on so-called *Josephson junctions* is discussed. In particular, we focus on two specific quantum devices, superconducting charge qubits and the superconducting quantum interference device (SQUID), both of which represent essential ingredients for our experiments. In the following, chapter 3 gives a thorough discussion of superconducting coplanar transmission line resonators which we use to realize single-mode coherent microwave radiation fields. Here, we also present the development of a novel type of flux-tunable cavity that incorporates a SQUID-loop at its center. The chapter is then rounded off with a discussion of the micro- and nano-fabrication aspects and the design and operating constraints for these novel devices. In chapter 4, superconducting charge qubits are coupled to microwave cavities to realize a solid-state cavity QED system. First, the general theoretical framework of cavity QED, the so-called *Jaynes-Cummings model*, is discussed and subsequently applied to the specific case of a coupled qubit-resonator system. Two major circuit QED experiments have been carried out in this thesis and are discussed extensively in chapter 5. In this final part, we present an experimental obser-

vation of the Lamb shift in a macroscopic solid-state system where the presence of the virtual photons inside the cavity manifests itself as a small renormalization of the energy of the qubit. In a second experiment, the successful strong coupling of a superconducting charge qubit to a novel flux-tunable cavity is demonstrated and some first preliminary results of our measurements are shown.

2 Quantum Devices

The last two decades saw the development of a vast number of mesoscopic and macroscopic quantum devices spanning quantum amplifiers [36, 37], ultra-sensitive detectors and magnetometers [38] and in particular superconducting quantum bits [33, 34, 35, 39]. In this section, superconducting quantum devices based on so-called Josephson junctions will be systematically investigated, laying the theoretical groundwork for the experiments discussed throughout this thesis.

2.1 Quantum Electrical Circuits

Classical electrical circuits can be consistently described in terms of Lagrangian and Hamiltonian mechanics [40, 41]. In this context, a quantization seems to be naturally at hand and can in fact be carried out with ease. The key problem in this case, however, is more of a conceptual and practical nature. Until the mid 1980s it was not clear if quantum behavior can be observed at all in electrical circuit elements. In conventional, classical circuits, the collective electronic degrees of freedom such as currents or voltages represent classical variables. The charge on a capacitor plate or the voltage drop across a resistor are then given by simple numbers. In a quantum circuit, however, all degrees of freedom have to be treated as operators which do not necessarily commute. The behavior of a quantum integrated circuit is the result of the collective behavior of many particles, i.e. it represents a macroscopic quantum phenomenon [42, 43]. Pioneering experiments [44, 45] and the development of the Caldeira-Leggett formalism [42, 46] consequently demonstrated the applicability of quantum mechanics to macroscopic objects and showed that electrical circuits can indeed exhibit quantum behavior. In the following, the formalism for describing electrical circuits in terms of quantum theory will be briefly reviewed. The quantization procedure discussed here is used repeatedly throughout this thesis and ultimately paves the way for the circuit QED experiments of chapter 5.
A Lagrangian and Hamiltonian description of electrical circuits naturally shows that the charge q and the magnetic flux Φ are canonically conjugate variables. Here, Φ takes the role of position coordinate and q is equivalent to momentum [41, 47, 48]. The voltage u and current i in an electrical circuit are most generally defined by the line integrals

$$u = \int \vec{E} \cdot d\vec{s} \quad , \quad i = \int \vec{B} \cdot d\vec{s} \tag{2.1}$$

where the integration path is to be taken over the length of the specific circuit element under consideration. In general, a circuit can be thought of as a set of different branches (e.g. ca-

pacitors, inductors, etc.) which are connected at nodes [47]. Consequently, we can define the dynamical variables branch charge $q(t)$ and branch flux $\Phi(t)$ as functions of time t

$$q(t) = \int_{-\infty}^{t} i(t')dt' \quad , \quad \Phi(t) = \int_{-\infty}^{t} u(t')dt' \tag{2.2}$$

where the boundary condition $u(t \to -\infty) = i(t \to -\infty) = 0$ was assumed, i.e. no voltages and currents in the circuit at $t = -\infty$. Now for a linear capacitor, the general functional relation of voltage and charge is of the well-known form $u = f(q) = q/C$ with the capacitance C being the inverse proportionality constant. Likewise for inductors we have $i = g(\Phi) = \Phi/L$ with L being the inductance. Furthermore, the electrical power is given by $P = dW/dt = u \cdot i$ and thus we have

$$P_C = \frac{q}{C} i = \frac{q}{C} \frac{\partial q}{\partial t} \qquad \text{and} \qquad P_L = i \frac{\partial \Phi}{\partial t} = \frac{\Phi}{L} \frac{\partial \Phi}{\partial t} \,. \tag{2.3}$$

Hence, it follows that the energies of a linear capacitive and inductive element can be written as

$$E_C(q) = \int_0^q \frac{q'}{C} dq' = \frac{1}{2} C u^2 = \frac{q^2}{2C} \quad , \quad E_L(\Phi) = \int_0^{\Phi} \frac{\Phi'}{L} d\Phi' = \frac{1}{2} L i^2 = \frac{\Phi^2}{2L} \,. \tag{2.4}$$

Given these expressions, it can be easily seen that branch charge and flux represent the canonical momentum and position coordinates fulfilling the Hamilton equations. Using (2.4), the total energy of a conservative circuit is described by the Hamilton function

$$H(q, \Phi) = h_c(q) + h_L(\Phi) = \frac{q^2}{2C} + \frac{\Phi^2}{2L} \,. \tag{2.5}$$

All this means is that the electric field energy is stored in the capacitor while the magnetic field energy is present in the inductor. On the other hand, a resistor dissipates energy and thus it cannot be used as a building block of a quantum circuit, as is discussed in detail below. Now if the two forms of energy in the electric and magnetic fields are transformed into each other, a current flows through the circuit. Hamilton's equations then show explicitly that q and Φ are indeed a pair of canonically conjugate variables

$$\frac{\partial H}{\partial q} = \frac{Q}{C} = -L \frac{\partial I}{\partial t} = -\dot{\Phi} \quad , \quad \frac{\partial H}{\Phi} = \frac{\Phi}{L} = I = q \tag{2.6}$$

$$\to \{\Phi, q\} = 1 \tag{2.7}$$

where Kirchhoff's rules have been used. The quantization of the circuit then follows the standard procedure. Classical variables and Hamilton function are replaced by operators and the quantization prescription

$$\{A, B\} \to \frac{1}{i\hbar}[A, B] \tag{2.8}$$

is imposed (first quantization). Thus the charge and flux operator are defined by

$$[\Phi, q] = i\hbar \quad \to \quad q = i\hbar \frac{\partial}{\partial \phi} \quad , \quad \phi = -i\hbar \frac{\partial}{\partial q} \,. \tag{2.9}$$

The quantum mechanical description of the circuit is then completed by defining the current and voltage operators

$$I = -\frac{1}{L}\frac{\partial \Phi}{\partial x} \quad , \quad V = \frac{q}{C}\,. \tag{2.10}$$

The fundamental problem in observing the quantum nature of integrated circuits lies in the inherent dissipation of energy. In order to preserve quantum coherence, all metallic parts of the circuit must have zero resistance such that electronic signals can be transmitted without loss of energy. This in turn means that the different circuit elements have to be superconducting at the given operating temperature [48]. In practice, quantum circuits are sets of micron- or sub-micron-size elements connected by wires or transmission lines. These superconducting systems can be entirely fabricated using standard techniques from conventional integrated circuit technology.
The discussion so far has shown that the operators describing the collective, macroscopic degrees of freedom can be easily inferred from their classical counterparts without necessarily having to consider each individual particle in the circuit. Conceptually, this can be understood in terms of the macroscopic quantum model.

2.2 Macroscopic Quantum Model

The quantum-mechanical behavior of individual microscopic particles is governed by the Schrödinger equation $i\hbar(\partial/\partial t)\,|\Psi\rangle = \mathbf{H}\,|\Psi\rangle$. Although each particle in a given system behaves quantum-mechanically, this behavior is in general not observed on a macroscopic scale: The quantum nature of the individual particles is usually averaged out since macroscopic quantities involve a summation over a broad distribution of quantum states. If, however, all particles in a system are described by the *same* state (δ-distributed), the quantum nature of the individual particles can become evident even on macroscopic scales. Two prominent examples of where this is the case are Bose-Einstein condensates and superconductors. In these systems, the ensemble of all particles can be described by a *single* wavefunction $|\Psi(\vec{r}, t)\rangle$ involving macroscopic variables such as the phase $\theta(\vec{r}, t)$. Using the Schrödinger equation and its general solution $|\Psi\rangle = \Psi_0 \exp[i\theta(\vec{r}, t)]$, the equation of motion for the phase of a wavefunction is written as

$$\hbar\frac{\partial}{\partial t}\theta(\vec{r}, t) = -E \tag{2.11}$$

where Ψ_0 was assumed to be stationary. In the case of fermions, all particles by definition have different energies so the time-evolution of the phase also differs from particle to particle. Thus, on average the macroscopic phase vanishes. For instance, in a normal conducting metal, no macroscopic quantum effects are observed since the charge carriers are simple electrons obeying Fermi-Dirac statistics. In the superconducting state, however, these electrons condense into Cooper pairs which obey Bose-Einstein statistics. In that case, all particles have the same energy in the ground state and thus according to (2.11) all phases evolve identically in time. This gives rise to a so-called *phase-locked state* in which the ensemble of all Cooper pairs is

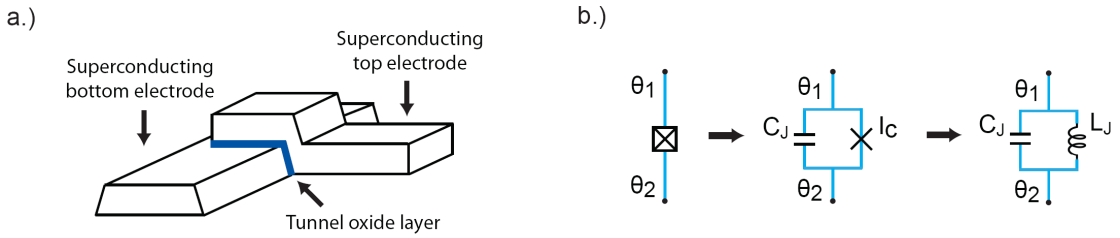

Figure 2.1: (a) Sketch of a Josephson tunnel junction. (b) Josephson junction viewed as a circuit element.

described by a *single* wavefunction

$$|\Psi\rangle = \sqrt{n_s(\vec{r},t)}e^{i\theta(\vec{r},t)} \tag{2.12}$$

where $n_s(\vec{r},t)$ denotes the Cooper pair density. Therefore, a superconducting piece of metal can be described by the macroscopic quantum variable $\theta(\vec{r},t)$ and the local charge density $\rho_s(\vec{r},t) = (-2e)n_s(\vec{r},t)$. A corresponding supercurrent density, fulfilling the continuity equation, then follows directly from the Schrödinger equation [49]. On a macroscopic scale, this collective quantized behavior manifests itself via the dependence of the current and voltage on the phase and charge density, which leads to coherent macroscopic effects such as flux quantization and the Josephson effect.

2.3 Josephson Junction Theory

A Josephson junction consists of two superconductors connected by a thin insulating barrier, as depicted schematically in Fig. 2.1. If the barrier is sufficiently thin, the macroscopic wavefunctions of both superconductors start to overlap and they form a weakly-coupled system in which Cooper pairs can tunnel coherently from one side to the other with a non-vanishing probability. The fundamental theory describing such a superconductor-insulator-superconductor system was first given by Brian Josephson in 1962 [50] and was closely followed by the first experimental confirmation in Ref. [51].

Josephson Relations

The two fundamental equations governing the behavior of a Josephson element relate both the voltage $V(t)$ across and the current $I_s(t)$ through the junction to the phase difference of the macroscopic wavefunctions on the superconducting electrodes of the junction. The supercurrent $I_s(t)$ flowing through a junction is given by the first Josephson equation, the current-phase relation [49, 52]

$$I_s(t) = I_c \sin\phi(t) \quad , \quad j_s(t) = j_c \sin\phi(t) \tag{2.13}$$

where I_c is the maximum current that can be carried by the supercurrent, the so-called critical current of the junction, and j_s, j_c are the corresponding current densities. The supercurrent is generated by the coherent, gauge-invariant phase difference of the two opposite junction electrodes

$$\phi(\vec{r}, t) = \theta_2(\vec{r}, t) - \theta_1(\vec{r}, t) - \frac{2\pi}{\Phi_0} \int_1^2 \vec{A}(\vec{r}, t) dl \tag{2.14}$$

where $\theta_i(\vec{r}, t)$ denotes the phase of the macroscopic wavefunction describing the Cooper pair condensate in electrode i. The vector potential $\vec{A}(\vec{r}, t)$ accounts for external magnetic fields, integrated over the junction in the direction of the current flow. Equation (2.13) describes the tunneling of Cooper pairs from one electrode to the other, with I_s being the corresponding tunneling current. Note that this relation can be directly derived from first principles [50, 52]. An approximate expression for the critical current I_c based on a microscopic model is given by the Ambegaokar-Baratoff-relation [53]

$$I_c = \frac{\pi}{2e} \frac{\Delta(T)}{R_n} \tanh\left(\frac{\Delta(T)}{2k_B T}\right) \tag{2.15}$$

which connects the critical current to the temperature-dependent BCS energy gap between ground and excited state $\Delta(T)$ and the tunnel resistance in the normal state R_n. The voltage across the junction is related to the change in phase difference through the second Josephson equation, the voltage-phase relation

$$\frac{d\phi}{dt} = \frac{2\pi}{\Phi_0} V(t) \tag{2.16}$$

where $\Phi_0 = h/2e$ is the flux quantum. All of the intriguing phenomena in Josephson elements follow directly from the basic relations (2.13) and (2.16). The first Josephson effect, described by (2.13), implies that there is a current flowing across the junction even without external applied voltage. Furthermore, Eq. (2.16) shows that the phase difference $\phi(t)$ will change in time if there is a non-vanishing voltage drop across the junction, which is referred to as the second Josephson effect. As can be inferred from the two Josephson relations, the supercurrent is then an oscillating function of the voltage with period $T = \Phi_0/2\pi$.

In terms of energy, a Josephson junction is characterized by the kinetic energy of the Cooper pairs, the Josephson coupling or tunneling energy $E_J = \int dt V \cdot I$, as well as the potential energy capacitvely stored in the junction, the charging energy $E_C = CV^2/2$. Note that E_C is an electrostatic energy while E_J is a magnetic energy (see also section 2.1). Using the first and second Josephson relations, these are written as

$$E_J(\phi) = E_{J0}(1 - \cos\phi) \quad , \quad E_C = 4E_{C0}N^2 \tag{2.17}$$

$$E_{J0} = \frac{\Phi_0 I_c}{2\pi} \quad , \quad E_{C0} = \frac{e^2}{2C} \tag{2.18}$$

where C denotes the junction capacitance and N the number of Cooper pairs on the superconducting electrodes. As mentioned above, the kinetic energy E_J resulting from the first Josephson relation describes the tunneling of Cooper pairs across the insulating barrier. E_{J0} is the energy

required for such a transfer of a Cooper pair and E_J can be regarded as a kinetic energy term, very much like in the quantum description of solid-state lattices [54]. This peculiar connection will become even more obvious in section 2.5, where the tunneling process is discussed in terms of a tight-binding model. Note that the formulation of a tunneling process in terms of phase differences is completely equivalent to a description using wavefunction overlaps [52].

Electrical Circuit Model

From the viewpoint of an electrical circuit element, as illustrated in Fig. 2.1b, the Josephson junction is essentially a nonlinear, non-dissipative circuit element consisting of a capacitance C_J and the non-linear Josephson inductance L_J. Applying a bias current I, two fundamental cases can be distinguished in a Josephson element. In the so-called zero-voltage state $I < I_c$, the applied current I does not exceed the maximum critical current I_c of the junction and the total current flowing through is just the supercurrent given by (2.13). Since there is no resistance in that case, there is also no voltage drop across the junction, hence zero-voltage state. If however the bias current through a Josephson junction exceeds the maximum supercurrent, i.e the critical current I_c, it can no longer be carried completely by I_s, which is referred to as the voltage state. Taking the time derivative of (2.13) and plugging in (2.16) gives

$$\frac{dI_s}{dt} = I_c \cos\phi \frac{2\pi}{\Phi_0} V(t). \tag{2.19}$$

Using $V = L(dI/dt)$, the *nonlinear* Josephson inductance is identified as

$$L_s = \frac{\Phi_0}{2\pi I_c} \frac{1}{\cos\phi} = \frac{\Phi_0}{2\pi I_c} \frac{1}{\sqrt{1-(I/I_c)^2}} \equiv \frac{L_c}{\sqrt{1-(I/I_c)^2}} \tag{2.20}$$

where (2.13) has been used. Here, $L_c = (\Phi_0/2\pi I_c)$ is the specific Josephson inductance. Note that for very small bias currents I, the inductance essentially reduces to $L_s \approx L_c$.
At finite temperatures, a Josephson element also contains normal electrons that are not condensed into Cooper pairs, so-called *quasiparticles*. In the zero-voltage state $I < I_c$ for temperatures much smaller than the critical temperature T_c, these normal electrons contribute only a small fraction to the total current, whereas in the voltage state $I > I_c$ all current is in fact carried by electrons rather than Cooper pairs. Thus for a complete description of the Josephson element, additional current channels have to be considered. These include *resistive*, *capacitive* and *noise current channels*. The resistive contribution results from the breaking up of Cooper pairs due to thermal excitations, which has a non-vanishing probability at finite temperatures. Then also 'unpaired', normal electrons contribute to the total current flowing through the junction, which is commonly referred to as the *normal* current I_N. Note that this current is resistive in nature, which can ultimately be traced back to the fermionic character of electrons as opposed to the bosonic properties of Cooper pairs [49]. The electrons due to the breaking up of Cooper pairs are referred to as quasiparticles and their contribution to the total current can become substantial for temperatures close to the transition temperature T_c. The second contribution results from the

capacitance of a Josephson junction. Since a superconductor/insulator/superconductor junction simply represents a parallel-plate capacitor, a Josephson junction also has a finite displacement current $I_D = C_J \cdot (dV/dt)$ in the presence of a time-varying voltage. Finally, current noise is taken into account by generically including an additional current I_F [1]. Thus using Kirchhoff's rules, the total current through a Josephson junction in the voltage state is written as [55, 56]

$$\begin{aligned} I &= I_s + I_N + I_D + I_F \\ &= I_c \sin\phi + V \cdot G_N(V) + C_J \frac{dV}{dt} + I_F \end{aligned} \tag{2.21}$$

where the voltage dependence of the conductance G_N in the ohmic term results from the fact that additional Cooper pairs break up if the voltage exceeds the gap voltage $V_g = 2\Delta/e$ with Δ denoting the BCS energy gap. Now using the second Josephson equation (2.16), the current through a junction reads

$$I = I_c \sin\phi + G_N(V)\frac{\Phi_0}{2\pi}\frac{d\phi}{dt} + C_J \frac{\Phi_0}{2\pi}\frac{d^2\phi}{dt^2} + I_F \,. \tag{2.22}$$

The capacitance of an ideal Josephson element is in general well approximated by the standard expression

$$C_J = \frac{\varepsilon_r \varepsilon_0 A}{d} \tag{2.23}$$

where ε_r denotes the relative dielectric constant of an oxide barrier of thickness d and area A. For the typical junctions in the experiments presented in this thesis, the Josephson capacitance per unit junction area is on the order of a few fF/μm^2.

RCSJ-Model

As is obvious from equation (2.21), a Josepshon junction can be effectively modeled as a parallel circuit, see Fig. 2.2a. In this so-called resistively and capacitively shunted junction (RCSJ) model, the voltage-dependence of the conductance is neglected. Thus using (2.18) and (2.22), one arrives at the following differential equation governing the behavior of a Josephson junction in the voltage state [38]

$$\left(\frac{\Phi_0}{2\pi}\right)^2 C_J \frac{d^2\phi}{dt^2} + \left(\frac{\Phi_0}{2\pi}\right)^2 \frac{1}{R_N}\frac{d\phi}{dt} + \frac{d}{d\phi}\left[E_{J0}\left(1 - \cos\phi - i\phi\right)\right] = 0 \tag{2.24}$$

where the normalized current $i = I/I_c$ has been introduced. One can compare this to the standard classical equation of motion of a particle of mass M moving along the coordinate x in a potential U with damping κ

$$M\frac{d^2x}{dt^2} + \kappa\frac{dx}{dt} + \nabla U = 0 \,. \tag{2.25}$$

[1] As will be discussed later on, this noise exhibits a typical $1/f$ characteristic, hence it's denoted by I_F .

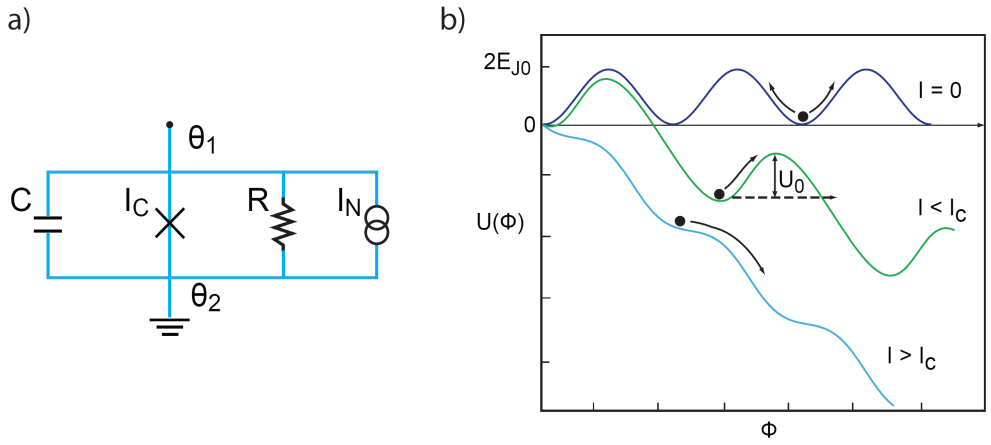

Figure 2.2: (a) The RCSJ equivalent circuit model. (b) Mechanical analogue of the dynamics of the gauge-invariant phase ϕ in a tilted washboard potential. Three different cases $I = 0, I < I_c, I > I_c$ are shown with the corresponding dynamics of the 'phase particle' illustrated by arrows.

Mapping the two equations of motion, a 'potential' for the phase of the Josephson junction can be identified as

$$U(\phi) = E_{J0}\,(1 - \cos\phi - i\phi) \tag{2.26}$$

which is commonly referred to as the *tilted washboard* or Josephson potential. Similarly, the mass M of the 'phase particle' as well as the damping κ and the quality factor Q of a Josephson junction are found

$$M = C_J \left(\frac{\Phi_0}{2\pi}\right)^2 \quad , \quad \kappa = \left(\frac{\Phi_0}{2\pi}\right)^2 \frac{1}{R_N} \quad , \quad Q = \sqrt{\frac{2\pi}{\Phi_0} I_c R_N^2 C_J} \equiv \sqrt{\beta_c} \tag{2.27}$$

where the *Stewart-McCumber parameter* $\beta_c = (2\pi/\Phi_0) I_c R_N^2 C_J$ has been introduced, which describes the damping strength of a junction. Note that in practice, however, the damping is governed by the impedance of the embedding circuit of the junction rather than by the intrinsic resistance R_N.

The analogy between the motion of a gauge-invariant phase difference across a Josephson junction and the damped motion of a particle is illustrated in Fig. 2.2b. In the zero-voltage state $I < I_c$, the phase potential is effectively given by $U(\phi) \approx E_{J0}(1-\cos\phi)$ and becomes increasingly tilted when ramping up the bias current. The tilt gives rise to quantum tunneling of the phase. For vanishing bias current $I = 0$, the height of the tunneling potential barrier is approximately $U_0 \sim E_{J0}$ and the oscillation frequency is given by

$$\omega_0 = \sqrt{\frac{2\pi I_c}{\Phi_0 C}}\,, \tag{2.28}$$

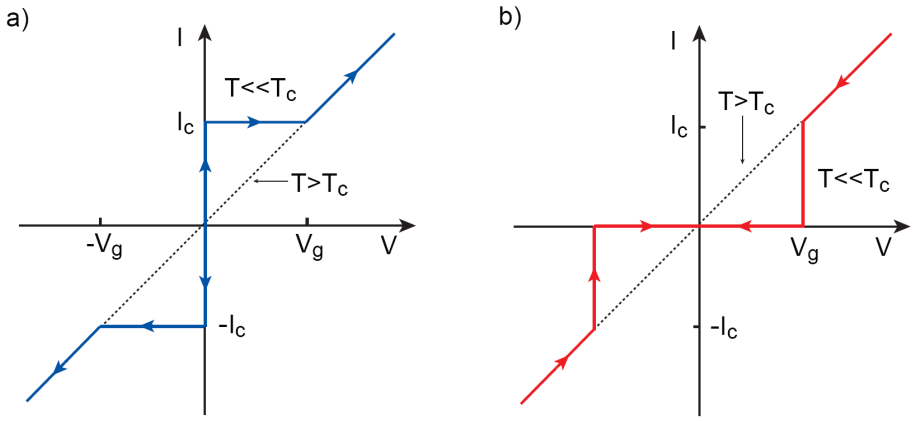

Figure 2.3: Schematic current-voltage characteristics of a driven Josephson junction: (a) Increasing current, (b) decreasing driving current, see text for details.

which is also referred to as the plasma frequency. The corresponding quantum tunneling rate of the 'phase particle' through the barrier U_0 is then written as [47]

$$\Gamma_q = a_q \frac{\omega_0}{2\pi} \exp\left(-\frac{36}{5}\frac{U_0}{\hbar\omega_0}\right) \tag{2.29}$$

where a_q is a damping dependent, dimensionless prefactor. The characteristic form of the nonlinear potential $U(\phi)$ forms the basis for quantum information processing with so-called superconducting phase qubits [39, 19] (see also section 2.5).

Current-Voltage Characteristics

The behavior of a lumped Josephson junction is to a good approximation described by the RCSJ differential equation. In particular, its peculiar current-voltage characteristics and response to driving sources can be conveniently discussed in the framework of the RCSJ model. The schematic current-voltage characteristics of an ideal, current-driven Josephson junction are depicted in Fig. 2.3. The IV characteristics strongly depend on the sweeping direction of the current. First, the case of increasing current is shown in Fig. 2.3a for temperatures well below the critical temperature $T \ll T_c$. Starting from $I = 0$, the current is first carried completely by the supercurrent (zero-voltage state) and there is no voltage drop until I reaches the critical current I_c. In terms of the RCSJ model, the washboard is only slightly tilted in that case and the phase particle is trapped in one of the potential minima (see Fig. 2.2), i.e. it is in a stationary state. For $T \ll T_c$ and $|V| < V_g$, the normal current contribution due to quasiparticles vanishes since neither the thermal energy $k_B T$ nor the energy eV supplied by the external circuit are sufficient to break up Cooper pairs, i.e. the current is carried almost entirely by the supercurrent. At $I = I_c$, the voltage suddenly increases from $V = 0$ to the gap voltage V_g, which is referred to as 'switching'. For $I > I_c$, the junction is in the normal conducting state and the current is carried completely by quasiparticles, which gives rise to the linear, ohmic dependence shown in

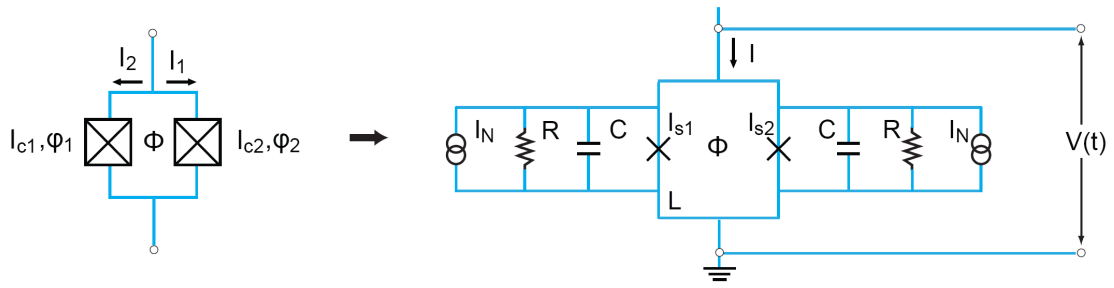

Figure 2.4: Circuit diagram of a SQUID and equivalent RCSJ model, in analogy to the case of a single Josephson junction of Fig. 2.2.

Fig. 2.3a. In this region, the washboard is tilted so strongly, that no minima exist anymore and thus the phase particle can move freely, resulting in a time-dependent phase difference and a voltage drop according to the second Josephson relation. Note that the IV curve is symmetric with respect to the origin. Furthermore, the case of decreasing current is depicted in Fig. 2.3b, which is often referred to as the quasiparticle curve. Starting from $I > I_c$, the junction is first in the voltage state, i.e. the current is carried by quasiparticles. Decreasing the current to below the critical current, we enter a region of constant voltage drop across the junction $V = V_g$ and at $I = 0$, the voltage switches from $+V_g$ to $-V_g$.

2.4 Superconducting Quantum Interference Devices

One of the most influential developments in the wake of the discovery of the Josephson effects was the invention of the so-called superconducting quantum interference device (SQUID). The first working devices date back to the sixties and over the course of the last three decades the SQUID has become a highly valuable tool in a vast number of different applications, ranging from ultra-sensitive magnetometers to ultra-low noise amplifiers or digital readout electronics [38], among many others. Moreover, the investigation of SQUIDs and the Josephson effects ultimately paved the way for superconducting quantum information processing. The discoveries that led to the development of the SQUID can be traced back to half a century ago when flux quantization was predicted in [57] and experimentally observed in Refs. [58] and [59]. Shortly after Josephson predicted the tunneling of Cooper pairs across a thin insulating barrier [50], the rf-SQUID was proposed in Ref. [60].

2.4.1 Critical Current and Tunability

A SQUID consists of two Josephson junctions forming a closed superconducting loop, as shown in Fig. 2.4. It is based on a unique combination of two fascinating and equally useful quantum-mechanical effects, namely flux quantization and Josephson tunneling. As will be discussed in this section, a SQUID can essentially be considered as a single Josephson junction with a flux tunable

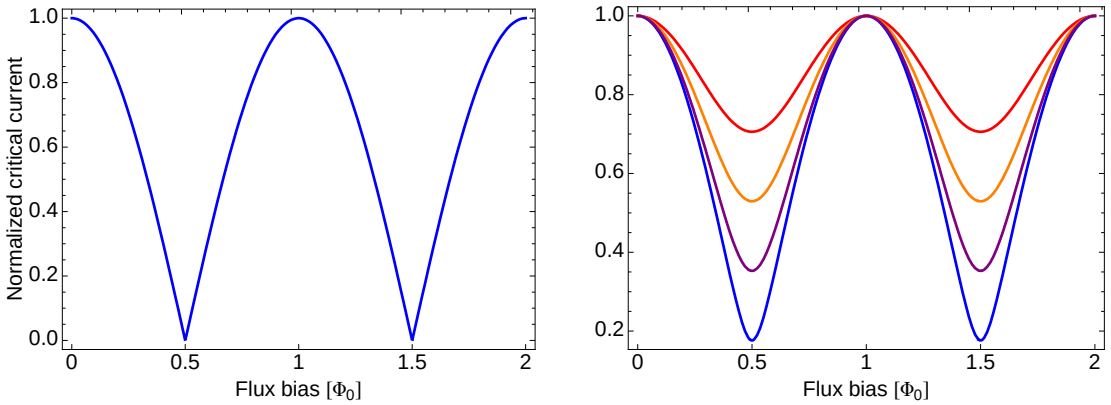

Figure 2.5: (a) Maximum critical current of a symmetric SQUID as a function of external flux bias Φ, normalized with respect to $(I_{c1}+I_{c2})$. (b) Maximum critical current of an asymmetric SQUID for different degrees of junction asymmetry: $d = 20\%$ (blue), $d = 35\%$ (purple), $d = 50\%$ (orange) and $d = 70\%$ (purple).

inductance L_s and Josephson energy E_s. According to Kirchhoff's rules, the total supercurrent through a SQUID loop is given by

$$I_s = I_{s1} + I_{s2} = I_{c1}\sin\phi_1 + I_{c2}\sin\phi_2\,. \tag{2.30}$$

Both phase and magnetic flux through such a superconducting loop are quantized according to

$$\Phi = \Phi_0 \cdot n \quad , \quad \phi = 2\pi n \tag{2.31}$$

from which it also follows that (see [38] or [49], for instance)

$$\phi_2 - \phi_1 = 2\pi n + \frac{2\pi\Phi}{\Phi_0} = \left(\frac{2\pi}{\Phi_0}\right)\Phi \,\mathrm{mod} 2\pi\,. \tag{2.32}$$

where Φ denotes the magnetic flux threading the loop. Thus the total supercurrent reads

$$I_s = I_{c1}\sin\phi_1 + I_{c2}\sin\left(\phi_1 + \frac{2\pi\Phi}{\Phi_0}\right)\,. \tag{2.33}$$

The magnetic flux Φ consists of an external contribution Φ_{ext} from applied magnetic fields as well as a self-inductance contribution $\Phi_{\mathrm{L}} = LI_{\mathrm{cir}}$, which accounts for the induction caused by the supercurrent I_{cir} circulating in the loop. Since it holds that $I_{\mathrm{cir}} = (I_{s1} - I_{s2})/2$, the total magnetic flux is given by

$$\begin{aligned}\Phi &= \Phi_{\mathrm{ext}} + LI_{\mathrm{cir}} \\ &= \Phi_{\mathrm{ext}} + \frac{L}{2}\left(I_{c1}\sin\phi_1 - I_{c2}\sin\left(\phi_1 + \frac{2\pi\Phi}{\Phi_0}\right)\right)\,.\end{aligned} \tag{2.34}$$

The SQUID's self-inductance contribution can be neglected for $LI_c \ll \Phi_0$, which is the case for very small loop sizes. Now setting $\Phi \equiv \Phi_{\mathrm{ext}}$ and neglecting self-inductance, the maximum

critical current can be easily found by maximizing (2.33) with respect to ϕ_1, which gives

$$I_c = \left[(I_{c1} - I_{c2})^2 + 4 I_{c1} I_{c2} \cos^2 \left(\pi \frac{\Phi}{\Phi_0} \right) \right]^{1/2} \tag{2.35}$$

and reduces to

$$I_c = 2 I_{c0} \left| \cos \left(\pi \frac{\Phi}{\Phi_0} \right) \right| \tag{2.36}$$

for symmetric junctions $I_{c1} = I_{c2}$. Thus, the critical current of a SQUID is a periodic function of Φ and can be tuned with an external magnetic flux. In case of non-negligible self-inductance, one has to find a consistent solution of the two equations (2.33) and (2.34), as shown in Ref. [61]. For large self-inductance $L I_c \gg \Phi_0$, the flux generated by the circulating supercurrent starts to compensate the external flux and thus the tunability of a given SQUID decreases with increasing L. In the devices used in our experiments, this self-inductance is usually very small and not a limiting factor for the SQUID tunability [38].
Neglecting self-inductance, the critical currents of both symmetric (2.36) and asymmetric (2.35) SQUIDs are plotted as functions of Φ in Fig. 2.5 for different $\Delta I_c = I_{c1} - I_{c2}$ with $I_{c1} + I_{c2} =$ const. .As can be seen, the range of current modulation with flux is increasingly reduced for growing ΔI_c. This does, however, also make the SQUID less prone to magnetic field noise which will become important later on when considering noise and decoherence in such systems. In that sense, the relative asymmetry $d = (I_{c1} - I_{c2})/(I_{c1} + I_{c2})$ of the two junctions can be used as a design parameter to realize a desired tuning range and a corresponding flux-noise sensitivity. The extrema of $I_c(\Phi)$ represent so-called 'sweet spots' where the SQUID is to first order insensitive to flux noise, which is discussed in more detail in sections 2.5 and 3.2.
The magnetic field dependence of the critical current of a SQUID gives rise to a tunable inductance according to (2.20)

$$L_s(\Phi, I) = \frac{\Phi_0}{2\pi} \left[(I_{c1} - I_{c2})^2 + 4 I_{c1} I_{c2} \cos^2 \left(\pi \frac{\Phi}{\Phi_0} \right) - I^2 \right]^{-1/2} \tag{2.37}$$

where I is the bias current. Thus, a SQUID represents a circuit element with a flux-tunable, non-linear inductance. In terms of the RCSJ model, it is described by the equivalent circuit depicted in Fig. 2.4b. Here, the total capacitance of the two junction system is given by

$$C_s = \varepsilon_0 \varepsilon_r \left(\frac{A_1}{d_1} + \frac{A_2}{d_2} \right) \tag{2.38}$$

with A_i and d_i denoting the area and thickness of junction barrier i. Note that in practice one also has to account for possible stray capacitances. The total impedance of the SQUID loop circuit of Fig. 2.4 reads

$$Z_s(\omega, \Phi) = \frac{i\omega L_s(\Phi) R_s}{R_s + i\omega L_s(\Phi) - \omega^2 L_s(\Phi) C_s R_s} \,. \tag{2.39}$$

where we have assumed a linear inductance in the limit $I/I_c \ll 1$. Note that all SQUID properties are periodic in Φ_0. The characteristic Josephson energy E_s of a SQUID can be directly inferred

from the single junction case. The magnetic flux-dependence naturally results in a tunable Josephson energy of the two parallel junctions [62]

$$E_s = E_{j\Sigma} \cos\left(\frac{\pi\Phi}{\Phi_0}\right) \sqrt{1 + d^2 \tan^2\left(\frac{\pi\Phi}{\Phi_0}\right)} \tag{2.40}$$

where $E_{j\Sigma} = E_{j1} + E_{j2}$. Here, we have introduced the energy asymmetry of the junctions

$$d = \frac{E_{j2} - E_{j1}}{E_{j2} + E_{j1}} \,. \tag{2.41}$$

2.4.2 Non-Linearity and Higher Order Effects

In analogy to the single junction case, the degree of non-linearity of a superconducting quantum interference device depends on the ratio of bias to critical current. This can be seen explicitly by considering the Taylor expansion of the square root in the Josephson inductance with respect to the ratio I/I_c. Neglecting self-inductance, the total inductance of the SQUID loop is just given by (2.37) and we find that it can be split up into linear and non-linear contributions

$$\begin{aligned} L_s(\Phi) &= \frac{\Phi_0}{2\pi I_c(\Phi)} \left[1 + \frac{1}{2!}\left(\frac{I}{I_c(\Phi)}\right)^2 + \frac{1}{4!}9\left(\frac{I}{I_c(\Phi)}\right)^4 + \ldots\right] \\ &= \frac{\Phi_0}{2\pi I_c(\Phi)} + A_3 I^2 + 9A_5 I^4 + \ldots \end{aligned} \tag{2.42}$$

where we have introduced the anharmonicity parameter of order n

$$A_n(\Phi) = \frac{1}{(n-1)!} \frac{\Phi_0}{2\pi} \frac{1}{I_c^n(\Phi)} \,. \tag{2.43}$$

In the limit of small bias currents $I \ll I_c$, the non-linearity of the SQUID is effectively suppressed by the critical current so that in lowest non-vanishing order one can essentially treat it as a regular linear circuit element that happens to have a flux-tunable impedance. This limit is desirable when trying to avoid anharmonicity in a quantum circuit while retaining tunability. In the context of the RCSJ-model, a SQUID in that case simply represents an harmonic oscillator with plasma frequency $\omega_p = (2\pi I_c/\Phi_0 C_s)^{1/2}$. Driving the oscillator at a frequency $\omega_D \ll \omega_p$ means that effectively no resonances are excited.

On the other hand, the non-linearity can reach significant levels when driving a SQUID-loop with large bias currents $I \gg I_c$. In that case, a SQUID represents an anharmonic oscillator with a non-linear energy level spectrum whose full quantum-mechanical description becomes non-trivial (see section 3.2). To second order in the bias current, we have for the non-linear inductance of a SQUID loop

$$\begin{aligned} L_s(\Phi) &= L_{s0}(\Phi) + A_3(\Phi) I^2 \\ &= \frac{\Phi_0}{2\pi}\left(\frac{1}{I_{c0}(\Phi)} + \frac{1}{4}\frac{I^2}{I_{c0}^3(\Phi)}\right) \,. \end{aligned} \tag{2.44}$$

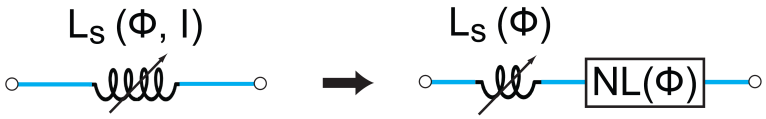

Figure 2.6: Separation of the SQUID into a series combination of a linear and a non-linear circuit element.

Thus to second order, the SQUID can be modeled as a series combination of a lumped linear inductance $L_{s0}(\Phi)$ and a non-linear element which is dependent on the bias current [37], see Fig. 2.6. Note that a separation in the form of a parallel circuit, where the current instead of the inductance is expanded, is completely equivalent. Including this non-linear perturbation, the total impedance in the lossless case reads

$$Z_s(\Phi) = i\left(\frac{1}{\omega(L_{s0}(\Phi) + A_3(\Phi)I^2)} - \omega C_s\right)^{-1} \tag{2.45}$$

from which we obtain the resonance frequency of the SQUID oscillator as

$$\begin{aligned} \omega_s &= \frac{1}{\sqrt{(L_{s0}(\Phi) + A_3(\Phi)I^2)C_s}} \\ &= \omega_{s0} - \frac{1}{2!}A_3 I^2 \frac{1}{2\sqrt{L_{S0}^3 C_s}} + \frac{1}{3!}A_3^2 I^4 \frac{3}{4\sqrt{L_{S0}^5 C_s^3}} - \ldots \end{aligned} \tag{2.46}$$

where $\omega_{s0} = 1/\sqrt{L_{s0}C_s}$ is the linear resonance frequency of the circuit. Clearly, the Taylor expansion shows that the non-linearity ultimately leads to frequency shifts which are proportional to the current flowing through the SQUID. This has important implications when the SQUID is incorporated into a larger resonant circuit: As a consequence of the SQUID non-linearity, the resonance frequency of the total circuit will also shift by a certain amount from its unperturbed value, depending on the magnitude of the bias current I flowing through the circuit. This poses important constraints on the choice of the optimal critical current for a given Josephson junction device. In some cases, a certain degree of non-linearity is a stringent requirement for operation, e.g. in superconducting qubits (section 2.5), whereas in others linearity is clearly favorable, in particular for the flux-tunable resonators discussed in section 3.2. There, a SQUID is incorporated into a larger resonant circuit (a transmission line resonator) to realize a flux-tunable harmonic oscillator. For a full quantum-mechanical description of such a system, one first needs to formulate the dynamics of the SQUID in terms of the Langrangian and Hamiltonian formalism.

2.4.3 Lagrangian and Hamiltonian Description

Thus far, the superconducting quantum interference device has been treated as a classical electrical circuit whose peculiar properties originate from the quantum-mechanical Josephson effect. Following section 2.1, the SQUID circuit can be easily quantized. As usual, the Lagrangian

consists of a potential and a kinetic energy part

$$\begin{aligned}\mathcal{L}_s &= \sum_{i=1,2}\left[\frac{\hbar^2(C_{J_i}/2)}{2(2e)^2}\dot{\phi}_i^2 + E_{J_i}\cos\phi_i\right] \\ &= \frac{\hbar^2(C_s/2)}{2(2e)^2}\dot{\phi}_s^2 - \sum_{n=0}^{\infty}\frac{(-1)^n}{2n!}\frac{E_s}{\phi_0^{2n}}\phi^{2n} \\ &\approx \frac{\hbar^2(C_s/2)}{2(2e)^2}\dot{\phi}_s^2 - \frac{E_s(\Phi)}{2\Phi_0^2}\phi_s^2 \end{aligned} \tag{2.47}$$

where ϕ_i denotes the phase difference across junction i and $\phi_s = (\phi_1 + \phi_2)/2$ and $C_s = (C_{J1} + C_{J2})/2$. In the last step, we have expanded the cosine potential term and made the harmonic approximation, i.e. kept only the leading term, and used the flux-dependent energy (2.40). Making the usual canonical transformation, the Hamiltonian of the SQUID in the harmonic approximation then reads

$$\mathcal{H}_s = \frac{\hbar^2}{(4e)^2 C_s}q_s^2 + \frac{E_s(\Phi)}{2\Phi_0^2}\phi_s^2 \tag{2.48}$$

where we have used the conjugate properties of charge and flux (see section 2.1). As expected, $\mathcal{H}_s$ has the form of a simple harmonic oscillator with the mapped quantities

$$m = \frac{2C_s}{\hbar^2}(2e)^2 \quad , \quad \omega_p = \sqrt{\frac{(2\pi)^2 E_s}{\Phi_0^2 C_s}} \tag{2.49}$$

The harmonic approximation is valid for $\phi_s \ll 1$, which corresponds to low amplitude plasma oscillations. If the SQUID is driven on resonance $\omega_d = \omega_p$, these oscillations are excited and the approximation breaks down, which can be effectively avoided by using operation frequencies for which $\omega_d \ll \omega_p$ holds. Since the plasma frequency is given by $\omega_p = (2\pi I_c/\Phi_0 C_s)^{1/2}$, this operating constraint directly translates to driving the SQUID far below its critical current, which provides a connection to the classical discussion of the non-linearity in section 2.4.2. On the other hand, for driving frequencies $\omega_d \sim \omega_p$, the harmonic approximation does no longer apply and the system has to be described in terms of the full non-linear SQUID Hamiltonian [62]

$$\mathcal{H}_s = -\frac{1}{2C(\Phi_0/2\pi)^2}\frac{\partial^2}{\partial\phi^2} + \left(\frac{\Phi_0}{2\pi}\right)^2\frac{1}{2L}\left(\phi^2 + \beta\cos\phi\right) \tag{2.50}$$

where β is the Stewart-McCumber parameter introduced before and C and L are the total capacitance and inductance of the SQUID circuit, respectively.

2.5 Superconducting Charge Qubits

The Josephson element has experienced a remarkable renaissance over the course of the last decade as its potential for scalable quantum information processing was established [1, 2, 3, 33, 39, 63, 64]. The intrinsic non-linearity of a Josephson junction generates strongly anharmonic energy levels and, in combination with its low dissipation, makes it a natural candidate for a

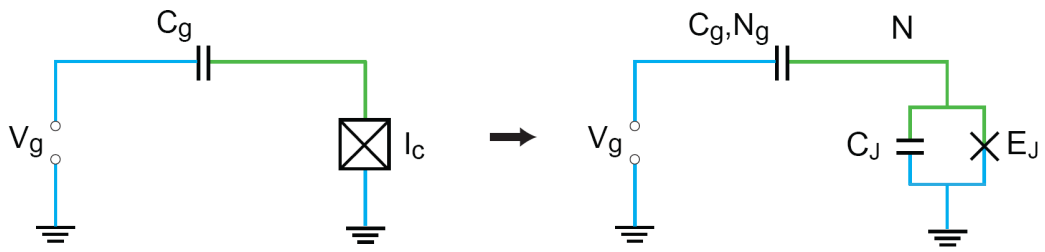

Figure 2.7: Equivalent circuit diagrams of a single Cooper pair box, see discussion in the text.

solid-state quantum bit (qubit). In general, three different 'flavors' of Josephson-junction based qubits can be distinguished according to their relevant degree of freedom: charge [33, 34], flux [65, 66] and phase [39]. In this thesis, we will focus on a specific type of superconducting charge qubit, the so-called Cooper pair box [34].

2.5.1 Single Cooper Pair Box

The Cooper pair box is a series combination of a Josephson junction and a gate capacitance C_g, as depicted in Fig. 2.7. It was theoretically proposed in Ref. [67] and first realized in Ref. [34]. In the Cooper pair box circuit, one electrode is shared between junction and capacitance, the so-called *island* shown in green in Fig. 2.7. The second electrode of the junction connects the circuit to a superconducting reservoir (in practice a ground), whereas the other capacitor electrode is attached to a bias voltage source V_g. In the superconducting state, the reservoir contains a large number of Cooper pairs. Cooper pairs can tunnel coherently through the junction onto the island, giving it a certain number of Cooper pairs N and a corresponding excess charge. In addition, an applied gate voltage V_g induces a certain number of polarization charges n_g on the plates of the capacitor and thus the total charge on the island is given by $2e(N - n_g/2)$. In practice, the gate charge n_g serves as a control or bias parameter that is used to compensate for offset charges q_{off} and fluctuations in the number of Cooper pairs on the island. Thus $n_g = q_{\text{off}} + C_g V_g/e$ is the controlled variable of the circuit and the Cooper pair box is classified as a *charge qubit*.

The quantum circuit of Fig. 2.7 is conveniently described in terms of the canonical pair of operators charge q and flux Φ, corresponding to the generalized momentum and position coordinates. The general Hamiltonian of the Cooper pair box circuit consists of an electrostatic and a magnetic part (see section 2.1)

$$\mathbf{H} = \mathbf{H}_{\text{el}} + \mathbf{H}_{\text{J}} = \frac{1}{2C} q^2 + \frac{1}{2L} \Phi^2 \,. \tag{2.51}$$

Taking into account possible stray capacitances, the total capacitance of the Cooper pair box circuit is $C_\Sigma = C_g + C_J + C_s$. The electrostatic or capacitive energy is then $E_c = q^2/2C_\Sigma$, whereas the inductive energy of the circuit is given by the Josephson energy $E_J = \Phi_0 I_c/2\pi =$

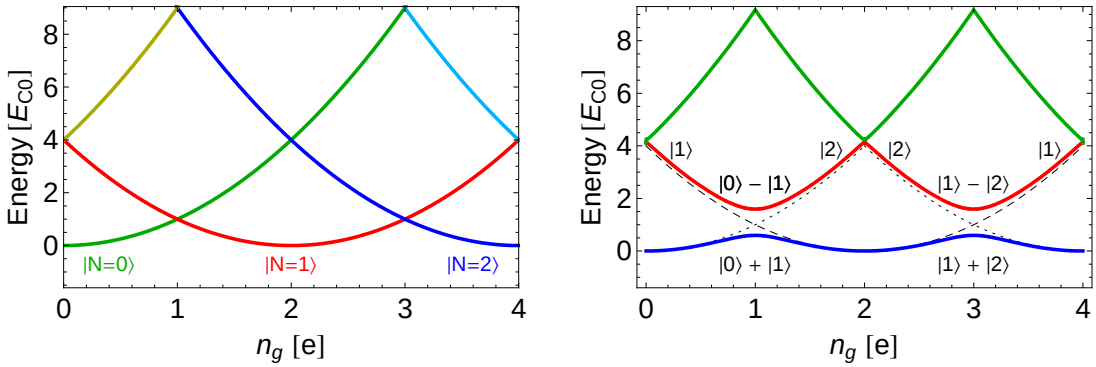

Figure 2.8: (a) Normalized eigenenergies of the bare electrostatic Hamiltonian $\mathbf{H}_{\text{el}}$. Each color refers to a different energy level and the kets denote the corresponding eigenstates $|N\rangle$. (b) Energy levels of the total Hamiltonian of the Cooper pair box $\mathbf{H}_{\text{CPB}}$ as a function of gate charge n_g. The energies from (a) are shown as dashed and dotted lines.

$(\Phi_0/2\pi)^2/L_s$, i.e. the second Josephson relation (2.16). Since the net charge on the island is $q = 2e(N - n_g/2)$, the total Hamiltonian is rewritten as

$$\mathbf{H}_{\text{CPB}} = \mathbf{H}_{\text{el}} + \mathbf{H}_{\text{J}} = 4E_{C0}(N - n_g/2)^2 - E_{J0}\cos\Theta \tag{2.52}$$

where $E_{C0} = (e^2)/2C_\Sigma$ denotes the charging energy and Θ the phase difference operator, which corresponds directly to (2.14). The dimensionless operators N and Θ are the conjugate generalized momentum and position coordinates, respectively, and thus they fulfill the canonical commutation relation (see also section 2.1)

$$[\Theta, N] = i \qquad \text{and} \qquad N = i\frac{\partial}{\partial\theta} \quad , \quad \Theta = -i\frac{\partial}{\partial n}. \tag{2.53}$$

where n and θ are eigenvalues of the two operators. The first term of the Hamiltonian represents the energy of a capacitor with a fixed, integer-quantized charge. The Josephson term $\mathbf{H}_{\text{J}}$ on the other hand describes the coherent tunneling of Cooper pairs onto the superconducting island. E_{J0} is the energy required for such a transfer of a Cooper pair from the reservoir to the island and $\mathbf{H}_{\text{J}}$ can be regarded as a discrete kinetic energy term. This will become more obvious in the charge representation which provides an intuitive approach for understanding the Cooper pair box.

Charge Basis

The unbounded, discrete charge basis diagonalizes the electrostatic part $\mathbf{H}_{\text{el}}$ of the CPB Hamiltonian. Here, the charge eigenstates $|n\rangle$ can be used to solve the corresponding eigenvalue problem, with n being the number of Cooper pairs on the superconducting island. The charge

basis is defined by

$$\langle m|n\rangle = \delta_{nm} \quad , \quad \mathbb{I} = \sum_n |n\rangle \langle n| \quad , \quad N|n\rangle = n|n\rangle \ . \tag{2.54}$$

Now rewriting $\cos\Theta = (1/2)(\exp[i\Theta] + \exp[-i\Theta])$ and using (2.53), the spectral decomposition of the Hamiltonian in the charge basis is

$$\mathbf{H}_{\mathrm{CPB}} = \sum_n \left[4E_{C0}(n - n_g/2)^2 |n\rangle \langle n| - \frac{E_\mathrm{J}}{2} \left(|n\rangle \langle n+1| + |n+1\rangle \langle n| \right) \right] . \tag{2.55}$$

In this representation, the eigenvalue problem can be solved by numerically diagonalizing the Hamiltonian which yields the energy levels as functions of gate charge n_g. Since this basis is unbounded, the Schrödinger equation can not be solved analytically without first restricting the problem to a certain subspace using a projection operator approach (see section 2.5.2).
The energy levels of the Cooper pair box are depicted in Fig. 2.8 as functions of the gate charge parameter n_g taken in units of single electrons. The bare electrostatic levels from the first term of the Hamiltonian are shown in Fig. 2.8a. As can be seen, the unperturbed term $\mathbf{H}_{\mathrm{el}}$ has a parabolic energy level structure $E_n = 4E_{C0}(n - n_g/2)^2$ which is periodic in the gate charge n_g. Degeneracy occurs at the crossing points of the energy parabolas, the so-called charge degeneracy points, e.g. at $n_g = 1$. As shown in Fig. 2.8b, the degeneracy is in turn lifted by the tunneling term $\mathbf{H}_\mathrm{J}$, which acts as a perturbation giving only off-diagonal matrix elements in the charge basis. The crossings of the energy levels of the unperturbed electrostatic Hamiltonian become avoided and the charge degeneracy points vanish for the total Hamiltonian $\mathbf{H}_{\mathrm{CPB}}$. This generates a periodic energy band structure with periodicity $n_p = 2e$. If the gate charge changes from n to $n+1$, for instance by increasing the gate voltage by $V_g = 2e/C_g$, the ground state of the Cooper pair box also shifts from $|n\rangle$ to $|n+1\rangle$. This just means that in the ground state an induced polarization charge $2e$ on the capacitor plates is compensated for by an additional Cooper pair on the island via tunneling from the reservoir. In the presence of Josephson tunneling, the charge eigenstates $|n\rangle$ and $|n+1\rangle$ are no longer degenerate at $n_g = 1$, they are however still coupled by tunneling. This coupling leads to coherent superposition states at the avoided crossings in the energy band structure Fig. 2.8b

$$|\Psi\rangle_{\mathrm{CPB}} = \frac{1}{\sqrt{2}} \left(|n\rangle \pm |n+1\rangle \right) . \tag{2.56}$$

At the charge degeneracy points, the lowest two energy bands have a minimum spacing of E_J whereas the difference between adjacent higher bands is much larger. This anharmonicity is caused by the non-linear Josephson element. The possibility of realizing anharmonic energy bands does in turn make it possible to treat the Cooper pair box as an effective two-level system and, ultimately, to use it as a quantum bit. The degree of anharmonicity of the energy level spectrum is essentially determined by the ratio E_J/E_C of Josephson energy to charging energy, which can be seen explicitly in the phase representation.

Phase Basis

In contrast to the charge basis, the basis of the conjugate operator Θ does allow for analytical solutions of the CPB Schrödinger equation. The continuous, periodic phase basis is given by

$$\langle\theta|\theta'\rangle = \delta(\theta-\theta') \quad , \quad \mathbb{I} = \int d\theta\,|\theta\rangle\langle\theta| \quad , \quad \Theta\,|\theta\rangle = \theta\,|\theta\rangle \quad , \quad |\theta\rangle = |\theta+2\pi\rangle\ . \tag{2.57}$$

The periodicity of the phase has already been introduced in section 2.3 and it is a direct consequence of charge discreteness $n = 2e$ in BCS theory [49]. In complete analogy to the usual unitary transformation between momentum and position basis, charge and phase basis are connected via discrete and continuous Fourier transforms, i.e. [47]

$$|\theta\rangle = \sum_n e^{i\theta n}\,|n\rangle \quad , \quad |n\rangle = \int_0^{2\pi} d\theta e^{-i\theta n}\,|\theta\rangle \tag{2.58}$$

which in turn also gives the translators for the two conjugate bases [68] (see section 2.1)

$$e^{in_0\Theta}\,|n\rangle = |n+n_0\rangle \quad , \quad e^{-i\Theta_0 N}\,|\theta\rangle = |\theta-\theta_0\rangle\ . \tag{2.59}$$

Thus using (2.57) and (2.58), the time independent Schrödinger equation in the phase representation reads

$$4E_{C0}\left(i\frac{\partial}{\partial\theta} - n_g/2\right)^2\Psi_k(\theta) - E_{J0}\cos\theta\Psi_k(\theta) = E_k\Psi_k(\theta) \tag{2.60}$$

where $\langle\theta|k\rangle = \Psi_k(\theta)$. The corresponding spectral decomposition of the Hamiltonian is given by

$$H_{\mathrm{CPB}} = 4E_{C0}\int_0^{2\pi} d\theta\left(i\frac{\partial}{\partial\theta} - n_g/2\right)^2|\theta\rangle\langle\theta| - \frac{E_{J0}}{2}\int_0^{2\pi} d\theta\left(e^{i\theta}+e^{-i\theta}\right)|\theta\rangle\langle\theta|\ . \tag{2.61}$$

(2.60) belongs to the class of *Mathieu equations* and can thus be solved analytically [68]. First, note that the translational relations (2.59) together with the gate charge periodicity imply that the solution of the Schrödinger equation is of the form $\Phi_k(\theta) = \exp(-in_g\theta)\Psi_k(\theta)$. Plugged into (2.60), this gives the equation in an explicit Mathieu form. The energy levels can then be written in the phase basis as [69]

$$E_m(n_g) = E_{C0}\mathcal{M}_{\mathrm{A}}(2[n_g + k(m,n_g))])\,(-E_{J0}/2E_{C0}) \tag{2.62}$$

where $\mathcal{M}_{\mathrm{A}}$ is Mathieu's characteristic value and $k(m,n_g)$ an eigenvalue sorting function. Prepackaged solutions for the Mathieu equations can be found in standard mathematical software, e.g. in *Mathematica*. While the charge representation provides for a more easily accessible, physical interpretation and an intuitive understanding of the Cooper pair box, the phase basis gives exact results and most calculations are less time-consuming and not as prone to possible truncation errors. The phase basis is especially well-suited for large ratios $(E_J/E_C) \gg 1$, where the Cooper pair box starts to go over from the *charge* to the *phase regime*. As will be discussed in detail in section 2.7, the energy bands tend to flatten out for increasing ratio of Josephson to

coupling energy. This is a crucial observation which has led to substantial improvements of the original Cooper pair box design in the form of the *transmon* (see section 2.7) [69, 70].

2.5.2 Two Level Approximation: CPB as a Qubit

Although the Cooper pair box has an infinite number of energy levels, the discussion so far has shown that strong degrees of anharmonicity are achieved as a consequence of the Josephson non-linearity. The anharmonicity is maximized at the avoided crossings, the former charge degeneracy points, where the spacing between the lowest two energy bands is much smaller than between the higher adjacent bands. The Cooper pair box can thus be treated as an effective two level system, i.e. a quantum bit or a pseudo spin 1/2 particle. Restricting the total Hilbert space of the CPB to the two lowest states $\{|0\rangle, |1\rangle\}$ in the charge basis, the Hamiltonian simplifies to

$$\begin{aligned}
\widetilde{\mathbf{H}}_{\mathrm{CPB}} &= P_{01} H_{\mathrm{CPB}} P_{01} \\
&= 4E_{C0}\left[n_g^2 |0\rangle\langle 0| + (1-n_g)^2 |1\rangle\langle 1|\right] - \frac{E_{J0}}{2}(|0\rangle\langle 1| + |1\rangle\langle 0| + |1\rangle\langle 2| + |2\rangle\langle 1|) \\
&\approx 4E_{C0}\left[n_g^2 |0\rangle\langle 0| + (1-n_g)^2 |1\rangle\langle 1|\right] - \frac{E_{J0}}{2}(|0\rangle\langle 1| + |1\rangle\langle 0|) \qquad (2.63)
\end{aligned}$$

where $P_{01} = \sum_{n=1,2} |n\rangle\langle n|$ is a projector. In the last step we have neglected an off-diagonal term as it only generates transitions to the third level, a process that is essentially suppressed for strong enough anharmonicity.
Using the Pauli representation $\{\sigma_x, \sigma_y, \sigma_z\}$, the state of the Cooper pair box can be conveniently described by a unit vector on the Bloch sphere and the Hamiltonian assumes a simpler form. In general, an arbitrary operator A on a two-dimensional Hilbert space can be written as $A = (-1/2)h_i\sigma_i + \mathrm{Tr(A)} \cdot \mathbb{1}$ where h_i is the unique representative vector. For the Cooper pair box we have $A = \mathbf{H}_{\mathrm{CPB}}$ and [68]

$$\vec{h} = 4E_{C0}(1-n_g)\vec{e_z} + E_{J0}\vec{e}_x \,. \qquad (2.64)$$

This gives the major result of this section, the Hamiltonian in Pauli representation

$$\begin{aligned}
\mathbf{H}_{\mathrm{CPB}} &= -2E_{C0}(1-n_g)\sigma_z - \frac{E_{J0}}{2}\sigma_x \\
&= -\frac{1}{2}(E_{\mathrm{el}}\sigma_z + E_{J0}\sigma_x) \qquad (2.65)
\end{aligned}$$

where the mean energy of the system $\overline{E} = \mathrm{Tr}(\mathbf{H}_{\mathrm{CPB}})$ was subtracted as gauge choice and the electrostatic energy $E_{\mathrm{el}} = 4E_{C0}(1-n_g)$ was introduced [2]. Using the mixing angle [72]

$$\theta_m = \arctan\left(\frac{E_{j0}}{E_{\mathrm{el}}}\right) , \qquad (2.66)$$

[2] Note that this result can also be derived less rigorously from (2.63) by making the identifications $\sigma_x \to |n\rangle\langle n+1| + |n+1\rangle\langle n|$, $\sigma_z \to 1/2(|n\rangle\langle n| + |n+1\rangle\langle n+1|$ and $\overline{E} = 8E_{C0}n_g^2(1-2n_g)$ [71].

the Hamiltonian (2.65) can be easily solved for the symmetric and antisymmetric eigenstates

$$|\Psi_{\uparrow/\downarrow}\rangle = \cos\left(\frac{\theta_m}{2}\right)|0\rangle \pm \sin\left(\frac{\theta_m}{2}\right)|1\rangle \ . \tag{2.67}$$

These two states form the computational subspace $\{|0\rangle, |1\rangle\} \leftrightarrow \{|\Psi_{\downarrow}\rangle, |\Psi_{\uparrow}\rangle\}$ used for encoding quantum information in a Cooper pair box. The ground state is a symmetric superposition of the charge eigenstates whereas the excited state is anti-symmetric. Controlled manipulation of these states allows for quantum information processing with the Cooper Pair Box [8, 33, 34, 68].
The simplified Hamiltonian in the two-level approximation is formally equivalent to that of a spin-1/2 particle in a magnetic field in the x-z plane. The quantization axis of the CPB qubit is parallel to this field. To make everything a bit more elegant and less cumbersome, we can rotate the coordinate system by the mixing angle θ_m about the y-axis so that

$$\mathbf{H}_{\mathrm{CPB}} = \hbar\omega_a\sigma_z \tag{2.68}$$

where the transition frequency between ground and excited state

$$\hbar\omega_a = \sqrt{E_{\mathrm{el}}^2 + E_{\mathrm{J0}}^2} = \sqrt{[4E_{C0}(1-n_g)]^2 + E_{J0}^2} \tag{2.69}$$

was introduced. In this rotated frame, the computational states are simply given by the charge eigenstates $|0\rangle$ and $|1\rangle$ at $n_g = 1$. At the charge degeneracy point $n_g = 1$, the electrostatic component vanishes and the qubit transition frequency is purely determined by the Josephson tunneling energy. At this point, the rotated frame is identical to the original frame $\theta_m \to 0$ and the computational subspace is spanned by the bare charge states $|0\rangle$ and $|1\rangle$.
So far, the two-state approximation has demonstrated that the CPB realizes an effective two-level system that can in principle be used for quantum computation. In practice, however, operating a CPB as a qubit represents a formidable challenge, both from a scientific as well as an engineering point of view. The fundamental criteria that must be fulfilled for scalable quantum information processing are compactly summarized in the form of the DiVincenzo critieria [73, 25]:

1. A scalable physical system with well-characterized qubits
2. A reset operation - the ability to initialize the state of the qubits to a simple fiducial state
3. Long relative coherence times that allow for the implementation of quantum error correcting codes
4. A universal set of quantum gates
5. High-fidelity readout - a qubit specific measurement capability
6. The ability to interconvert stationary and flying qubits
7. The ability to faithfully transmit flying qubits between specified locations

In the Cooper pair box, superconductivity naturally helps in fulfilling some of these criteria (ultra-low dissipation and noise at low temperatures). Up until now, the superconducting charge qubit approach presented in this thesis sufficiently satisfies criteria 1, 2 and 4 [48]. In addition, the potential to fulfill criteria 6 and 7 has been demonstrated in recent experiments [9]. So far,

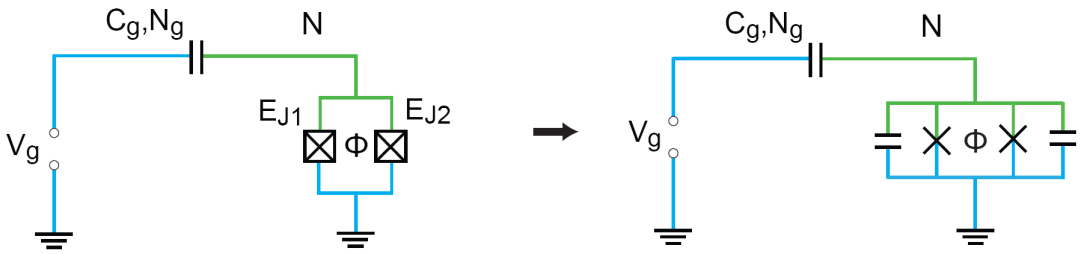

Figure 2.9: Equivalent circuit diagrams of the split Cooper pair box, see discussion in text.

number 3 and 5 are not sufficiently met, however recent developments have already shown significant improvements towards this goal [7, 69, 70, 74].

2.5.3 Split Cooper Pair Box

The split Cooper pair box is a combination of a superconducting quantum interference device (section 2.4) and a single Cooper pair box. It combines the flux-tunability of the Josephson energy of a SQUID with the gate charge control in the single Cooper pair box. In a split CPB, as depicted in Fig. 2.9, the single Josephson junction is simply replaced by a SQUID loop. This introduces magnetic flux as a dynamical variable. With the general results for SQUIDs obtained in section 2.4, it is straight forward to generalize the single to the split CPB case. From a circuit point of view, all that is done is replacing one parallel circuit by another. Everything else stays the same (see Fig. 2.9).
The two parallel junctions of the SQUID geometry are each characterized by a Josephson energy $E_{\mathrm{J}1/\mathrm{J}2}$ and a superconducting phase difference $\phi_{1/2}$. According to (2.40), the total tunneling energy of the loop then reads

$$\begin{aligned} E_{\mathrm{J}} &= -E_{J\Sigma}\cos\left(\pi\frac{\Phi}{\Phi_0}\right)\sqrt{1+d^2\tan^2\left(\pi\frac{\Phi}{\Phi_0}\right)}\cos(\theta-\theta_0) \\ &= -E'_{\mathrm{J}0}\cos(\theta-\theta_0) \end{aligned} \tag{2.70}$$

where $\theta = (\phi_1+\phi_2)/2$, $E_{J\Sigma} = E_{\mathrm{J}1} + E_{\mathrm{J}2}$ and the phase $\tan\theta_0 = d\tan(\pi\Phi/\Phi_0)$, which can be eliminated for constant external flux [69]. Here, the junction asymmetry is given by

$$d = \frac{E_{\mathrm{J}2} - E_{\mathrm{J}1}}{E_{\mathrm{J}1} + E_{\mathrm{J}2}}\,. \tag{2.71}$$

The results from sections 2.5.1 and 2.5.2 are then conveniently translated to the case of a split CPB by making the substitution

$$E_{J0} \rightarrow E'_{J0} = E_{J\Sigma} \cos\left(\pi \frac{\Phi}{\Phi_0}\right) \sqrt{1 + d^2 \tan^2\left(\pi \frac{\Phi}{\Phi_0}\right)}\,. \tag{2.72}$$

Thus the split CPB behaves like a single Cooper pair box with a flux-tunable effective tunneling energy $E_{J0}(\Phi)'$. In total, we now have two external control parameters at our disposal, the gate charge n_g and the external flux Φ. Since the Josephson energy determines the energy level separation E_{01} between the two qubit states at the charge degeneracy point, the external magnetic flux can be used to tune the qubit transition frequency. Rewritting the Hamiltonian in the two-state approximation with the new flux-dependent Josephson part, the qubit transition (2.69) reads

$$\hbar\omega_a = \sqrt{E_{J\Sigma}(\cos^2(\pi\Phi/\Phi_0) + d^2 \sin^2(\pi\Phi/\Phi_0)) + 16E_C^2(1 - n_g)^2}\,. \tag{2.73}$$

Hence the split Cooper pair box realizes an effective quantum two-level system whose electrodynamical behavior can be controlled by an external gate charge n_g and an external magnetic flux Φ.

2.6 Noise Mechanisms

The two dominant noise sources in Josephson junction-based devices are magnetic flux and critical current noise, both of which have a long history of experimental and theoretical investigation [38, 75, 76, 77]. These noise mechanisms are universally present in all devices incorporating parallel Josephson junctions, e.g. in SQUIDs, superconducting qubits or Josephson rings. In the particular case of superconducting charge qubits, they are primarily responsible for *dephasing*, a form of decoherence discussed in detail below. For the Cooper pair box, charge noise represents the dominant noise source. This section gives a general overview of critical current and flux noise in Josephson devices. Since the devices used in our experiments are exclusively based on $Al/AlO_x/Al$ junctions, we will focus on these materials in detail.

Critical Current and Charge Noise

Fluctuations in the critical current of Josephson junctions arise from the trapping and subsequent release of electrons in traps in the tunnel barrier [75, 78, 79]. Following recent experimental and theoretical investigations of critical current noise in $Al/AlO_x/Al$ junctions [78, 80], defects in the oxide tunnel barrier have been shown to affect the conducting channels of the junctions. Within this microscopic theoretical model, an expression for critical current fluctuations in Josephson junctions can be derived by considering the electric dipole moments of two-level system defects in the barrier (e.g. OH^- impurities) and their effect on the total barrier potential. The rms

critical current fluctuations are given by [78]

$$\langle(\delta I_c)^2\rangle = \frac{L^4}{\mathcal{A}^2}\langle(\Delta g)^2\rangle\, I_c^2 \quad \Rightarrow \quad \delta I_c^{rms} = \frac{L^2}{\mathcal{A}}\sqrt{\langle(\Delta g)^2\rangle} I_c \tag{2.74}$$

where L denotes the junction barrier thickness and $\mathcal{A}$ the junction area. Furthermore,

$$\langle\Delta g^2\rangle = \frac{1}{2\Delta z_0}\int_0^{\pi} d\theta_0 \sin\theta_0 \int_{z_{01}}^{z_{02}} dz_0 \Delta g^2(\theta_0, z_0) \tag{2.75}$$

$$\Delta g^2(\theta_0, z_0) = \int_0^{2\pi} d\phi \int_{\rho_{min}}^{\rho_{max}} d\rho\rho \cdot \left[e^{\beta W(\rho,\phi,\Theta_0,z_0)} - e^{-\beta W(\rho,\phi,\Theta_0,z_0)}\right] \tag{2.76}$$

$$W(\rho, \phi, \Theta_0, z_0) = \sum_{n=1}^{\infty}(1-(-1)^n) f_n(\rho, \phi, \Theta_0, z_0) \tag{2.77}$$

$$f_n(\rho, \phi, \Theta_0, z_0) = K_0(n\pi\rho)\sin(n\pi z_0) - K_0\left(n\pi\sqrt{\rho^2 + d^2\sin^2\Theta_0 - 2\rho d\sin\Theta_0\cos\phi}\right) \times \sin(n\pi z_0 + n\pi d\cos\phi) \tag{2.78}$$

with all spatial coordinates being normalized to the barrier thickness L. Here $\Delta z_0 = z_{02} - z_{01}$ and $d := d/L$ denotes the average dipole spacing. $z_0 := z_0/L$ and θ_0 are used to describe the position of the dipoles within the barrier whereas the polar coordinates $\rho := \rho/L$ and ϕ are used as integration variables for integrating over the junction area. With these expressions, the corresponding noise power density is given by [78]

$$S_{I_c}(f, T) \approx \frac{P_0 k_B T}{4f}\frac{L^5}{\mathcal{A}}\langle(\Delta g)^2\rangle \tag{2.79}$$

where P_0 is the two-level system density of states. Now choosing the cutoffs $\rho_{min} = 0.1$ and $\rho_{max} = 4.0$ [3] as well as $p = 3.7\,\mathrm{D}$ for OH^- impurities and $\varepsilon_r = 10$, $d = 0.13\,\mathrm{nm}$, $U_0 = 1\,\mathrm{eV}$ for AlO_x junctions, one gets $\langle(\Delta g)^2\rangle = 1.5782 \times 10^2$. Thus for a typical Josephson junction of barrier thickness $L = 1\,\mathrm{nm}$ and area $A = 0.04\,\mu\mathrm{m}^2$, the rms critical current fluctuations amount to

$$\delta I_c^{rms} \approx 0.314 \times 10^{-5} I_c\,. \tag{2.80}$$

Using $P_0 = 10^{45}\,\mathrm{J}^{-1}\mathrm{m}^{-3}$ for AlO_x [78], the corresponding noise power at $f = 1\,\mathrm{Hz}$ and $T = 100\,\mathrm{mK}$ is given by

$$S_{I_c} \approx 1.3612 \times 10^{-13} I_c^2\,\mathrm{Hz}^{-1}\,. \tag{2.81}$$

We can compare this result to a second, more emperical model for δI_c^{rms} and S_{I_c} [75]. Based on an extensive analysis of experimental data on critical current fluctuations at $T = 4.2\,\mathrm{K}$ for different junction materials, the $1/f$ noise power spectral density is extrapolated to $T < 1\,\mathrm{K}$ and to a good approximation described by (see Ref. [75])

$$S_{I_c}(f, T) \approx \left[144\frac{(I_c/\mu\mathrm{A})^2}{(\mathcal{A}/\mu\mathrm{m}^2)}\left(\frac{T}{4.2\mathrm{K}}\right)^2(\mathrm{pA})^2\right]\frac{1}{f} \tag{2.82}$$

[3] For values $\rho_{min} < 0.1$ the effect of the dipole on the tunnelling potential would become too strong to be realistic and for $\rho > 2$, $W(\rho, \phi, \Theta_0, z_0)$ essentially vanishes [78].

where $\mathcal{A}$ denotes the total junction area. Note that here S_{I_c} is independent of the barrier thickness L. This noise power density corresponds to a rms fractional change in critical current as follows:

$$\langle(\delta I_c)^2\rangle\,|_{t=0} = \left[144\frac{(I_c/\mu\mathrm{A})^2}{(\mathcal{A}/\mu\mathrm{m}^2)}\left(\frac{T}{4.2\mathrm{K}}\right)^2(\mathrm{pA})^2\right]2\pi\int_{\omega_1}^{\omega_2}d\omega\frac{1}{\omega} \tag{2.83}$$

$$\Rightarrow \delta I_c^{\mathrm{rms}} = \left[288\pi\frac{(I_c/\mu\mathrm{A})^2}{(\mathcal{A}/\mu\mathrm{m}^2)}\left(\frac{T}{4.2\mathrm{K}}\right)^2(\mathrm{pA})^2\ln\left(\frac{\omega_2}{\omega_1}\right)\right]^{1/2} \tag{2.84}$$

Using the same parameters as in the calculations above yields

$$\delta I_c^{\mathrm{rms}} \approx 1.08675\times10^{-5}I_c \tag{2.85}$$

$$S_{I_c} \approx 2.04082\times10^{-12}I_c^2\mathrm{Hz}^{-1}\,. \tag{2.86}$$

where a bandwidth of $\omega_1 = 0.1$Hz - $\omega_2 = 1000$Hz has been assumed. Thus, despite the different temperature scaling, the results from the two approaches agree quite well and give the same order of magnitude for the rms fractional change $\delta I_c^{\mathrm{rms}}$ in the critical current.

Flux Noise

In addition to critical current noise and Johnson white noise from electronic components, most dc SQUIDs exhibit an excess low-frequency flux noise with a power spectrum that scales $\propto 1/f$ [76, 77, 79]. Although flux noise in SQUIDs and superconducting qubits has been the subject of extensive experimental investigations, a clear microscopic origin of this type of noise has not been identified yet. In a recent theoretical work [79], flux noise is thought to be generated by unpaired electrons that hop on and off defect centers by thermal activation, commonly referred to as *trapping*. Arriving at a defect, an electron randomly adopts a low-energy spin direction. While occupying a given trap, the spin is locked in its direction. When electrons are released from the traps, the uncorrelated changes of their spin directions result in a series of random telegraph signals that in sum give a $1/f$ power spectrum [79]. Since AlO_x barriers sometimes contain relatively large densities of defects such as OH^- impurities, flux noise can be a crucial issue in $Al/AlO_x/Al$ Josephson junctions. In the following, we will briefly discuss a generic approach that leads to an approximate quantitative expression for the rms fluctuations due to flux noise [79]. Assuming a simple relation for the spectral density

$$S_\Phi(f) = \alpha/f \tag{2.87}$$

with α constant, the total mean square flux noise can be written as

$$\langle(\delta\Phi_N)^2\rangle = \alpha\int_{f1}^{f2}df\frac{1}{f} = \alpha\cdot\ln\left(\frac{f_2}{f_1}\right) \tag{2.88}$$

where f_1 and f_2 are cutoff frequencies. Thus it follows that

$$\alpha = \frac{\langle(\delta\Phi_N)^2\rangle}{\ln(f_2/f_1)} \quad \rightarrow \quad S_\Phi(f) = \frac{\langle(\delta\Phi_N)^2\rangle}{\ln(f_2/f_1)}\frac{1}{f} \tag{2.89}$$

so that the rms flux noise is given by

$$\delta\Phi_N^{rms} = \sqrt{f\ln(f_2/f_1)S_\Phi(f)} \tag{2.90}$$

As first determined experimentally [76], the magnitude of the flux noise tends to flatten out at low temperatures $T < 1$ K with a value of about S_Φ^{rms} $10^{-5}\Phi_0/\sqrt{\mathrm{Hz}}$ at 1 Hz, becoming nearly independent of the SQUID parameters and materials. Thus, the rms fluctuations in $Al/AlO_x/Al$ junctions at $f = 1\,\mathrm{Hz}$ can be roughly estimated as

$$\delta\Phi_N^{rms} \approx 5.4 \times 10^{-5}\Phi_0 \tag{2.91}$$

where the frequency range $f_1 = 10^{-4}\,\mathrm{Hz}$ to $f_2 = 10^9\,\mathrm{Hz}$ has been chosen[4].

2.7 Transmon Qubits

Over the course of the last decade, superconducting qubits such as the Cooper pair box [67, 34] have emerged as some of the most promising candidates for quantum information processing. Their excellent scalability properties and natural potential for strong and fast inter-coupling are features that other implementations are struggling with [48, 81]. Superconducting qubits are, however, still solid state systems and thus the electromagnetic, thermodynamic and mechanical environment can (and will) also couple strongly to them. The resulting short coherence times represent the main obstacle towards feasible quantum error correction and scalable quantum computation.

Two complementary approaches exist towards tackling this problem. On the one hand, the systematic investigation of materials and junction properties to control and eliminate different types of loss and 1/f noise (see section 2.6) has the potential to improve virtually all types of superconducting qubits [74, 75, 82]. On the other hand, the development of devices that are by design and operation insensitive to certain sources of decoherence represents an elegant approach that strongly benefits the specific type of qubit under investigation. This approach has already led to significant improvements in coherence times through so-called *sweet spot* operation in Cooper pair boxes [63]. Moreover, it has recently led to the development of a new generation of superconducting charge qubits, the *transmission line shunted plasma oscillation qubit* or *transmon* [69, 70]. This novel type of charge qubit has been used in all of the experiments in this thesis and thus we will spend some time on explaining and discussing its properties.

In the first part of this section, the main decoherence mechanisms in superconducting charge qubits will be reviewed, closely following the excellent discussions given in Refs. [71], [64] and [83] . The second part will focus on the measures that can be taken to suppress some of these

[4] The results are only weakly sensitive to this choice.

mechanisms and a charge noise insensitive qubit design is derived from the Cooper pair box following Ref. [69].

2.7.1 Decoherence in Charge Qubits

In the context of quantum computation, decoherence refers to the mechanisms that cause a quantum bit to lose its information content to the environment. Most generally, there are two qualitatively different forms of decoherence in open quantum systems, *energy relaxation* and *dephasing*. Although they sometimes have identical sources, they cause changes in different quantum-mechanical properties describing a qubit. Here, we follow the Bloch-Redfield approach [84] which describes the dynamics of a two-level system in terms of the two rates $\Gamma_1 = T_1^{-1}$ (energy relaxation) and $\Gamma_2 = T_2^{-2}$ (dephasing).

Energy Relaxation T_1

Energy relaxation and heating are processes causing incoherent changes of the qubit state. That is, the interaction with an environmental noise bath causes the qubit to flip randomly between its two possible states. This is most generally described by the quantity T_1, the characteristic time over which a qubit is excited and de-excited by the environment. It is defined by the inverse of the corresponding excitation and de-excitation rates [83]

$$T_1 = \frac{1}{\Gamma_\uparrow + \Gamma_\downarrow} \,. \tag{2.92}$$

This type of decoherence is a consequence of the fact that all physical realizations of quantum information are in reality *open* rather than *closed* quantum systems. To which extent a closed system can be realized ultimately depends on how well it can be isolated from the environment. A powerful and universal approach for describing coupling and information leakage to the environment is the Kraus or super-operator formalism [25, 85] . This representation allows to describe the dynamics of a principal quantum system (the qubit) without having to explicitely consider properties of the environment. Everything one needs to know is wrapped up in a superoperator acting on the density operator of the qubit only

$$\Lambda : \rho_A(0) \to \Lambda(\rho_A) = \sum_m M_m \rho_A(0) M_m^\dagger \tag{2.93}$$

where M_m are the Kraus operators that summarize the effect of the environment and act only on the qubit state space. The $M_m = \langle m|U_{AB}|0\rangle_B$ are determined by the matrix elements of the time evolution operator of the whole system calculated with the basis states of the environment. In this way, the environment itself is traced out and all that remains is the perturbed time evolution of the qubit. Thus all that is needed is the interaction Hamiltonian of qubit and environment.
For the specific case of superconducting charge qubits, we can explicitly identify some of the effects of the environment and write down the corresponding interaction terms [83]. In general, relaxation is considered as a perturbation that couples a qubit operator ξ to an environment or

noise bath operator B

$$H_I = \xi B\,. \tag{2.94}$$

Here, ξ corresponds to the specific variable of the qubit that is affected by a certain type of noise. In a general framework [86], the qubit operator ξ either contains σ_z or $\sigma_\perp = \sigma_x + \sigma_y$ components, depending on the type of decoherence that is caused by a given noise source. Energy relaxation (T_1) refers to the decay of the diagonal z component of the qubit density matrix while dephasing (T_2) describes the decay of the off-diagonal part [86, 25]. Using the general approach (2.94), the relaxation rate corresponding to (2.92) is to a good approximation given by [83]

$$\Gamma_{\uparrow\downarrow} = \frac{1}{\hbar^2}\,|\langle g|\xi|e\rangle|^2\,S_B(\mp\omega_a) \tag{2.95}$$

where Fermi's golden rule was used and $S_B(\mp\omega_a)$ denotes the noise spectral density of the environment at the qubit transition frequency.
Consider for instance the case of noise on the gate voltage $\mathrm{V_g} = \overline{\mathrm{V}}_\mathrm{g} + \delta\mathrm{V_g}$ that is used to control the charge bias n_g of the Cooper pair box. This noise is simply the Johnson noise that results from the ohmic environment of the CPB. This type of noise is thermal in nature and causes random motion of charge carriers. It affects the number of charges on the island N and couples to it via the gate capacitance C_g. Thus we can write

$$\xi_V = 2e\frac{C_g}{C_\Sigma}\delta V_g N\,. \tag{2.96}$$

Note that this operator can also be equivalently written in terms of the operator σ_z (see Eqs.(2.64) and (2.65)). The spectral density in this case is simply the Johnson-Nyquist expression for a dissipative circuit element (e.g. a resistor or the ohmic lines connected to the qubit) [83]

$$S_V(\omega) = \frac{2\hbar\omega\mathrm{Re[Z]}}{1 - e^{-\hbar\omega/k_bT}} \tag{2.97}$$

where $Z = Z(\omega)$ is the environment impedance. δV_g ultimately causes fluctuations in the gate charge and translates directly to energy relaxation via [71]

$$\Gamma_V = \frac{2\pi g^2}{\sqrt{[4E_{C0}(1-n_g)]^2 + E_{J0}^2}} \tag{2.98}$$

where we have used the two-state approximation for the CPB and g denotes the coupling strength to the ohmic environment. These gate voltage fluctuations do, however, also lead to random changes in the qubit transition frequency (2.69) and are thus also a source of the second form of decoherence, dephasing. Although not discussed explicitly here, this is in fact true for all mechanisms causing energy relaxation [5].

[5] Apart from the example of voltage noise discussed here, there are ample other causes for energy relaxation such as quasi-particle, inductive or radiative material loss which are explained in detail elsewhere [71, 74, 86].

Dephasing T_2

Dephasing refers to processes that cause a qubit to accumulate a random phase rather than to change its quantum state directly. In charge qubits, dephasing mainly arises from the intrinsic low frequency 1/f junction noise discussed in section 2.6 as well as from thermal Johnson noise. Although dephasing of overall phases is irrelevant, this form of decoherence more importantly changes the relative phase in superpositions of two states. Here, the quantity T_2 is the characteristic time scale over which the qubit accumulates a random phase shift of π.
The phase is determined by the frequency and thus the root of dephasing lies in fluctuations of the qubit transition. For the general case of a split Cooper pair box, the qubit transition frequency (2.73)

$$\hbar\omega_a = \sqrt{E_{J\Sigma}(\cos^2(\pi\Phi/\Phi_0) + d^2\sin^2(\pi\Phi/\Phi_0)) + 16E_C^2(1-n_g)^2} \tag{2.99}$$

depends on a number of different parameters. Fluctuations in all of these parameters ultimately contribute to dephasing. In particular, this means that all mechanisms of energy relaxation are also responsible for dephasing. Since dephasing describes the decay of the amplitude of a quantum state, energy relaxation contributes a factor of $\Gamma_{T1}/2$. This in turn also sets a dissipation-imposed upper limit for the dephasing time of $T_2 = 2T_1$.

Some general formulae valid for arbitrary parameters are readily derived [86, 71]. Let the frequency fluctuations $\delta\omega_a$ depend on the parameter η. Expanding this general fluctuation around η_0 gives

$$\delta\omega_a = \delta\eta\left(\frac{\partial\omega_a}{\partial\eta}\right)_{\eta_0} + \frac{\delta\eta^2}{2}\left(\frac{\partial^2\omega_a}{\partial\eta^2}\right)_{\eta_0} + \ldots \tag{2.100}$$

with the corresponding variance

$$\langle\delta\omega_a^2\rangle = \sigma_\eta^2\left(\frac{\partial\omega_a}{\partial\eta}\right)_{\eta_0}^2 + \frac{\sigma_\eta^4}{4}\left(\frac{\partial^2\omega_a}{\partial\eta^2}\right)_{\eta_0}^2 + \ldots \tag{2.101}$$

where the standard deviation of the parameter $\sigma_\eta = \sqrt{\langle\delta\eta^2\rangle}$ was introduced. The dimensionless dephasing rate due to noise in η then reads

$$\Gamma_\phi = \frac{1}{\omega_a T_2^\eta} = \frac{1}{\omega_a}\sqrt{\langle\delta\omega_a^2\rangle}\,. \tag{2.102}$$

In conventional Cooper pair boxes, noise in the gate charge parameter $\eta = n_g$ is the dominant contribution to dephasing. There are both intrinsic as well as extrinsic forms of charge noise and three different types can be distinguished. The first type is the Johnson gate voltage noise (2.97) discussed above which results from thermal fluctuations in the motion of charge carriers. Furthermore, Josephson junctions suffer from the intrinsic $1/f$ charge noise presented in section 2.6. The third contribution comes from the resistive quasi-particle currents present in junctions

[86]. From (2.99) and (2.102) we find for the first order contribution of charge noise at $\Phi = 0$

$$\Gamma_\phi = \sigma_{n_g} \frac{(n_g - 1)}{(n_g - 1)^2 + \left(\frac{E_J}{4E_C}\right)^2} . \tag{2.103}$$

The variance σ_{n_g} is different for each type of charge noise and can be calculated from the corresponding spectral noise density [87].
The second important contribution to dephasing results from fluctuations in the parameter $\eta = \Phi$, i.e. the flux bias used to tune the qubit transition. We find for the first order contribution from flux noise

$$\Gamma_\phi = \frac{\pi \sigma_\Phi}{2\Phi_0} \frac{E_J^2}{\hbar \omega_a^2} (1 - d^2) \sin\left(\frac{2\pi\Phi}{\Phi_0}\right) . \tag{2.104}$$

The third parameter in the qubit transition that is subject to noise is the Josephson energy $E_{J\Sigma} = E_{J1} + E_{J2}$ itself. This results from the intrinsic 1/f fluctuations of the critical currents discussed in section 2.6. It follows for the corresponding dephasing rate

$$\Gamma_\phi = \frac{E_J}{\hbar \omega_a^2} \left[\cos^2\left(\frac{\pi\Phi}{\Phi_0}\right) + d^2 \sin^2\left(\frac{\pi\Phi}{\Phi_0}\right)\right] . \tag{2.105}$$

As shown in the following, it is possible to reduce dephasing in superconducting qubits to a certain extent by means of adequate qubit design.

2.7.2 The Transmon: A Charge Insensitive Qubit Design

Major efforts have been taken since the first experimental realizations of the Cooper pair box to understand and control the sources of dephasing and energy relaxation discussed above. These have brought about the notion of specific operating points in the CPB parameter space that allow eliminating first order contributions to decoherence [63]. These points are often referred to as *sweet spots* and can be directly inferred from the corresponding first order dephasing rates. The charge noise contribution (2.103) vanishes at the gate charge sweet spot $n_g = 1$. Unsurprisingly, the energy bands in Fig. 2.8 have maxima and minima at these sweet spots and the Cooper pair box becomes first-order insensitive to charge fluctuations. Operating the CPB at this point has led to significant improvements in coherence times [63]. For flux noise, (2.104) goes to zero at the sweet spots $\Phi = 0$ and $\Phi = \Phi_0/2$. Permanently operating at these points does, however, nullify the tuning ability of the CPB. For critical current noise (2.105) there exists no sweet spot, which ultimately results from the fact that there must always be at least one parameter that sets the absolute energy scale $\hbar\omega_a$ [71].
Although we can eliminate first order charge noise by biasing the qubit at $n_g = 1$, there are still higher order terms that effectively cause dephasing. Naturally, the question arises whether it is possible to (a) eliminate higher order contributions and (b) find a regime were all of them are suppressed simultaneously. Considerations in this direction have led to the development of the transmission line shunted plasma oscillation qubit, the so-called *transmon*. It was theoretically proposed in [69], experimentally invesitgated in [70] and already successfully used in a number

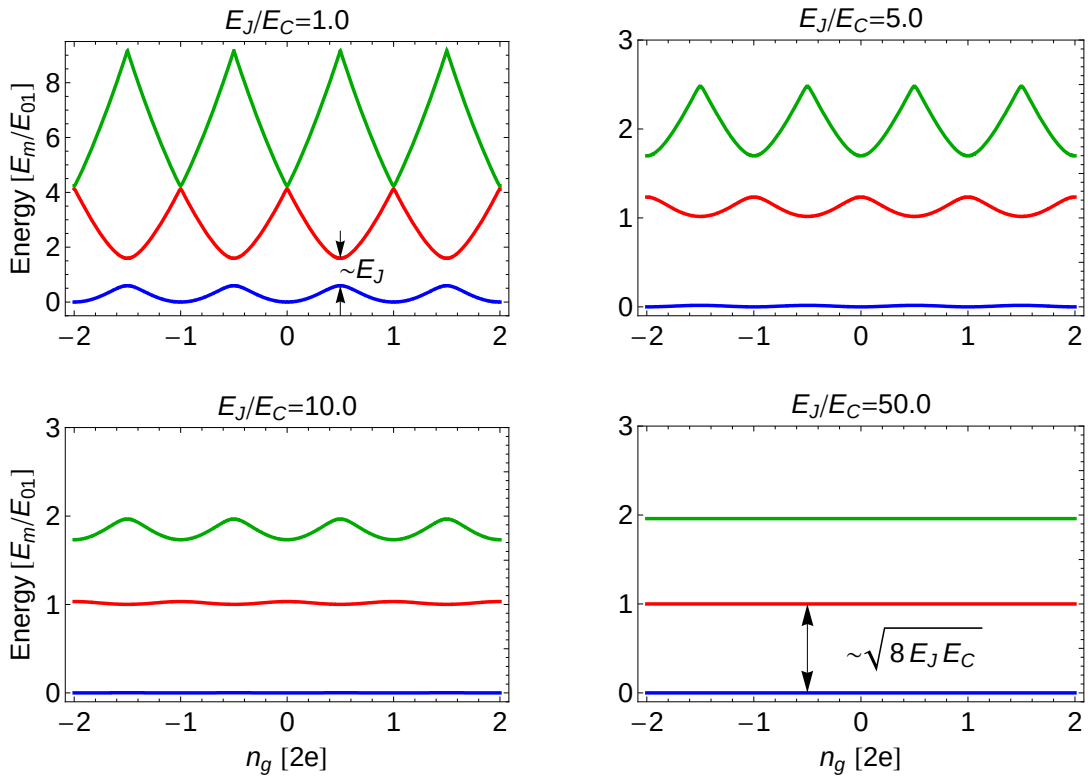

Figure 2.10: Eigenenergies of the Cooper pair box for different ratios of Josephson to coupling energy.

of hallmark experiments [5, 9, 6, 88]. The transmon represents a type of qubit derived from the Cooper pair box whose sensitivity to charge noise can be controlled by design. In particular, it has become possible to eliminate terms of higher orders in the charge noise dephasing rate and hence to fabricate qubits with a 'permanent' sweet spot.

The most crucial quantities of a Cooper pair box are its energy level anharmonicity and its charge dispersion. While the latter one determines the sensitivity of the energy levels to variations in the gate voltage and to charge noise, sufficient anharmonicity is a stringent requirement to avoid higher level excitations and allow for qubit operation. As we will see in a moment, both quantities depend on the ratio of Josephson to charging energy ($E_\mathrm{J}/E_\mathrm{C}$). Let's start by re-considering the eigenenergies of the Cooper pair box derived in section 2.5.1, where it was found in the phase basis

$$E_m(n_g) = E_{C0}\mathcal{M}_\mathrm{A}(2[n_g + k(m, n_g))])\,(-E_{J0}/2E_{C0}) \tag{2.106}$$

with $\mathcal{M}_\mathrm{A}$ denoting Mathieu's characteristic value and $k(m, n_g)$ an eigenvalue sorting function [69, 64]. The first three energy levels $m = 0, 1, 2$ are plotted in Fig. 2.10 for different ratios ($E_\mathrm{J}/E_\mathrm{C}$) as function of the gate charge n_g. Going from small to large ratios, we observe that the dependence on charge decreases rapidly. The energy bands tend to flatten out until a point where the eigenenergies of the Cooper pair box become almost independent of n_g. Consequently, the Cooper pair box also becomes less and less sensitive to charge fluctuations. For large ratios of Josephson to charging energy of a few tens to a hundred we enter a region of 'permanent' sweet spots. This can be seen explicitly from the asymptotic charge dispersion of the Cooper

pair box in the limit $E_J/E_C \gg 1$ [69]

$$\epsilon_m \approx (-1)^m E_C \frac{2^{4m+5}}{m!}\sqrt{\frac{2}{\pi}}\left(\frac{E_J}{2E_C}\right)^{\frac{m}{2}+\frac{3}{4}} e^{-\sqrt{8E_J/E_C}} \tag{2.107}$$

which gives the peak to peak value for the charge dispersion of the mth level. As can be seen, the charge dispersion decreases exponentially with increasing ratio of Josephson to charging energy. The sensitivity to changes in the gate charge is drastically reduced as the large Josephson energy starts to dominate over the electrostatic energy. As a consequence it seems possible to realize 'charge' qubits with large ratios of (E_J/E_C) that are in fact independent of charge and thus also charge noise. This is the underlying observation that led to the development of the transmon, an improved version of the Cooper pair box. While typical CPBs are operated in a regime where $E_J/E_C < 1$, the transmon by design has a strongly decreased charging energy and is thus operated in a region in parameter space where $E_J/E_C \gg 1$. This creates a 'permanent' sweet spot over the whole range of n_g values and makes the transmon virtually insensitive to any form of charge noise. Of course charge can no longer be used as a control parameter in the transmon. But then again this control parameter has become completely obsolete since its initial purpose, the compensation of offset charges and fluctuations, is also void now (see section 2.5.1). Operating in a regime of $E_J/E_C \gg 1$ naturally comes with a number of drawbacks.
As the energy bands in Fig. 2.10 flatten out for increasing ratio (E_J/E_C), it can be seen that not only the charge dispersion but also the anharmonicity of the levels decreases. In other words, a decrease in level anharmonicity is the price to pay for a gain in charge-noise insensitivity. To see how severe this loss in anharmonicity is and if it affects qubit operation, we can expand the Josephson cosine potential in the Hamiltonian (2.52) to fourth order and treat the quartic term perturbatively [6], which yields the approximate eigenenergies [69]

$$E_m \approx -E_J + \sqrt{8E_J E_C}\left(m+\frac{1}{2}\right) - \frac{E_C}{12}(6m^2+6m+3)\,. \tag{2.108}$$

The relative anharmonicity of the first two levels is defined as

$$\alpha_r = \frac{E_{12}-E_{01}}{E_{01}}\,. \tag{2.109}$$

Using the approximate result for E_m, we find

$$\alpha_r \approx -(8E_J/E_C)^{-1/2}\,. \tag{2.110}$$

Thus, in contrast to the charge dispersion (2.107), the anharmonicity decreases only with a weak power law in the Josephson to charging energy ratio. This in turn makes it possible to find a range of values E_J/E_C with strongly decreased charge noise insensitivity as well as sufficiently large degrees of anharmonicity so that one does not have to compromise on qubit operation. A comparison of the numerically exact result (using Mathieu functions) and the approximate result for both the relative $\alpha_r(E_J/E_C)$ and absolute anharmonicity $\alpha(E_J/E_C)$ is

[6] In complete analogy to the treatment of the SQUID non-linearity in section 2.4.2.

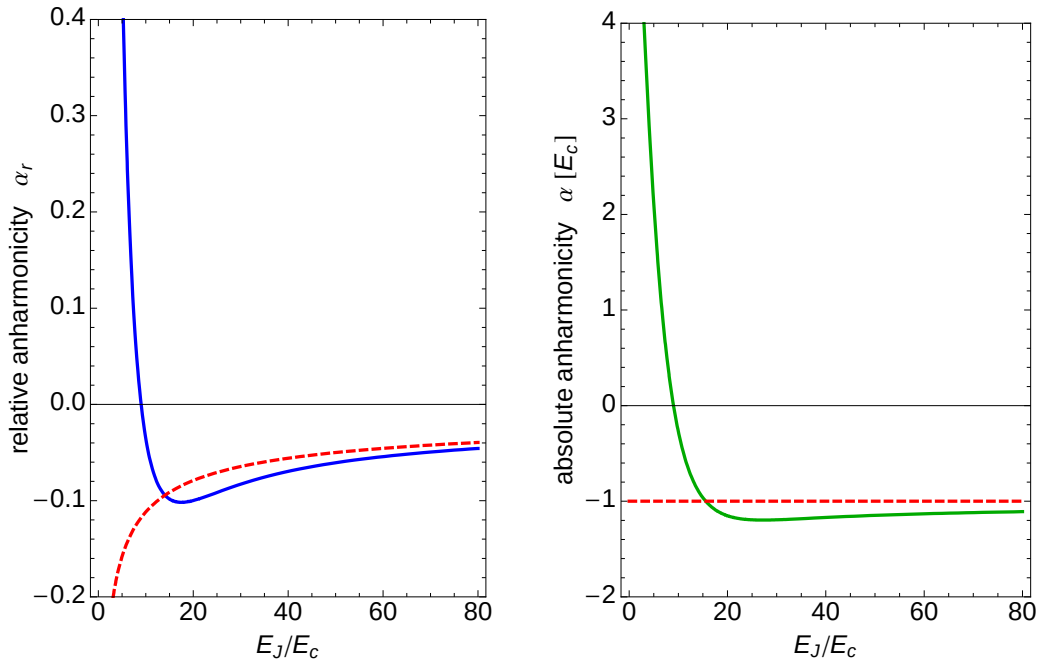

Figure 2.11: Absolute (right) and relative (left) anharmonicity of the transmon as a function of the ratio E_J/E_C: exact calculations (blue and green solid lines), approximate expression (2.110) (dashed red).

given in Fig. 2.11. Going from the Cooper pair box regime $E_J/E_C < 1$ towards the transmon regime $E_J/E_C > 1$, the relative anharmonicity changes sign at $E_J/E_C \sim 9$ and reaches a shallow minimum around $E_J/E_C \sim 20$. The sign change indicates that the transition energies decrease for increasing quantum number m, in particular we have $E_{01} > E_{12}$. For typical transmon ratios of $E_J/E_C \sim 50$ this is indeed the case. Note that the anharmonicity of a many-level system used as a qubit ultimately sets a lower bound on the duration of the pulses that can be used to control the qubit. In practice, coherent qubit control requires pulse lengths that are small compared to T_1 and T_2. The minimum pulse duration is approximately set by the anharmonicity as $\tau_p \sim 1/|\omega_{01}\alpha_r|$ [69]. For typical pulse lengths on the order of 10 ns, the minimum anharmonicity for a $\omega_{01}/2\pi = 10$ GHz qubit can be estimated as $|\alpha_r| \sim 1/200\,\pi$ [69]. In terms of the energy ratio, this gives a large range of possible values $20 \lesssim E_J/E_C \ll 5 \times 10^4$ where the qubit's charge noise sensitivity is significantly decreased without having to compromise on operational speed. This was confirmed by recent experimental investigations presented in Ref. [70], where coherent control of transmon qubits with T_2 times exceeding 2 μs was demonstrated. This already approaches the limit $T_2 = 2T_1$ imposed by energy relaxation.

The discussion above clearly showed that an improved CPB design with $E_J/E_C \gg 1$ has the potential to yield significantly increased coherence times. So how does one actually realize such an increased energy ratio? Recalling the expressions for the charging energy from section 2.5.1

$$E_C = \frac{2e^2}{2C_\Sigma} \quad , \quad C_\Sigma = C_g + C_J + C_s \,, \tag{2.111}$$

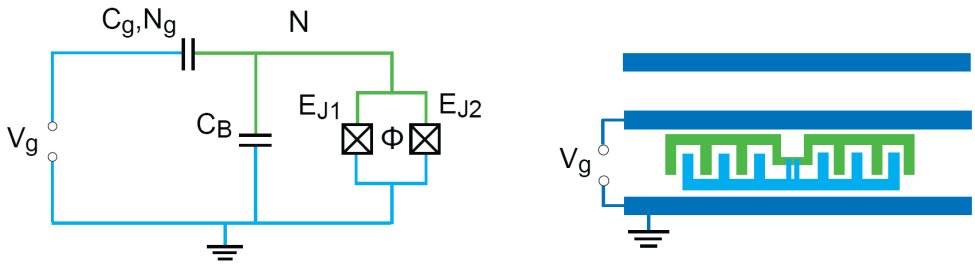

Figure 2.12: Reduced circuit diagram and sketch of a transmon capactively coupled and shunted to a transmission line resonator.

Figure 2.13: Optical microscope picture of a transmon qubit fabricated in the clean room facilities at ETH Zurich.

we see that the ratio E_J/E_C can be made larger by means of increasing the total capacitance of the CPB design. This is readily achieved by adding a parallel capacitor C_B to the CPB circuit, as shown in Fig. 2.12. In practice, transmons are coupled to and operated inside transmission line resonators (see chapter 3), forming circuit QED systems (chapter 4). As shown in the sketch in Fig. 2.12 , the parallel capacitor C_B is then realized as a large shunt capacitance with a finger like structure. An optical microscope picture of a realized transmon qubit is shown in Fig. 2.13. The transmons used in the experiments presented in chapter 5 have been exclusively fabricated in the clean room facilities at ETH Zurich and part of this thesis was to characterize the Josephson junctions in our fabrication process.

3 Superconducting Tunable Cavities

The strong coupling of a Cooper pair box qubit to a coplanar waveguide cavity marked a major milestone on the road towards solid-state quantum computation and triggered a whole new exciting field of research, now known as *circuit quantum electrodynamics* [1, 2, 3]. While superconducting charge, phase and flux qubits have been actively investigated for more than a decade [33, 34, 39, 63, 64, 65, 66], only recently it was demonstrated that these systems can be coherently coupled to single microwave photons stored in a transmission line resonator [2]. The notion that quasi one-dimensional coplanar transmission lines can be used to realize ultra-high Q cavities with large rms electric field strengths [3] has ultimately allowed for the implementation of a solid-state analog of traditional, atomic cavity quantum electrodynamics [14, 22].
Up to this point, transmission line resonators have been successfully coupled to both charge and phase qubits [19] and have by now become a standard tool for qubit readout in these experiments. These resonators have well-defined, fixed resonance frequencies ω_r which are primarily determined by their length. A major part of this thesis was devoted to the development and implementation of a novel type of transmission line resonator whose resonance frequency can be *dynamically tuned* over a considerable portion of the microwave spectrum. These devices have the potential to add a new dimension to circuit QED experiments, going as far as turning the resonator itself into a qubit [89].
The first part of this chapter focuses on 'conventional' transmission line resonators and the models that can be used to describe them. In the second part the focus is shifted to the novel type of tunable cavity developed in the framework of this thesis and also in Refs. [90, 11]. Various models ranging from simple electrical circuit mapping to a full second quantization are presented and the chapter is rounded off by a discussion of the practical constraints on the design, fabrication and operation of these new devices.

3.1 Transmission Line Resonators

Superconducting transmission line (TL) resonators represent the electrical circuit analog of optical cavities in the microwave regime. The radiation field in an optical cavity realizes a quantum harmonic oscillator. An atom placed inside such a cavity then strongly couples to the one mode of the radiation field that is close to its transition frequency (see section 4.1.1). If well separated, all other modes can be neglected to a good approximation since they couple only very weakly to the atom's relevant transition [14, 22].
In the electrical circuit analog presented in this thesis, a superconducting charge qubit (section 2.5) plays the role of the atom, while the single-mode harmonic oscillator is realized by a trans-

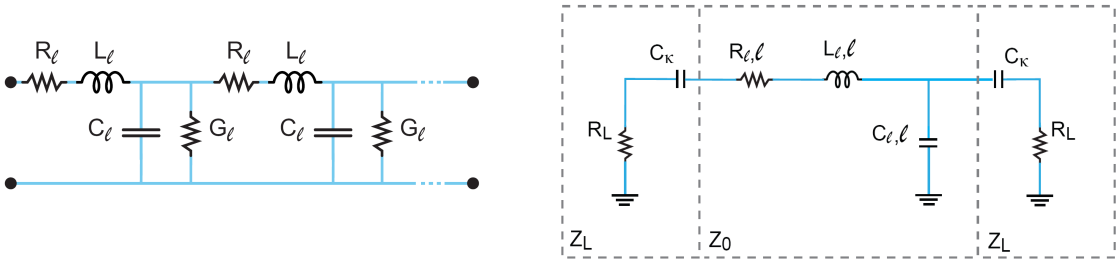

Figure 3.1: Lumped element model for transmission lines (left) and transmission line capacitively coupled to a load impedance, see discussion in the text.

mission line cavity. In fact, there are many possible ways to realize a harmonic oscillator circuit, most prominently in the form of a simple lumped LC circuit. In the microwave domain, however, we are dealing with wavelengths on the order of 100 μm $\leq \lambda \leq$ 1 m and thus a true lumped element oscillator is somewhat hard to realize in this regime. Since we want to be able to measure the circuit, we have to attach wires to it which extend more than a wavelength and thus there is almost inevitably one large dimension present. To a good approximation, a transmission line resonator is the distributed element version of an LCR oscillator. Such a distributed element construction avoids uncontrolled stray inductances and capacitances and allows for better microwave properties than lumped element resonators.

3.1.1 Lumped Element and LC Oscillator Model

Standard circuit theory[1] makes the assumption that the electrical wavelengths are a lot larger than the dimensions of a given network [91]. If this is not the case, the phase of the current or voltage can change significantly over the length of a device and can thus no longer be ignored. In the microwave regime, the dimensions of the typical devices used are on the order of a wavelength and hence we are in a situation where standard circuit theory can in general not be applied. However, it is possible to give at least an approximate description in terms of circuit theory without having to resort to Maxwell's equations [91].
In its broadest sense a transmission line is simply a parallel pair of two conductors, the most common example being a regular coaxial cable. Naturally, each of the two conductors has self-inductance, which can be described by a self-inductance L_ℓ per unit wire length Δx. Analogously, each wire has losses due to finite conductivity and possible dielectric losses which can be modeled with a resistance R_ℓ and a shunt conductance G_ℓ, both per unit wire length. Additionally, the wires are usually quite close which implies a shunt capacitance C_ℓ per Δx. Thus for discrete Δx, a small incremental length of transmission line can be modeled by a circuit of the form as depicted in Fig. 3.1a. Therefore the total transmission line can be described by an infinite series of lumped-element circuits. Now simply applying Kirchhoff's rules to the circuit in Fig. 3.1 a, taking the limit $\Delta x \to 0$ and separating the time component gives the one dimensional

[1] That is, Ohm's law and Kirchhoff's rules.

differential equations

$$\frac{dU(x)}{dx} = -(R_\ell + i\omega L_\ell)I(x) \quad , \quad \frac{dI(x)}{dx} = -(G_\ell + i\omega C_\ell)U(x) \tag{3.1}$$

with the current and voltage at an arbitrary point x of the transmission line

$$U(x) = U_0^+ e^{-\gamma x} + U_0^- e^{\gamma x} \quad , \quad I(x) = I_0^+ e^{-\gamma x} + I_0^- e^{\gamma x} \,. \tag{3.2}$$

The signals on a transmission line propagate as waves of the form (3.2) with propagation coefficient

$$\gamma = \sqrt{(R_\ell + j\omega L_\ell)(G_\ell + j\omega C_\ell)} \,. \tag{3.3}$$

The imaginary part $\beta = \mathrm{Im}[\gamma]$ defines the phase velocity $v_{\mathrm{ph}} = \omega/\beta$ and wavelength $\lambda = 2\pi/\beta$ whereas the real part $\alpha = \mathrm{Re}[\gamma]$ describes the attenuation of the waves. The characteristic impedance of a transmission line, i.e. the impedance of one small section of unit length, is then given by

$$Z_0 = \pm\frac{U_0^\pm}{I_0^\pm} = \sqrt{\frac{R_\ell + j\omega L_\ell}{G_\ell + j\omega C_\ell}} \,. \tag{3.4}$$

For the nearly lossless case, all of this simplifies to

$$\gamma = j\omega\sqrt{L_\ell C_\ell} \quad , \quad v_{\mathrm{ph}} = \sqrt{\frac{1}{L_\ell C_\ell}} \quad , \quad Z_0 = \sqrt{\frac{L_\ell}{C_\ell}} \,. \tag{3.5}$$

A piece of transmission line terminated at both ends by a load impedance Z_L represents a distributed resonant circuit. As depcited in Fig. 3.1b, the total load impedance consists of a capacitance C_κ via which the electromagnetic waves, i.e. the photons, can couple into the resonant circuit as well as the resistance $R_L \sim 50\,\Omega$ of the input/output lines. The effective input impedance at a distance ℓ from the terminating load impedance is given by [91]

$$Z_{\mathrm{in}} = Z_0 \frac{Z_L + Z_0 \tanh\gamma\ell}{Z_0 + Z_L \tanh\gamma\ell} \tag{3.6}$$

and if the load impedance is an open ($Z_L = \infty$) this simplifies to

$$Z_{\mathrm{in}}^{\mathrm{open}} = Z_0 \coth\gamma\ell = Z_0 \frac{1 + j\tan\beta\ell\tanh\alpha\ell}{\tanh\alpha\ell + j\tan\beta\ell} \,. \tag{3.7}$$

The corresponding $\ell = n\lambda/2$ resonances are then given by

$$\omega_n = \beta v_{\mathrm{ph}} = \frac{2\pi}{\lambda} v_{\mathrm{ph}} = \sqrt{\frac{1}{L_\ell C_\ell}}\frac{n\pi}{\ell} \tag{3.8}$$

where $n \in \mathbb{N}/0$ is the mode index. Thus the resonance frequency of a lossless transmission line resonator is determined by its length and its inductance and capacitance per unit length. As will be shown in the following sections, all of these quantities can be controlled by design, allowing to realize cavities with specific, well-defined resonance frequencies. A transmission line resonator

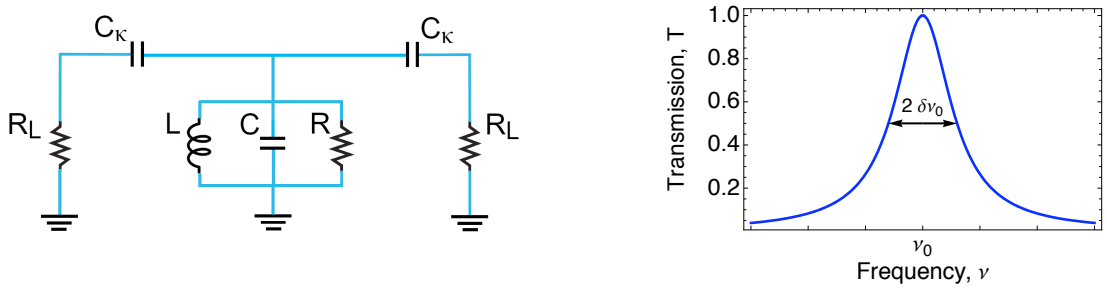

Figure 3.2: (a) LCR oscillator coupled capacitively and symmetrically to an external load R_L. Typical Lorentzian transmission spectrum of an LCR oscillator circuit.

is a distributed element version of the well-known LC oscillator and, as shown below, we can effectively map the distributed realization onto its lumped element counterpart. This so-called mapped LCR model provides for an intuitive picture of the resonator and its properties and it will moreover show that a transmission line resonator can realize a quantum harmonic oscillator.

Mapped LCR-Oscillator Model

A transmission line resonator behaves around its resonance frequency effectively like a parallel combination of a lumped inductance, capacitance and resistance, where L, C and R can be expressed in terms of the quantities per unit length of the transmission line. By mapping the lumped element model for transmission lines onto such a simple LCR-oscillator, a set of relations for fast and fairly reliable calculations of the most important resonator properities can be written down. Such a mapped LCR approximation is valid for frequencies around resonance $\omega \approx \omega_n$ and provides for an intuitive understanding of the resonator properties and the effects of coupling the resonator to an input/output line.
Fig. 3.2a shows a LCR oscillator coupled capacitively and symmetrically to an external load R_L via an input/output capacitance C_κ. Neglecting the load for the moment, the differential equation of motion for the charge q in this circuit follows directly from Kirchhoff's rules

$$\frac{d^2q}{dt^2} - \frac{1}{RC}\frac{dq}{dt} + \frac{q}{LC} = 0 \tag{3.9}$$

with the solution

$$q(t) = q_0 \exp\left[i\omega_0 t - \frac{\kappa}{2}t + \phi\right] . \tag{3.10}$$

Thus the charge in this circuit oscillates with frequency $\omega_0 = 1/\sqrt{LC}$ and decays at a rate of $\kappa = 2/RC$, which describes the damping of the oscillation. The corresponding internal quality factor $Q_{\text{int}} = \omega_0/(2\pi\kappa)$ gives the number of oscillations per decay time $T_\kappa = 1/\kappa$. The total impedance of the circuit Fig. 3.2 a reads

$$Z_{\text{LCR}} = \left(\frac{1}{R_L} + \frac{1}{R} + j\left(\omega(C + C_\kappa - \frac{1}{\omega L}\right)\right)^{-1} \tag{3.11}$$

where the imaginary part vanishes at the resonance frequency of the circuit $\omega = \omega_0$. These resonances have a Lorentzian line shape and their half width at half maximum is expressed by the quality factor $\delta\nu = \nu_0/2Q$, see Fig. 3.2b. A high Q resonant circuit will thus have sharp, narrow resonances and oscillates many times before it decays, whereas a low Q circuit has a broad linewidth and decays much more quickly. For the full circuit of Fig. 3.2a including the coupling environment, the total quality factor is the parallel combination of the internal and external quality factors

$$\frac{1}{Q_L} = \frac{1}{Q_{\text{int}}} + \frac{1}{Q_{\text{ex}}} \tag{3.12}$$

where the external quality factor for symmetric coupling reads [92]

$$Q_{\text{ex}} = \frac{n\pi}{4Z_0}\left(\frac{1}{C_\kappa^2 R_L \omega_n^2} + R_L\right) . \tag{3.13}$$

For large coupling capacitances, Q_{ex} becomes small and the loaded quality factor is dominated by the external contribution $Q_L \sim Q_{\text{ex}}$. On the other hand, weak coupling to the input/output lines yields a large external quality factor and we have $Q_L \sim Q_{\text{int}}$. The external and internal quality factors also determine the insertion loss L_0, which gives the peak transmission of the resonant circuit. It can be expressed using the coupling coefficient g:

$$L_0 = \frac{g}{g+1} = \frac{(Q_{\text{int}}/Q_{\text{ex}})}{(Q_{\text{int}}/Q_{\text{ex}})+1} . \tag{3.14}$$

As pointed out in [91], the LCR impedance (3.11) can be expanded around resonance ω_0 which in turn allows for a direct mapping of the TL resonator impedance (3.7) onto Z_{LCR}. This mapping gives the following relations [91, 92]:

$$L \to \frac{1}{n}\frac{2Z_0}{\pi\omega_n} = \frac{2}{n^2}\frac{L_\ell \ell}{\pi^2} \quad , \quad C \to \frac{C_\ell \ell}{2} \quad , \quad R \to \frac{Z_0}{\alpha\ell} = \frac{1}{\alpha\ell}\sqrt{\frac{L_\ell}{C_\ell}} \tag{3.15}$$

and

$$\omega_n \to \sqrt{\frac{1}{L_\ell C_\ell}}\frac{n\pi}{\ell} \quad , \quad Q_{\text{int}} = \omega_n R_{\text{LCR}} C \to \frac{\pi}{2\alpha\ell} \tag{3.16}$$

The transmission line resonator thus behaves around its resonance effectively like a simple LCR oscillator. In this intuitive picture, the relations (3.12) - (3.16) can be used for fast and fairly precise estimates of the most important quantities of a TL resonator around resonance.

3.1.2 Quantization of the LCR Circuit

The discussion of section 3.1.1 showed that a transmission line resonator effectively behaves like a lumped LCR oscillator around its resonance. The mapping of TL properties onto oscillator quantities like L, C and R in turn allowed for an intuitive understanding of the resonator behavior and represents a convenient way to capture the physics of this system. A quantization of the LCR oscillator in turn leads directly to a harmonic oscillator Hamiltonian and thus elegantly bridges the gap between traditional microwave engineering and fundamental quantum mechanics.

	mechanical oscillator	electrical LC oscillator
momentum	$p_x(t)$	$q(t)$
position	$x(t)$	$\Phi(t)$
mass	m	C
frequency	ω	$1/\sqrt{LC}$
commutator	$[x, p_x] = i\hbar$	$[\Phi, q] = i\hbar$

Table 3.1: Correspondence table of a one-dimensional mechanical oscillator and an electrical LC oscillator circuit.

Following section 2.1, a quantum circuit is in general described by the canonical conjugate variables charge q and flux Φ with the standard commutator $[\Phi, q] = i\hbar$. For the lossless LC oscillator, charge and flux are related by the voltage across the circuit

$$V = -L\frac{\partial I}{\partial t} = \frac{q}{C} \tag{3.17}$$

and the total circuit is governed by the Hamiltonian

$$\mathcal{H}_{\mathrm{LC}} = \frac{q^2}{2C} + \frac{\Phi^2}{2L}\,. \tag{3.18}$$

Comparing this to the standard Hamiltonian of a mechanical harmonic oscillator $H = p^2/2m + (1/2)m\omega^2 x^2$ and recalling that q has the role of momentum and Φ of position, one can identifiy $\omega = 1/\sqrt{LC}$ and $m = C$. Furthermore, we can define the dimensionless creation and annihilation operators of the circuit

$$a = \frac{1}{\sqrt{2\hbar\sqrt{L/C}}}(\Phi + i\sqrt{L/C}\,q) = \frac{1}{\sqrt{2\hbar Z_0}}(\Phi + iZ_0 q) \tag{3.19}$$

$$a^\dagger = \frac{1}{\sqrt{2\hbar\sqrt{L/C}}}(\Phi - i\sqrt{L/C}\,q) = \frac{1}{\sqrt{2\hbar Z_0}}(\Phi - iZ_0 q) \tag{3.20}$$

which fulfill the standard commutation relation $[a, a^\dagger] = 1$. Thus, the Hamiltonian of the LC circuit can be written in the form of a standard harmonic oscillator Hamiltonian

$$\mathcal{H}_{\mathrm{LC}} = \hbar\omega\left(a^\dagger a + \frac{1}{2}\right)\,. \tag{3.21}$$

Furthermore, using (3.17), a voltage operator V can be introduced as

$$V = \sqrt{\frac{\hbar\omega}{2C}}(a - a^\dagger). \tag{3.22}$$

To a good approximation, a lossless TL resonator thus represents a cavity that is described by a harmonic oscillator Hamiltonian of the form (3.21). From a quantum optics point of view, each set of values of $\{\Phi, q, L, C\}$ represents a certain mode of the cavity with an average photon number $\langle n\rangle = a^\dagger a$. The operator V can be thought of as a quantum voltage generated by the photons inside the cavity. The analogy of a one-dimensional mechanical oscillator such as a

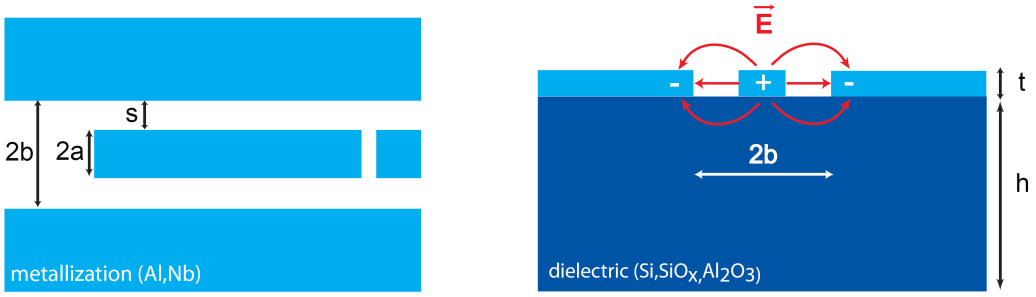

Figure 3.3: Schematic sketch of a coplanar waveguide: Top view (left) and side view (right). Here, h denotes the substrate thickness, $2a$ the width of the center conductor, $2b$ the spacing between the two ground planes and t the thickness of the metallization. The materials used in this thesis are indicated accordingly.

massive particle moving in a harmonic potential and a resonant LC circuit is expressed in the correspondence table Tab. 3.1.

3.1.3 Physical Implementation: Coplanar Waveguide Cavities

In the discussion so far, the transmission line resonator was treated conceptually as a parallel pair of two (not further specified) conductors terminated by a load impedance on both ends. When realizing a transmission line resonator, a certain physical implementation has to be chosen. As can be expected from the universality of the concept, there exist many different realizations [91]. For the experiments presented in this thesis, we have realized transmission line resonators in the form of superconducting coplanar waveguide cavities. A coplanar waveguide (CPW) is a quasi one-dimensional structure that can be thought of as a planar version of a coaxial cable [93]. The first realizations date back to the late sixties and today CPWs are used in a vast number of different applications ranging from amplifiers and mixers to photonic bandgap structures and communication technology [94].

Most generally, a CPW on a dielectric substrate of thickness h consists of a center strip conductor of width $2a$ with quasi-infinite, parallel ground planes on either side separated by $2b$ as sketched in Fig. 3.3. Such a structure supports a transversal electromagnetic mode of wave propagation (TEM_{nm}), i.e. it represents a one-dimensional transmission line just like the one discussed in section 3.1.1. To realize a cavity from such a structure, the CPW is terminated on both ends by a capacitor in the form of a simple gap or finger structure whose geometric properties are used to design the magnitude of input/output coupling. Optical microscope pictures of a typical CPW cavity and capacitor structures are shown in Fig. 3.4. These resonators were fabricated in the clean room facilities of ETH Zurich using standard micro lithographic techniques. The detailed process is described in Refs .[92, 95]. We typically use a center conductor width of $2a = 10\,\mu$m and a ground plane separation of $2b = 19\,\mu$m which gives a characteristic impedance of $Z_0 \cong 60\,\Omega$ that is matched with all other microwave components in our setup. All of the measurements presented here were performed using either Aluminum or Niobium as superconducting metallization, the latter one having the highest critical temperature

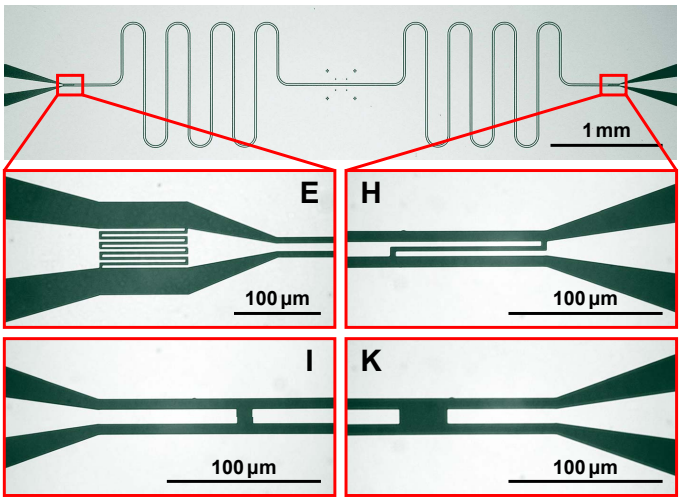

Figure 3.4: Optical microscope picture of an Aluminum coplanar waveguide resonator. The positions of the capacitors for input/ouput coupling are indicated by the red squares and some example finger and gap capacitor structures are depicted below (taken from [92]).

of all known elemental metals [2] $T_c = 9.2\,\mathrm{K}$. The metallization has a thickness of roughly 200 nm on a subtrate of $h = 500\,\mu\mathrm{m}$. As substrate materials we use Si, SiO_x as well as sapphire Al_2O_3. The well-established nano- and micro fabrication techniques used for realizing these cavities allow us to engineer many of the characteristic resonator parameters at will and to design and produce tailor-made devices with a fairly high degree of control, a subject adressed in a design study conducted as a sideproject to this thesis, see Ref. [92]. Important resonator properties such as the characteristic impedance Z_0, the quality factor Q or the resonance frequency are all be determined in terms of the geometric CPW parameters, as can be seen from a so-called conformal mapping description of the system.

3.1.4 Conformal Mapping and Scattering Matrix Description

While the mapped LCR-model of section 3.1.1 gives good results around resonance and provides for an intuitive description of transmission line resonators, the specific realization in the form of a coplanar waveguide cavity can be more accurately described in terms of its dielectric and geometric properties. This section briefly discusses a conformal, quasi-static mapping technique that leads to an analytical expression for the characteristic impedance and allows calculating the transmission spectrum from the geometry- and temperature-dependent quantities per unit length of a given coplanar waveguide.
Based on Refs. [91], [94] and [96], an expression for the characteristic impedance $Z_0 = \sqrt{L_\ell / C_\ell}$ of a superconducting coplanar waveguide resonator on a double layer substrate, accounting for dielectric losses as well as geometric and kinetic inductance effects, can be derived. A scattering matrix method [91] in turn allows for convenient calculations of the network properties of a CPW cavity like its transmission S_{21} or reflection S_{22}. Such a description is in complete analogy to the

[2] Note that Nb is a type-II superconductor.

translation and refraction matrices used in geometric optics, which expresses the equivalency of conventional optical cavities and the microwave version used here.
The effective dielectric constant of a coplanar waveguide on a finite thickness substrate is defined as the ratio of the waveguide's total capacitance per unit length C_ℓ and the partial capacitance in the absence of all dielectrics [94]

$$\varepsilon_{\text{eff}} = \frac{C_\ell}{C_{\text{air}}} \,. \tag{3.23}$$

Using the analytical expression for the partial capacitance C_{air} in Ref. [94], the total capacitance per unit length is then written as

$$C_\ell = 4\varepsilon_0 \varepsilon_{\text{eff}} \frac{K(k)}{K(k')} \,. \tag{3.24}$$

Here $K(x)$ denotes the complete elliptical integral of the first kind and the geometry-dependent quantities are given by

$$k = \frac{a}{b} \quad , \quad k' = \sqrt{1-k^2} \tag{3.25}$$

$$k_{1,2} = \frac{\sinh(\pi a/2h_{1,2})}{\sinh(\pi b/2h_{1,2})} \quad , \quad k'_{1,2} = \sqrt{1-k_{1,2}^2} \quad , \quad \beta = \frac{2\pi\nu}{c}\sqrt{\varepsilon_{\text{eff}}} \tag{3.26}$$

with the effective dielectric constant

$$\varepsilon_{\text{eff}} = 1 + \left(\frac{\varepsilon_1 - 1}{2}\right) \frac{K(k')K(k_1)}{K(k)K(k'_1)} + \left(\frac{\varepsilon_2 - \varepsilon_1}{2}\right) \frac{K(k')K(k_2)}{K(k)K(k'_2)} \tag{3.27}$$

where $\varepsilon_{1,2}$ and $h_{1,2}$ denote the relative dielectric constants and thicknesses of the two substrate materials, respectively, $2a$ the width of the center conductor and $2b$ the spacing between the two ground planes (see also Fig. 3.3). Setting $\varepsilon_1 = \varepsilon_2$, the results are readily simplified to the case of a single layer substrate.

Kinetic Inductance

The total inductance per unit length of a superconducting CPW resonator is given by the sum of the temperature independent geometric inductance L_m and the temperature dependent kinetic inductance L_k [96, 97]. A current flowing on a wire induces a magnetic flux and the energy is stored in the resulting magnetic field. Additionally, the current also translates to a kinetic energy of the electrons in the wire, which is usually masked by the conductivity of normal metals [49]. In superconductors, however, resisitivity is suppressed and thus this kinetic energy gives an additional contribution to the total inductance referred to as kinetic inductance. It holds that [94, 97]

$$L_\ell = L_m + L_k = \frac{\mu}{4}\frac{K(k')}{K(k)} + \mu \frac{\lambda_L^2(T)}{2a \cdot t} g(a,b,t) \tag{3.28}$$

where the geometric factor is given by

$$g(a,b,t) = \frac{1}{2k^2K^2(k)}\left(\ln\left(\frac{t}{8a}\right) + \frac{2b}{(2b-a)}\ln\left(\frac{b-a}{b}\right)\left(\frac{2a}{2b-a}\right)\ln\left(\frac{t}{4(2b-a)}\right)\right) \quad (3.29)$$

and μ is the permeability of the substrate material. The temperature-dependent London penetration depth $\lambda_L(T)$ can be calculated using the Casimir-Gorter approximation for the Cooper pair density [98], which yields

$$\lambda_L(T) \approx \frac{\lambda(0)}{[1-(T/T_c)^4]^{1/2}} \quad (3.30)$$

where T_c is the critical temperature of the superconductor and $\lambda(0)$ is the extrapolated London length at zero temperature, e.g. $\lambda(0)[\mathrm{Al}] \approx 50\,\mathrm{nm}$, $\lambda(0)[\mathrm{Nb}] \approx 90\,\mathrm{nm}$ [99]. The asymptotic behavior implies that the temperature dependence can be neglected for very low temperatures $T \ll T_c$, whereas $\lambda_L(T \to T_c)$ diverges as expected (above T_c, an external magnetic field can fully penetrate the bulk superconducting material). Since the temperature dependence of the Copper pair density follows a high power law and as $\lambda_L(T)$ enters quadratically into the inductance of the resonator, kinetic inductance can cause significant shifts in the resonance frequency for temperatures close to T_c.

Characteristic Impedance and ABCD-Matrices

Using (3.24) and (3.28), the total characteristic impedance of a superconducting CPW cavity can be written as

$$Z_0 = \sqrt{\frac{L_\ell}{C_\ell}} = \frac{1}{\sqrt{\varepsilon_{\mathrm{eff}}}}\left[\frac{\mu_0}{4\varepsilon_0}\frac{K(k')}{K(k)}\left(\frac{1}{2}\frac{K(k')}{K(k)} + \frac{\lambda_L^2}{a\cdot t}g(a,b,t)\right)\right]^{1/2} \quad (3.31)$$

which simplifies to

$$Z_0 = \frac{30\pi}{\sqrt{\varepsilon_{\mathrm{eff}}}}\frac{K(k')}{K(k)} \quad (3.32)$$

when kinetic and geometric inductances are neglected [94]. With (3.31), the total transmission spectrum $S_{21}(\nu)$ and thus the resonance frequencies of a capacitively coupled CPW cavity can be conventiently determined using the ABCD-matrix method from conventional microwave theory [91]. Note that this method is completely analogous to the matrix methods in geometric optics. Each circuit element of the cavity is assigned a specific 2×2 matrix that describes its transmission and reflection behavior. For a CPW resonator, the total ABCD matrix consists of two input/output coupling matrices and a transmission line matrix

$$\begin{pmatrix} A & B \\ C & D \end{pmatrix} = \begin{pmatrix} 1 & Z_{\mathrm{in}} \\ 0 & 1 \end{pmatrix}\begin{pmatrix} \cosh(\alpha+i\beta\ell) & Z_0\sinh(\alpha+i\beta\ell) \\ Y_0\sinh(\alpha+i\beta\ell) & \cosh(\alpha+i\beta\ell) \end{pmatrix}\begin{pmatrix} 1 & Z_{out} \\ 0 & 1 \end{pmatrix} \quad (3.33)$$

where $\alpha = \mathrm{Re}[\gamma]$ and $\beta = \mathrm{Im}[\gamma]$ are the attenuation and propagation coefficients as expressed in terms of the internal quality factor (3.16) and the effective dielectric constant in (3.26),

respectively. The input/output impedances are simply

$$Z_{\text{in/out}} = \frac{1}{i\omega C_{\text{in/out}}} \,. \tag{3.34}$$

Both dielectric and conductor losses are accounted for by α as it sums up all internal contributions to wave attenuation in the resonator. The transmission of a CPW resonator is expressed fully in terms of the ABCD-matrix elements and the load impedance $Z_{\text{L0}} = R_L$ at the input and output ports

$$S_{21} = \frac{2}{A + B/Z_{\text{L0}} + CZ_{\text{L0}} + D} \,. \tag{3.35}$$

Numerically maximizing S_{21} yields the resonance frequencies. Furthermore, several interesting parameters such as dielectric properties, effective lengths or quality factors of a resonator can be determined using fits of S_{21} to measured transmission spectra [92].

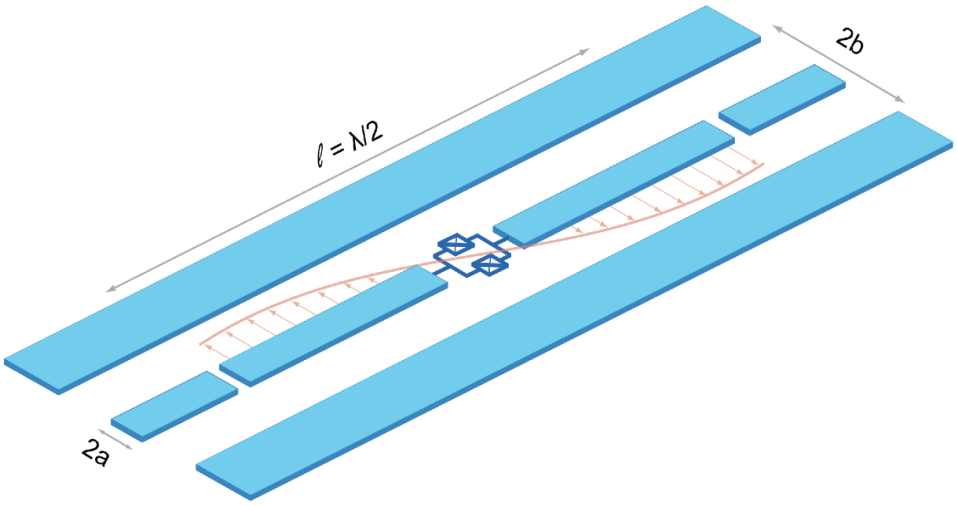

Figure 3.5: Sketch of a coplanar waveguide resonator symmetrically incorporating a SQUID-loop. The length of a transmission line section on each side of the SQUID is $\ell = \lambda/4$ so that in total one gets a $\lambda/2$ resonator.

3.2 Superconducting Tunable Resonators

The resonance frequencies of the transmission line cavities discussed so far are well-determined by their geometric properties (e.g. length, ground plane separation, coupling capacitance) as well as dielectric substrate properties (e.g. ε_{eff}, substrate thickness). By means of choosing appropriate design parameters a desired, fixed resonance frequency ν_r can be realized [92]. However, in order to realize a cavity whose frequencies can be changed *dynamically*, it has to contain some circuit element that is tunable with respect to some external degree of freedom. As shown in section 2.4, a SQUID-loop represents the prototype of such a circuit element whose impedance can be tuned using an external magnetic field. Since the complex impedance of a resonant circuit ultimately determines ν_r, a SQUID loop allows building circuits with tunable resonances. Incorporating such a parallel combination of two Josephson junctions into a transmission line resonator results in a distributed superconducting circuit whose resonance frequencies can be tuned with an external flux bias Φ. A sketch of the basic design of such a distributed circuit is illustrated in Fig. 3.5. A tunable cavity opens up a whole range of possibilities and some interesting new physics, especially when it comes to coupling it to superconducting qubits in a circuit QED architecture, where they potentially allow for fast, selective entanglement protocols [10]. The first tunable devices have recently been realized with some promising results [11, 90]. In the framework of this thesis, designs for 30 different transmission line SQUID-resonators have been developed, four of which have been successfully implemented and measured where one was strongly coupled to a transmon qubit (see section 5.2).
The discussion in sections 2.3 and 2.4 showed that the behavior of a SQUID critically depends on the magnitude of the dc current it is driven with. It was shown that if the driving current is much smaller than the critical current $I \ll I_c$, the non-linear, higher order terms in the SQUID inductance can be neglected to a good approximation. In that case, such a device is effectively

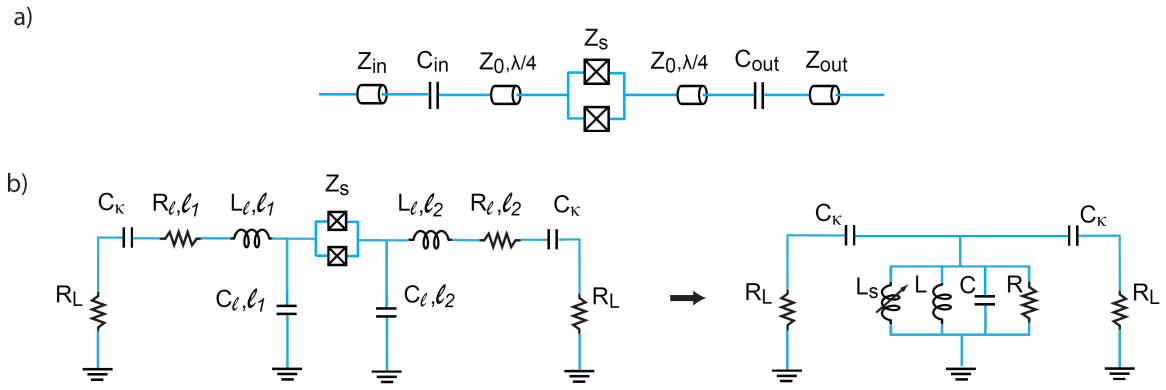

Figure 3.6: (a) Electrical sketch of the tunable resonator where $Z_{\text{in/out}}$ and $C_{\text{in/out}}$ denote the input/output impedances and capacitances, respectively, Z_0 the characteristic impedance of the transmission line sections and Z_J the SQUID impedance. (b) Mapping of the capacitively coupled resonator onto a tunable LCR oscillator.

a linear circuit element with a tunable impedance that can be modeled as a harmonic oscillator. A transmission line cavity incorporating a SQUID can then be described as an integrated system of two harmonic oscillators with a tunable resonance frequency $\omega_r(\Phi)$. On the other hand, the non-linearity can reach significant levels for larger driving currents so that the corresponding SQUID-resonator will essentially become an anharmonic oscillator. It is important to note that the driving current does not necessarily have to be on the order of the critical current for the non-linearity to become important, i.e. a given SQUID can be non-linear even for $I \ll I_c$. As shown below, the degree of this non-linearity can be directly related to the number of photons inside the cavity, which corresponds to an ac driving current at the position of the SQUID. This qualitatively different behavior depending on the magnitude of the driving current has to be accounted for in an accurate description. The total SQUID-cavity system of Fig. 3.5 will be discussed in several different approaches. Starting with a mapped LCR model and a scattering matrix formulation as in section 3.1.1, we will then proceed to give a full second quantization treatment of the system including perturbation theory [89]. The section is rounded off by a discussion of the design and operating constraints for implementing a tunable cavity.

3.2.1 Electrical Circuit and Scattering Matrix Model

In a classical electrical approach, the SQUID-cavity system depicted in Figs. 3.5 and 3.6 can be fully described using the methods developed for regular transmission line resonators. In the implementation of this thesis, the SQUID is positioned at the center of the resonator, attached on both sides to a $\ell = \lambda/4$ coplanar waveguide capacitively coupled to the input/output lines, see Fig. 3.6a. In total this gives a $\lambda/2$ coplanar waveguide cavity with a flux-tunable resonance frequency. Recalling the SQUID impedance Eq. (2.39)

$$Z_s(\omega, \Phi) = \frac{i\omega L_s(\Phi) R_s}{R_s + i\omega L_s(\Phi) - \omega^2 L_s(\Phi) C_s R_s}, \tag{3.36}$$

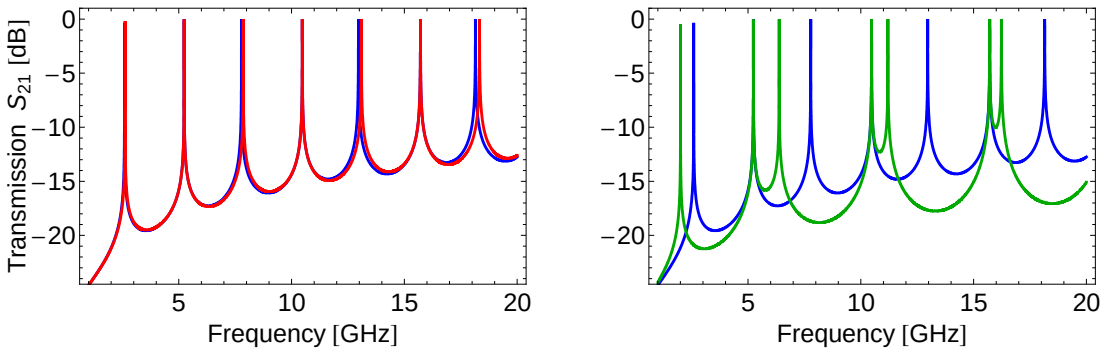

Figure 3.7: (a) Comparison of calculated transmission spectra for a transmission line resonator with (red) and without (blue) SQUID-loop incorporated. (b) Transmission spectra of a SQUID-resonator for two different external fluxes $\Phi_{\text{ext}}^{(1)} = n \cdot \Phi_0$ (blue) and $\Phi_{\text{ext}}^{(2)} = (n + 1/2)\Phi_0$ (red). For these simulations, the typical parameters $\ell = 22000\,\mu$m, $I_{c1} = 1.78\,\mu$A, $I_{c2} = 1.80\,\mu$A and $C_{\text{in/out}} = 4.7\,$fF of cavity design 'I1' have been used. Note that insertion losses $\alpha = \text{Re}[\gamma]$, $\gamma = \alpha + i\beta$ have been neglected in these calculations

we can assign each part of the circuit a specific 2×2 matrix. The transmission coefficient S_{21} is then found in a straight-forward way. The total ABCD matrix of the resonator reads

$$\begin{aligned}\begin{pmatrix} A & B \\ C & D \end{pmatrix} &= \begin{pmatrix} 1 & Z_c \\ 0 & 1 \end{pmatrix} \begin{pmatrix} \cos\beta l & jZ_0 \sin\beta l \\ jY_0 \sin\beta l & \cos\beta l \end{pmatrix} \begin{pmatrix} 1 & Z_s \\ 0 & 1 \end{pmatrix} \\ &\times \begin{pmatrix} \cos\beta l & jZ_0 \sin\beta l \\ jY_0 \sin\beta l & \cos\beta l \end{pmatrix} \begin{pmatrix} 1 & Z_c \\ 0 & 1 \end{pmatrix} \end{aligned} \tag{3.37}$$

where we have assumed symmetric coupling. Neglecting resistive losses, the SQUID impedance in the linear limit is written as

$$Z_s = i \left(\frac{2\pi}{\omega \Phi_0} \left[(I_{c1} - I_{c2})^2 + 4 I_{c1} I_{c2} \cos^2 \left(\frac{\pi \Phi}{\Phi_0} \right) \right]^{1/2} - \omega C_s \right)^{-1} . \tag{3.38}$$

Following section 3.1.4, the transmission of the resonator is then given by

$$S_{21} = \frac{2}{A + B/Z_{L0} + CZ_{L0} + D} . \tag{3.39}$$

Numerically maximizing $S_{21}(\omega)$ yields the resonance frequencies of the circuit. Since the resonator now incorporates a flux-dependent inductance, the resulting transmission spectrum can be varied by applying a local external magnetic field. Fig. 3.7a shows a comparison of calculated transmission spectra for a $\lambda/2$ resonator without SQUID (blue) and one with a SQUID-loop incorporated at the center (red; zero flux bias). As can be seen, the resonances are slightly shifted for zero flux bias, simply by the additional impedance of the SQUID-loop. To a good approximation, however, the two cases with and without SQUID are identical at $\Phi = 0$. Furthermore, a comparison of two transmission spectra for different external fluxes $\Phi_{(1)} = n \cdot \Phi_0$ and $\Phi_{(2)} = (n + 1/2)\Phi_0$ applied to a SQUID resonator are given in Fig. 3.7b. As expected, every even mode is invariant under changes of Φ, which is a consequence of the symmetry of the

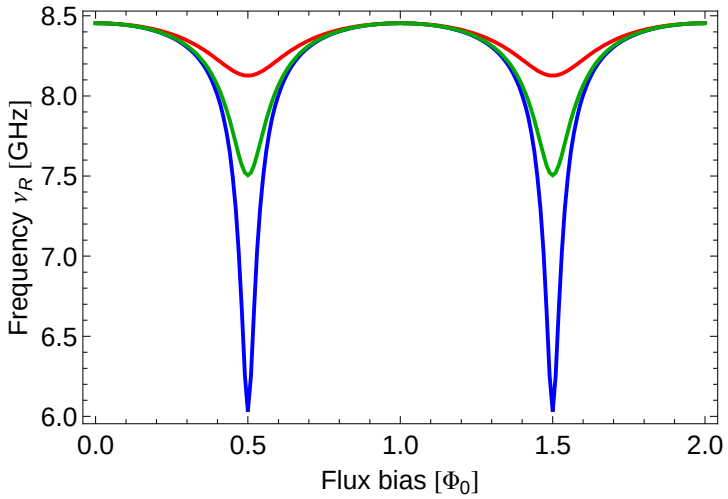

Figure 3.8: Resonance frequencies of a SQUID-cavity as functions of flux bias for different degrees of junction asymmetry: $d = 5\%$ (blue), $d = 20\%$ (green) and $d = 50\%$ (red). Here, we have used the parameters $\ell = 7600\,\mu$m and $C_{\text{in/out}} = 7.8\,$fF, corresponding to cavity design 'H1'.

resonator: Since the SQUID is positioned at the center of the resonator with equal $\lambda/4$ transmission line sections on both sides, the current has a node $I = 0$ and the voltage an anti-node $V = V_{\text{max}}$ at the SQUID's position for every other mode $n = 2i$, $i \in \mathbb{N}$. Thus, for instance, in the second mode the electromagnetic field does not 'see' the SQUID since the current vanishes at its position and therefore the resonance frequency does not change under variations of Φ. This 'deactivation' of certain modes also naturally follows from a field-theoretical treatment and will be further discussed in section 3.2.2. In addition, plots of the first mode resonance frequency, obtained from numerically maximizing S_{21}, are depicted in Fig. 3.8 as a function of flux bias for three different critical current combinations at fixed resonator length. The resonance frequency can be tuned by several GHz over a period in Φ_0. The critical current asymmetry $d = (I_{c1} - I_{c2})/(I_{c1} + I_{c2})$ determines the tuning range and the total range decreases with increasing d.

In analogy to the case of a regular CPW resonator, the tunable version can also be described in terms of a mapped LCR oscillator model. This provides for an intuitive picture and shows that the SQUID-cavity system effectively realizes a tunable harmonic oscillator. In the linear limit and assuming a negligible SQUID capacitance C_s, the tunable TL resonator can be readily mapped onto an LCR oscillator, see Fig. 3.6b. Compared to the regular mapped TL resonator, the presence of the SQUID results in an additional parallel inductance that can be tuned with an external flux. The total impedance reads

$$Z_{\text{LCR}}(\Phi) = \left[\frac{1}{R} + i\left(\omega C - \frac{1}{\omega}\left(\frac{L_s + L}{L_s L}\right)\right)\right]^{-1} \tag{3.40}$$

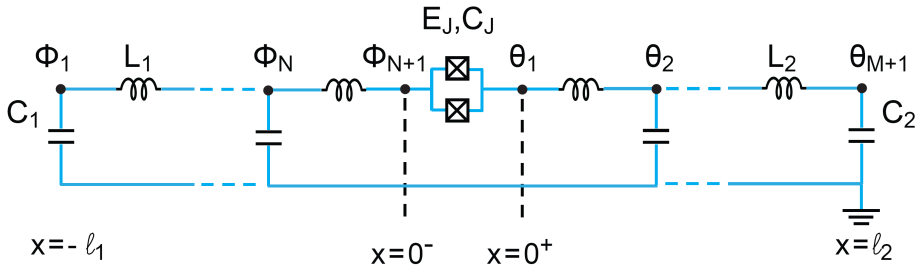

Figure 3.9: Lumped element circuit representation of a transmission line resonator incorporating a parallel pair of two Josephson junctions. This model can be used for an effective quantization of the distributed circuit, see detailed discussion in the text.

with the flux-tunable resonance frequencies

$$\omega_n(\Phi) = \frac{n}{\sqrt{C\left(\frac{L_s L}{L_s+L}\right)}} \approx \omega_r \sqrt{1+\frac{L}{L_s}} \tag{3.41}$$

where $L_s = L_s(\Phi)$ is the SQUID inductance and ω_r the resonance frequency of the equivalent resonator without SQUID.

3.2.2 Circuit Quantization

Up until now, the cavity-SQUID system was discussed in terms of a classical approach. The two systems were described in a classical electrical picture with the quantum-mechanical Josephson effect manifesting itself only via the flux-dependent inductance. The next step now consists of a full circuit quantization in which the tunable resonator is quantized as a whole following the procedure of section 2.1. Incorporating a Josephson junction-based element such as a SQUID into a TL resonator naturally introduces a Kerr-type non-linearity to the system and thus renders the energy spectrum of the cavity non-linear. Following the discussion in sections 2.3 and 2.4.2, the degree of this non-linearity is determined by the magnitude of the current driving the SQUID. In the non-linear regime, the tunable transmission line resonator represents an anharmonic oscillator rather than a standard harmonic oscillator. This effect was not addressed by the purely electrical approach of section 3.2.1, where all non-linear, higher order terms of the SQUID inductance (2.42) have been neglected.
As shown in [10] and [89], a quantization of the full circuit consisting of transmission line and SQUID can treat the non-linear effects perturbatively. This treatment explicitly shows that the SQUID's non-linearity effectively causes frequency shifts proportional to the number of photons inside the resonator, i.e. depending on the corresponding current at the position of the SQUID. The quantization procedure of the total SQUID-resonator system given here closely follows Ref. [89].
Following section 2.1, the two conjugate variables describing an electrical circuit are flux $\Phi(t)$ and charge $q(t)$. Since the flux is directly related to the superconducting phase of the SQUID

via $\phi = (2\pi/\Phi_0)\Phi \text{Mod}(2\pi)$, the flux representation is used here for convenience. The system is modeled as a series lumped element circuit as depicted in Fig. 3.9. The circuit is split into three parts: (1) a transmission line of length ℓ_1 and capacitance and inductance per unit length C_1^0 and L_1^0 on the l.h.s of the SQUID, (2) a parallel set of Josephson junctions of infinitesimal length and Josephson energy E_J and capacitance C_J and (3) a transmission line on the r.h.s of the SQUID with length ℓ_2 and capacitance and inductance per unit length C_2^0 and L_2^0. In the flux representation, each lumped element section i of the circuit is assigned a certain node flux, i.e. $\Phi_i, i \in \mathbb{N}$ on the l.h.s of the SQUID and $\theta_i, i \in \mathbb{N}$ on the r.h.s.[3]. Furthermore, each section then has a capacitance $C_{1,2}$ and inductance $L_{1,2}$ which are related to the infinitesimal quantities per unit length through $C_{1,2} = C_{1,2}^0 \Delta x$ and $L_{1,2} = L_{1,2}^0 \Delta x$. The SQUID's position is set as the origin. Following section 2.1, the Lagrangian of the total circuit Fig. 3.9 then reads

$$\begin{aligned}
\mathcal{L} &= \mathcal{L}_{\text{lhs}} + \mathcal{L}_{\text{s}} + \mathcal{L}_{\text{rhs}} \\
&= \sum_{i=1}^{N} \frac{1}{2}\left[C_1 \dot{\Phi}_i^2 - \frac{(\Phi_{i+1} - \Phi_i)^2}{L_1}\right] \\
&+ \frac{C_J}{2}(\dot{\theta}_1 - \dot{\Phi}_{N+1})^2 - \frac{E_J}{2\phi_0^2}(\theta_1 - \Phi_{N+1})^2 \\
&+ \sum_{i=1}^{M} \frac{1}{2}\left[C_2 \dot{\theta}_i^2 - \frac{(\theta_{i+1} - \theta_i)^2}{L_2}\right]
\end{aligned} \tag{3.42}$$

where we have used the SQUID Lagrangian of section 2.4 and introduced the reduced flux quantum $\phi_0 = 2\pi/\Phi_0$. Note that here the harmonic approximation for the Josephson energy has already been made, i.e. $\mathcal{L}_s$ only contains the first non-vanishing term of the Josephson cosine potential (see section 2.4). All higher order terms are neglected. Later on, we will recover the non-linearity from the harmonized Hamiltonian by means of treating the quartic order term of the Josephson potential perturbatively. Furthermore, note that we assume a flux-independent Josephson energy in (3.42), i.e. the SQUID is first treated as a single junction with Josephson energy E_J throughout the quantization procedure. The flux-dependence of the SQUID will then be recovered later on by making the simple transition $E_J \to E_J(\Phi)$.

Wave Equation

The Euler Lagrange equations $(d/dt)(\partial\mathcal{L}/\partial\dot{q}) - (\partial\mathcal{L}/\partial q_i) = 0$ resulting from the Lagrangian density (3.42) are wave equations for the generalized position coordinate on both sides of the SQUID ($x = 0$), i.e. for the node flux Φ_i ($x < 0$) and θ_i ($x > 0$). Making the transition to a continuous description in (3.42)

$$\Delta x \to 0 \quad , \quad \sum_{i=1}^{N} \to \int_{-\ell_1}^{0} \quad , \quad \sum_{i=1}^{M} \to \int_{0}^{\ell_2} \quad , \quad (\Phi_i, \theta_i) \to (\Phi(x), \theta(x)) \tag{3.43}$$

[3]Note that the total flux field is, however, continuous despite this artificial separation since the SQUID's longitudinal extension is neglected.

and using the connection between lumped element and TL quantities per unit length $C_{1,2} = C^0_{1,2}\Delta x$ and $L_{1,2} = L^0_{1,2}\Delta x$, the Lagrangian is rewritten as

$$\begin{aligned} L &= \int_{-\ell_1}^{0} \frac{1}{2}\left[C(x)\dot{\Phi}^2 - \frac{1}{L(x)}\left(\frac{\partial\Phi}{\partial x}\right)^2\right] + \int_0^{\ell_2}\left[C(x)\dot{\theta}^2 - \frac{1}{L(x)}\left(\frac{\partial\theta}{\partial x}\right)^2\right] \\ &+ \frac{C_J}{2}\left(\dot{\theta}(0) - \dot{\Phi}(0)\right)^2 - \frac{1}{2L_J}\left(\theta(0) - \Phi(0)\right)^2 \end{aligned} \tag{3.44}$$

where we have defined

$$C(x) = \begin{cases} C_1^0 & x < 0 \\ C_2^0 & x > 0 \end{cases} \quad , \quad L(x) = \begin{cases} L_1^0 & x < 0 \\ L_2^0 & x > 0 \end{cases} \quad . \tag{3.45}$$

The wave equations for the flux field are then simply found as the Euler-Lagrange equations corresponding to (3.44):

$$\ddot{\Phi}(x,t) - \frac{1}{L(x)C(x)}\frac{\partial^2\Phi(x,t)}{\partial x^2} = 0 \quad , \quad \ddot{\theta}(x,t) - \frac{1}{L(x)C(x)}\frac{\partial^2\theta(x,t)}{\partial x^2} = 0 \tag{3.46}$$

with the standard plane wave solutions of the form

$$\Phi(x,t) = \sum_k e^{-i\omega_k t}\left(A_k e^{-ikx} + B_k e^{ikx}\right) \quad , \quad \theta(x,t) = \sum_q e^{-i\omega_q t}\left(C_q e^{-iqx} + D_q e^{iqx}\right) \tag{3.47}$$

where k and q are the wave numbers on the l.h.s and r.h.s of the SQUID, respectively. The corresponding frequencies are given in the usual form

$$\omega_k = \frac{k}{\sqrt{L_1^0 C_1^0}} \quad , \quad \omega_q = \frac{q}{\sqrt{L_2^0 C_2^0}}\,. \tag{3.48}$$

In the end, we are interested in continuous modes of the flux field rather than in the two separate wave functions (3.47). Such an expression can be derived by considering three fundamental constraints on the field: (i) the continuity condition at the SQUID position $x = 0$, (ii) the boundary condition that no current should flow outside the resonator at both ends $I_1(x = -\ell_1) = I_2(x = \ell_2) = 0$ and (iii) the conservation of current at the origin $I_1(x = 0) = I_2(x = 0)$. Consecutively applying these constraints leads to a transcendental equation for the field whose solutions form a complete, infinite set of orthogonal eigenfunctions [10, 89]. The detailed calculations that lead to this equation are presented in appendix A, where it is also shown that the eigenmodes of the total system $\Psi(x,t)$ can be written in a separation form $\Psi(x,t) = \sum_k \Psi_k(t)\chi_k(x)$, where k denotes the wave number for the complete resonator.

Effective Hamiltonian

With the continuous eigenmodes $\Psi(x,t)$ of the total circuit (see appendix A), the continuous Lagrangian (3.44) can be conveniently written as

$$L = \frac{1}{2}\int_{-\ell_1}^{\ell_2}\left[C(x)\dot{\Psi}(x,t)^2 - \frac{1}{L(x)}\left(\frac{\partial\Psi(x,t)}{\partial x}\right)^2\right]dx - \frac{1}{2L_j}(\Psi(0^+,t)-\Psi(0^-,t))^2\,. \quad (3.49)$$

The decomposition of the field into a spatial $\chi_k(x)$ and a time-dependent part $\Psi_k(t)$ in turn allows rewriting this Lagrangian as a sum of harmonic oscillators of frequency ω_k (see appendix A)

$$L = \sum_k \frac{C_{\text{cav}}}{2}\dot{\Psi}_k(x,t) - \frac{C_{\text{cav}}\omega_k^2}{2}\Psi_k^2(t) \quad (3.50)$$

where the total capacitance of the cavity $C_{\text{cav}} = \int_{-\ell_1}^{\ell_2} C(x)dx$ was introduced. Here, the flux-dependent resonance frequency is given by [10]

$$\omega_0(\Phi) = \frac{\omega_r}{1+\frac{L_s(\Phi)}{L}} \quad (3.51)$$

where ω_r denotes the fundamental resonance frequency of the equivalent cavity without SQUID. The fact that the Lagrangian can be written as a sum of harmonic functions results from the linear approximation of the Josephson potential that was made in the very beginning in (3.42). As shown below, the anharmonicity can be recovered by means of treating higher order terms of the potential perturbatively.
Using the fact that charge is the conjugate variable to the flux Ψ_k

$$q_k = \frac{\partial L}{\partial\dot{\Psi}_k}\,, \quad (3.52)$$

a Legendre transformation $H = \Psi_k q_k - L$ of the Lagrangian leads to the classical Hamiltonian

$$H_0 = \sum_k \frac{q_k^2}{2C_{\text{cav}}} + \frac{1}{2}C_{\text{cav}}\omega_k^2\Psi_k^2\,. \quad (3.53)$$

As usual, the last step now consists of a second quantization where we introduce the ladder operators through

$$\Psi_k = \sqrt{\frac{\hbar}{2C_{\text{cav}}\omega_k}}\left(a_k^\dagger + a_k\right) \quad , \quad q_k = \sqrt{\frac{\hbar C_{\text{cav}}\omega_k}{2}}\left(a_k^\dagger - a_k\right)\,. \quad (3.54)$$

with the final Hamiltonian

$$H_0 = \sum_k \hbar\omega_k\left(a_k^\dagger a_k + \frac{1}{2}\right)\,. \quad (3.55)$$

This shows explicitly that in the linear SQUID regime $I \ll I_c$, the tunable cavity can be treated as a harmonic oscillator just like the regular cavities of section 3.1, the only difference being

the flux-dependence of the resonance frequencies ω_k. If, however, higher order terms of the Josephson potential can not be neglected, the harmonic oscillator description is no longer valid and the perturbed Hamiltonian acquires anharmonic terms.

Deactivated Modes

Now before turning to a discussion of the non-linear effects and the perturbative treatment of higher order terms, the phenomenon of 'mode deactivation' will be briefly reviewed in a field-theoretical context. The purely electrical treatment of the $\lambda/2$ SQUID-resonator system in section 3.2.1 already showed that for the symmetric case of a SQUID at the center position, every even mode stays completely invariant under the presence of the SQUID. In an electrical context, this simply results from the fact that the current has nodes at the position of the SQUID for every even mode so that the field does not 'see' the SQUID. In general, this deactivation of certain modes occurs whenever the current vanishes at the SQUID's position. Field-theoretically, this automatically follows from the continuity condition, i.e. the diffraction law $\omega_k \equiv \omega_q$, $kv_1 = qv_2$ with v_i denoting the wave velocity, and the conservation of current $I_1(x=0) = I_2(x=0)$ (see also appendix A). Using the eigenmode decomposition $\Psi(x,t) = \sum_k \Psi_k(t)\chi_k(x)$, the current is given by

$$I(x,t) = -\sum_k \frac{\Psi_k(t)}{L_0}\frac{\partial \chi_k}{\partial x} \tag{3.56}$$

which vanishes for wave numbers $k = m\pi/\ell$ and $q = n\pi/\ell$, $\forall n, m \in \mathbb{N}$ in a symmetric resonator $\ell_1 = \ell_2 = \ell$. Using these wave numbers together with the constraint of current conservation, the field amplitudes on the r.h.s and l.h.s of the SQUID are conditioned by (see appendix A or [89])

$$D_k = A_k(-1)^{m-n}\,. \tag{3.57}$$

This shows explicitly that purely even modes only occur when the l.h.s and r.h.s are identical. These modes are essentially deactivated as they ignore the presence of the SQUID. Thus, depending on the frequency that is used to probe the system, we will either see a standard resonator (deactivated modes) or a tunable one (activated modes).

3.2.3 The Non-Linear Tunable Cavity - A Solid-State Photonic Qubit

The higher order terms that have been neglected in the initial Lagrangian (3.42) can be treated as a perturbation to the harmonic Hamiltonian (A.26) which allows us to recover some of the non-linear effects that are caused by the SQUID. Taking into account the term quartic in phase difference and restricting the Hilbert space to a single mode k , the anharmonic Hamiltonian can be written as

$$H = H_0 + H_A = \hbar\omega_k\left(a_k^\dagger a_k \frac{1}{2}\right) - \frac{E_j}{4!}\frac{1}{\phi_0^4}(\theta_1 - \phi_N)^4 \tag{3.58}$$

where the flux-dependence of the Josephson energy is given by (see section 2.4)

$$E_j = E_{j\Sigma} \cos\left(\frac{\pi\Phi_{\text{ext}}}{\Phi_0}\right) \sqrt{1 + d^2 \tan^2\left(\frac{\pi\Phi_{\text{ext}}}{\Phi_0}\right)} \tag{3.59}$$

with the asymmetry parameter

$$d = \frac{E_{j2} - E_{j1}}{E_{j2} + E_{j1}}\,. \tag{3.60}$$

Using the ladder operators defined by (A.25), the phase difference across the SQUID in (3.58) can be expressed in the continuous limit as [89]

$$\theta_1 - \phi_N = \sum_k \Delta_k \left(a_k^\dagger + a_k\right) \tag{3.61}$$

with Δ_k denoting the phase gap at the junctions which can be rewritten as

$$\Delta_k = -2A_k \sin(k\ell/2) \sqrt{\frac{\hbar}{2C\omega_k}} \cot(k\ell/2) \tag{3.62}$$

where a center-positioned SQUID was assumed. Here, the field amplitude A_k is given by (see appendix A)

$$A_k = \sqrt{\frac{C}{C_\ell}} \left[\frac{\ell}{2} + \frac{\sin(k\ell)}{2k}\right]^{-1/2} \tag{3.63}$$

so that the phase gap in the case of symmetric alignment simplifies to

$$\Delta_k = -\sqrt{\frac{2\hbar}{C_\ell \omega_k}} \left[\frac{\ell}{2} + \frac{\sin(k\ell)}{2k}\right]^{-1/2} \cos(k\ell/2)\,. \tag{3.64}$$

Now using (3.64) in the nonlinear Hamiltonian (3.58), neglecting any fast oscillating terms of $a_k^\dagger$ and a_k in the rotating-wave approximation, the total Hamiltonian for mode k is obtained as

$$H = \hbar\left(\omega_k - \Delta\omega_k a_k^\dagger a_k\right) a_k^\dagger a_k \tag{3.65}$$

where the frequency shift

$$\Delta\omega_k \equiv \Delta\omega_k(\Phi_{\text{ext}}) = \frac{E_j(\Phi_{\text{ext}})}{4\hbar} \left(\frac{2\pi}{\Phi_0}\Delta_k\right)^4\,. \tag{3.66}$$

has been introduced. Note that in this approximation the non-linearity of the Josephson elements in the resonator ultimately reduces to a flux- and photon number-dependent frequency shift that generates the anharmonicity of the energy spectrum. The corresponding eigenequation can be easily solved algebraically with the photon number eigenstates $|n, k\rangle$ which yields the energies

$$E_{n,k} = \hbar n_k(\omega_k - \Delta\omega_k(\Phi_{\text{ext}}) n_k)\,. \tag{3.67}$$

The non-linearity becomes most obvious from the flux-dependent spacing of the energy levels of the single-mode radiation field

$$\Delta E_k = E_{n+1,k} - E_{n,k} = \hbar\omega_k - \hbar\Delta\omega_k(\Phi_{\text{ext}})(2n+1)\,. \tag{3.68}$$

This perturbative procedure is readily expanded to account for an infinite number of modes, which gives the general Hamiltonian of the radiation field of the tunable cavity [89]

$$H = \hbar\sum_{k,j}\left(\omega_k - 2\Delta\omega_{kj}a_j^\dagger a_j + \Delta\omega_{kk}a_k^\dagger a_k - \Delta\omega_{kj}\right)\left(a_k^\dagger a_k + \frac{1}{2}\right) \tag{3.69}$$

with the generalized frequency shift

$$\Delta\omega_{kj}(\Phi_{\text{ext}}) = \frac{E_j(\Phi_{\text{ext}})}{4\hbar}\left(\frac{2\pi}{\Phi_0}\right)^4(\Delta_k\Delta_j)^2\,. \tag{3.70}$$

The non-linear Hamiltonian of the SQUID-cavity contains some rich physics that are worthwhile investigating. Owning to the non-linearity of the junctions, the bare frequency ω_k of each isolated mode acquires a photon-number dependent term that looks much like a Stark shift and is independent of all other modes and only proportional to the internal photon number in each mode. Indeed, the physics is the same and the modes seem to be Stark-shifted by their own photon population. Moreover, the different modes are dispersively coupled to each other so that a given mode k also acquires a Stark shift proportional to the photon number in the other modes. This interesting phenomenon opens up a number of fascinating possibilities. If the shift per photon $\Delta\omega_{kk}$ can be made larger than the linewidth of the cavity, we should be able to observe several distinct peaks corresponding to different photons. In this way, one could resolve individual photon number states even without the presence of a qubit. Provided the mode spacing is sufficiently large, the photon number of a single-mode radiation field in the cavity can then be inferred from a simple transmission measurement, realizing a resonator that monitors its own photon population. In principle, the shift per photon $\Delta\omega_{kk}$ can be made sufficiently large by fabricating junctions with large enough Josephson energies and using a high Q cavity with narrow resonances can also help to resolve the individual photon states inside the resonator. Moreover, in case of strong coupling between the different modes, it would also be possible to monitor the photon number in a mode by measuring the transmission of an adjacent mode, thus realizing a quantum-non demolition measurement very much in the same way as the qubit readout in traditional circuit QED systems (see chapter 4). Unfortunately, time was too scarce to pursue these ideas much further within this thesis, although some promising preliminary results have been obtained.

As is also discussed in Ref. [89], the non-linearity of the resonator might in fact also make it possible to use the resonator itself as a qubit, i.e. as a solid-state based photonic qubit. If the degree of anharmonicity suffices, one could, for instance, use the photon number states $|n=0\rangle$ and $|n=1\rangle$ as logic states for quantum computation. The energy relaxation time of such a solid state photonic qubit is given by the cavity decay time $T_\kappa = 1/\kappa$ which is determined by the quality factor of the resonator. A high Q yields long decay times and the photons can

then in principle be stored for a sufficiently long time to allow for computational operations. The coupling to a low Q cavity was proposed as a way to readout the state of the photonic qubit [89]. An elementary calculation [89] shows that the readout mechanism works in the same way as the dispersive readout scheme in conventional circuit QED (see chapter 4). The non-linear, high Q cavity induces a photon-number dependent shift in the resonance frequency of the readout cavity which can in turn be inferred from a transmission measurement. Another natural possibility results from the Stark shifts and the mode-mode coupling discussed above, where the qubit state could be inferred from a transmission measurement of an adjacent mode.

3.2.4 Operating Constraints

Designing and fabricating a TL cavity that incorporates a superconducting quantum interference device represents a formidable challenge since a fairly large number of inter-dependent design parameters have to be chosen in a consistent way. This section discusses the most important design considerations and the constraints that have to be accounted for to effectively operate a superconducting tunable cavity.

Critical Currents and Junction Sizes

The discussion of the RCSJ-model in chapter 2 has shown that the behavior of SQUIDs and Josephson junctions is governed by Langevin-type pendulum equations (2.24). In the linear regime, a SQUID represents a damped, harmonic oscillator with quality factor Q, damping κ and plasma frequency

$$\omega_\mathrm{p} = \sqrt{\frac{2\pi I_c}{\Phi_0 C_s}}\,. \tag{3.71}$$

The oscillation can be thought of as the movement of a 'phase-particle' in the SQUID Josephson potential. Now sending microwave signals at frequency ω through a TL cavity that incorporates a SQUID does not only excite the resonances ω_r of the cavity but also the resonances of the superconducting loop itself. Hence ω_r has to be much smaller than ω_p in order to avoid resonant excitation of the SQUID while driving the cavity. According to (2.35) and (3.71), this in turn imposes the constraint

$$I_c \gg \frac{\omega_\mathrm{r}^2 \Phi_0 C_s}{2\pi} \tag{3.72}$$

on the choice of critical currents. For a typical capacitance value of $C_s = 2$ pF, this yields the lower limit $I_c \geq 25$ nA for a 6 GHz resonator. Furthermore, this requirement also gives an upper limit for the operating temperature of the cavity

$$\hbar\omega_\mathrm{p} \gg \hbar\omega_\mathrm{R} \gg k_\mathrm{b} T\,. \tag{3.73}$$

Thus for a 6 GHz resonator one has to operate at temperatures $T \ll 285$ mK. In an actual experiment, the non-linearity of the SQUID should be effectively suppressed to realize a cavity that is as close as possible to an ideal harmonic oscillator. The discussions in chapter 2 have

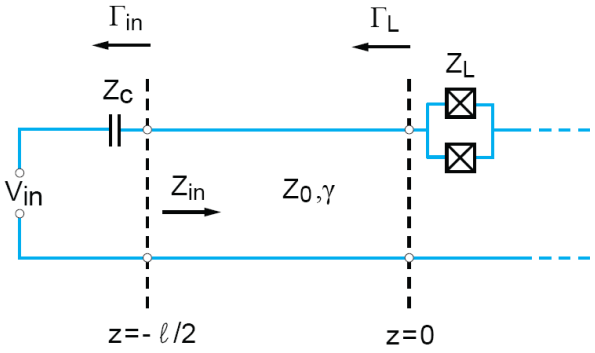

Figure 3.10: Schematic circuit diagram of a capacitively coupled transmission line incorporating a SQUID loop.

also shown that the degree of non-linearity is determined by the current through the SQUID. This in turn imposes a constraint on the input power that the resonator can be driven at.

Input and Drive Power

Operating the SQUID-cavity system in the linear regime requires that the current through the SQUID is below the critical current of the junctions $I \ll I_c$. This constraint can be directly expressed in terms of the input power applied to the resonator.
A classical, analytical expression for the current at the position of the SQUID at a given input power can be derived using methods borrowed from conventional microwave theory [91]. Consider the transmission line model depicted in Fig. 3.10. The applied input or gate voltage V_g couples into the resonator through the input capacitance Z_C at position $z = -\ell$ [4]. The SQUID at $z = 0$ is effectively regarded as a load impedance Z_L with reflection coefficient Γ_L. The voltage wave at an arbitrary position z along the transmission line can be written as [91]

$$V(z) = V_0^+ e^{-\gamma z} + V_0^- e^{+\gamma z} \tag{3.74}$$

where $\gamma = \alpha + i\beta$ is the propagation constant introduced in section 3.1.1 and V_0^+ and V_0^- denote the incident and reflected wave amplitudes, respectively. Thus using the reflection coefficient Γ_L of the load (i.e. the SQUID), the voltage reads

$$V(z) = V_0^+ \left(e^{-\gamma z} + \Gamma_L e^{+\gamma z}\right) \tag{3.75}$$

with the corresponding current

$$I(z) = \frac{V_0^+}{Z_0} \left(e^{-\gamma z} - \Gamma_L e^{+\gamma z}\right) . \tag{3.76}$$

[4] For a more convenient derivation and less cumbersome notation, the SQUID's position was chosen at the origin $z_s = 0$ with the total resonator having a length of $l_R = 2\ell$. In the end we will make the transition $z_s \to \ell/2$ and $l_R \to \ell$.

The effective input impedance Z_{in} looking into the resonator at a distance ℓ from the input is given by [91]

$$Z_{in} = Z_0 \frac{Z_L + Z_0 \tanh \gamma\ell}{Z_0 + Z_L \tanh \gamma\ell} = \frac{1 + \Gamma_L e^{-2\gamma\ell}}{1 - \Gamma_L e^{-2\gamma\ell}} Z_0 \,. \tag{3.77}$$

Now simply applying Ohm's law to the circuit in Fig. 3.10 gives (voltage divider rule)

$$V(z = -\ell) = V_0^+ \left(e^{\gamma\ell} + \Gamma_L e^{-\gamma\ell}\right) = V_{in} \frac{Z_{in}}{Z_{in} + Z_c} \tag{3.78}$$

from which the amplitude V_0^+ can be expressed

$$V_0^+ = V_{in} \frac{Z_{in}}{Z_{in} + Z_c} \frac{1}{e^{\gamma\ell} + \Gamma_L e^{-\gamma\ell}} \,. \tag{3.79}$$

Here Z_c denotes the input impedance, i.e. the capacitance. Now plugging in (3.77) yields

$$V_0^+ = V_{in} \frac{Z_0}{Z_0 + Z_c} \frac{e^{-\gamma\ell}}{1 - \Gamma_c \Gamma_L e^{-2\gamma\ell}} \tag{3.80}$$

where the reflection coefficient of the input capacitance $\Gamma_c = (Z_c - Z_0)/(Z_c + Z_0)$ has been introduced. Note that this coefficient is just the scattering matrix parameter S_{22} of the input capacitance, see section 3.1.3. Furthermore, from the definition of the parameter S_{21} (3.35) it follows that

$$2S_{21} = \frac{Z_0}{Z_0 + Z_c} \tag{3.81}$$

so that Eq. (3.80) is expressed as

$$V_0^+ = 2V_{in} \frac{S_{21} e^{-\gamma\ell}}{1 - S_{22}\Gamma_L e^{-2\gamma\ell}} \,. \tag{3.82}$$

Hence using (3.76), the current at position z is written as

$$I(z) = \frac{2V_{in}}{Z_0} \left(e^{-\gamma z} - \Gamma_L e^{\gamma z}\right) \frac{S_{21} e^{-\gamma\ell}}{1 - S_{22}\Gamma_L e^{-2\gamma\ell}} \,. \tag{3.83}$$

The time-averaged input power is given by $P_{in} = \frac{1}{2} V_{in}^2 / Z_0$. Using this expression, reseting the origin at the input of the resonator and making the transition $\ell \to \ell/2$ to the right resonator length finally yields

$$I(z) = \sqrt{\frac{8P_{in}}{Z_0}} \left(e^{\gamma z} - \Gamma_L e^{-\gamma z}\right) \frac{S_{21} e^{-\gamma\ell/2}}{1 - S_{22}\Gamma_L e^{-\gamma\ell}} \,. \tag{3.84}$$

Neglecting losses $\gamma \approx i\beta$ where $\beta\ell = \pi/2$ for a $\lambda/2$ cavity on resonance and assuming $\Gamma_L = 1$, which holds for large Josephson energies, the current at the SQUID position at $z = \ell/2$ is plotted as a function of input power for different coupling capacitances in Fig. 3.11. For very low driving currents, the SQUID can be assumed to be in the linear regime and the total cavity system is described as a simple harmonic oscillator with a tunable resonance frequency (see section 3.2.2). Using the typical values $C_\kappa = 5$ fF, $Z_0 = 50\,\Omega$ and $I_c = 500$ nA at a resonance frequency of

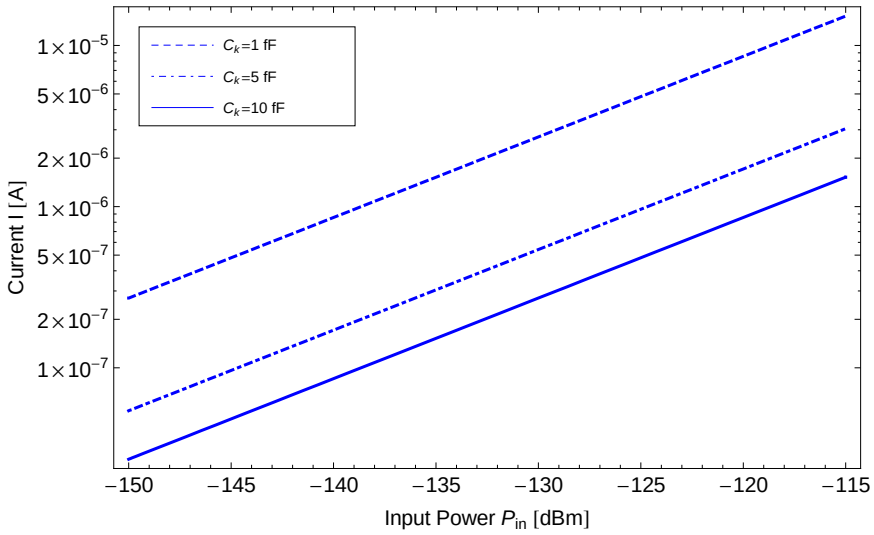

Figure 3.11: Logarithmic plot of the current I at the position of the SQUID $z = \ell/2$ as a function of input power P_{in} at the resonator for different coupling capacitances.

$\nu_R = 6.65$ GHz, this leads to the constraint

$$P_{in} \leq -130\,\text{dBm} \tag{3.85}$$

for the power applied to the resonator input. Exceeding the critical current leads to non-linear effects. Quantum-mechanically, this power constraint directly translates to a maximum photon population of the resonator. Using the current definition (3.56) as well as the flux field expressions from appendix A, we can write the current operator as

$$I_k(x) = \frac{kA_k}{L_0}\sqrt{\frac{\hbar}{2C_{\text{cav}}\omega_k}}\sin(k(x+\ell))\left(a_k^\dagger + a_k\right) . \tag{3.86}$$

Assuming coherent states, it holds that [22, 89]

$$\langle a_k^\dagger + a_k\rangle \sim 2\sqrt{n_k}\,. \tag{3.87}$$

Taking $\langle I_k(x)\rangle = I_c$, this in turn gives the maximum photon population at which the critical current is reached:

$$n_{\text{max}} \approx \frac{I_c^2}{4}\left[\frac{kA_k}{L_0}\sqrt{\frac{\hbar}{2C_{\text{cav}}\omega_k}}\sin(k\ell)\right]^{-2} \tag{3.88}$$

where we have assumed the junctions to be at $x = 0$. For typical junction and resonator parameters, this critical photon number ranges from about $n \sim 6$ photons at $\Phi = \Phi_0/2$ to about $n \sim 80$ at zero flux bias [89].

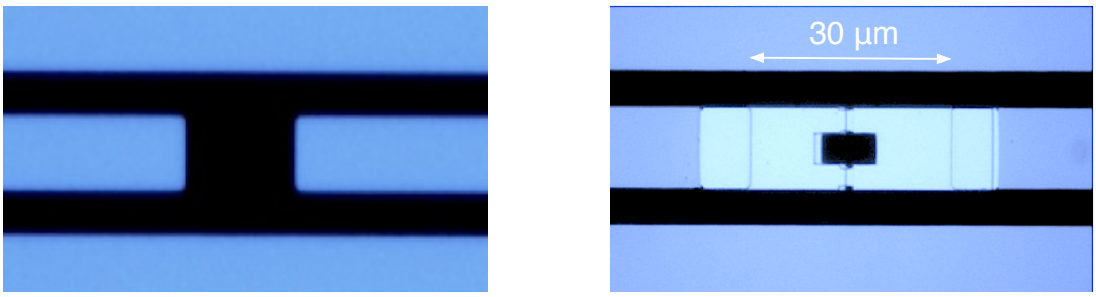

Figure 3.12: Center conductor gap before deposition (left) and typical asymmetric SQUID loop fabricated in the center pin (right). The niobium metallization is shown in blue, the alumnium layers in cyan and the sapphire substrate in black.

3.2.5 Design and Device Fabrication

Superconducting transmission line cavities can be realized using well-established micro- and nano-fabrication techniques known from conventional chip technology. One of the great advantages of the samples used in this thesis lies in their simplicity. All the devices that have been designed, fabricated and measured within this thesis consist of only one respectively two metal layers on a single-crystal substrate with no need for additional crossovers or deposited dielectrics. In that way, we have to employ only minimal fabrication which greatly limits materials complexity. Detailed discussions of the fabrication process for regular transmission line resonators can be found Refs. [92, 95]. Here, we focus on the fabrication of tunable resonators incorporating a SQUID loop.

In order to realize flux-tunable coplanar waveguide resonators, we have employed a two-step process in which the resonator and the SQUID are fabricated separately. The design of an optical lithography mask represented the starting point. Around 30 resonator designs with different lengths, coupling capacitances and SQUID junctions have been developed in the framework of this thesis. The lithography mask is used for patterning the different resonator structures on a two inch wafer consisting of 180 nm pure, superconducting niobium on a 500 μm single-crystal sapphire substrate. The wafer is first coated with UV-sensitive resist using a standard spinning technique. In a 'hard contact' lithography process, the optical mask is precisely aligned on top of the wafer and consequently UV exposed. The exposed niobium areas can then be etched away using either dry or wet etching techniques. To allow for the possibility to incorporate a SQUID loop into the center pin of the resonator, all mask designs have a 30 μm wide gap in the center conductor of the resonator. This gap is etched into the Niobium layer along with the rest of the structure in the optical lithography step. Once etching is finished, the two inch wafer is diced into single 2×7 mm chips each containing an individual resonator.

The aluminum SQUIDs are then fabricated in the second step using electron beam lithography and double-angle aluminum deposition. An important point before the actual SQUID fabrication is to clean the niobium surface of the resonators and remove any oxide layers. Since the resonator structures and the SQUIDs are fabricated separately, the niobium surface can oxidize in between the two steps, resulting in NbO_x layers of several nm thickness. If the Aluminum SQUIDs were fabricated right on top of this layer, large contact resistances are possible and the $Nb/NbO_x/Al$

interface can in fact form a tunnel junction itself. In order to avoid this, the oxide layers are removed using ion gun etching (*Veeco* 3 cm Argon DC Ion Source) with a beam current of 10 mA and a voltage of 300 V, respectively. Each sample is exposed for 180 s, a time interval for which no measurable Nb/Al contact resistances could be observed anymore. Details about the ion gun and the determination of the corresponding etching rates for the different materials in our fabrication process are given in appendix B. Once the niobium surface is cleaned, the chip is coated with a double-layer resist structure. This step is done right after ion gun etching in order to avoid regrowing of oxide layers. MMA resist is first spun onto the surface at 3000 rpm for 60s followed by a layer of pure (1:1) PMMA 950K (same spinning parameters). The SQUID structure and the two Josephson junctions are then patterned at the position of the 30 μm center pin gap using electron beam lithography and consequently developed in MIBK. In the following, the aluminum junctions are fabricated using double-angle evaporation, where the bottom layer is deposited under $+30^\circ$ (30 nm Al) and the top layer under -30° (150 nm Al). Finally, the remaining resist layers are lifted off in an aceton bath. A typical SQUID-loop fabricated in the center conductor is shown in Fig. 3.12 together with a picture of the center pin gap prior to deposition.

4 Circuit Quantum Electrodynamics

The successful strong coupling of a superconducting charge qubit to a coplanar waveguide cavity marked a major milestone on the road towards solid state quantum information processing and triggered a whole new exciting field, now known as *circuit quantum electrodynamics* [1, 2, 3]. This novel architecture represents a solid-state analog of traditional atomic cavity QED systems and has allowed to realize a number of fascinating on-chip quantum optics experiments [2, 4, 5, 6, 9, 19]. Over the course of the last five years, the circuit QED architecture has become a high accuracy testbed for probing the interaction of matter and light on the level of single quanta and it quickly evolved into a promising system for future solid-state quantum computing. While charge, phase and flux qubits have been actively investigated for more than a decade, only recently the coherent coupling of these systems to single microwave photons stored inside a transmission line resonator demonstrated their true potential for scalable quantum information processing. This chapter discusses the underlying theory of circuit and cavity quantum electrodynamics.
First, the Jaynes-Cummings model is introduced, which provides a universal description of the most fundamental system for testing matter-light interactions, a two-level system coupled to a single-mode electromagnetic field [100, 22]. In the following, we will couple the Cooper pair box qubits of chapter 2 to the transmission line resonators of chapter 3 and show, that the resulting system represents a specific physical realization of the Jaynes-Cummings model. Since we use transmons rather than Cooper pair boxes in all of the experiments in this thesis, section 4.2 will spent some time on discussing the case of a coupled transmon-resonator system. Finally, we will consider the coupling of a superconducting qubit to the non-linear, flux-tunable cavity of section 3.2.

4.1 Coupling Superconducting Qubits to Cavities

4.1.1 Jaynes-Cummings Interaction

The most fundamental system for studying the interaction of matter and light is a two-level atom interacting via dipole coupling with a single-mode radiation field. This represents the simplest possible form of the atom-field interaction and is known as the so-called Jaynes-Cummings model [22, 100]. A quantized radiation field in free space is most generally described as an infinite sum over harmonic oscillator Hamiltonians

$$H_R = \sum_k \hbar\omega_k \left(a^\dagger a + \frac{1}{2} \right) \tag{4.1}$$

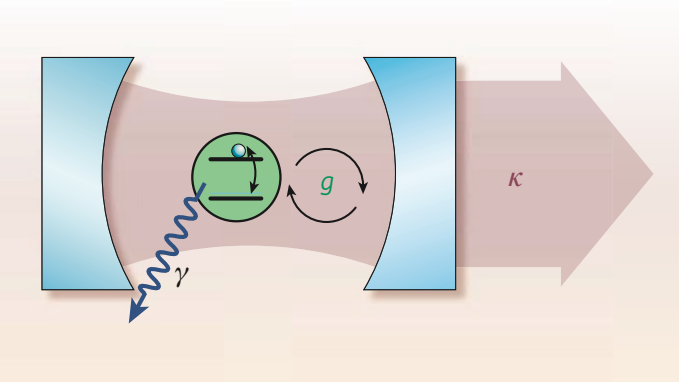

Figure 4.1: Sketch of a cavity QED system (taken from [3]). Quantum-mechanical two-level system (green) coupled via dipole interaction to a single-mode radiation field with photon decay rate κ.

where each mode k is an harmonic oscillator of frequency ω_k whose excitation number n equals the number of photons $\langle a^\dagger a \rangle$ in the mode. In its ground state, each of these oscillators has a non-vanishing zero-point energy $\hbar\omega_k/2$ resulting from the vacuum field fluctuations. This is a consequence of energy-time uncertainty which allows virtual photons to constantly pop into and out of existence. The interaction with the vacuum radiation field is also the underlying reason for the spontaneous emission of any quantum system [22]. Now a general radiation field contains an infinite number of modes k, with the mode density depending on the specific boundary conditions of the physical volume V under consideration [101]. In free space, we have $V \to \infty$ which leads to a continuous mode density. An atom or an ideal two-level system placed in such a 'free space field' will then couple to a very large number of modes, making it almost impossible to study its interaction on the level of single quanta. In that case, the atom has an infinity of vacuum states available for the spontaneous emission of radiation. If the boundary conditions do, however, only allow for a *single* relevant mode, the mode density is reduced to a δ-function and the coupling of the atom is drastically modified. If the atom's transition frequency ω_a matches the mode frequency, it will couple strongly to the field and the process of spontaneous emission is greatly enhanced. On the other hand, if the two frequencies are off-resonant, the emission and absorption by the atom are effectively suppressed [14, 22]. This situation is realized in a cavity whose spatial dimensions are comparable to the wavelength: Such a cavity will only support modes whose wavelengths are compatible with its size. For optical frequencies, a cavity is realized by a pair of two parallel mirrors whose separation sets the boundary conditions. An isolated atom placed between these two mirrors then also only couples to the supported modes and the total system realizes a Jaynes-Cummings Model, as depicted schematically in Fig. 4.1. The ideal two-level atom is described by the simple Hamiltonian

$$H_A = \frac{\hbar\omega_a}{2}(|1\rangle\langle 1| - |0\rangle\langle 0|) = \frac{\hbar\omega_a}{2}\sigma_z \tag{4.2}$$

and it couples to the field via a standard dipole interaction

$$H_I = -\frac{e}{mc}(\vec{p}\vec{A}) \tag{4.3}$$

where $\vec{A}$ is the vector potential of the electromagnetic field and $\vec{p}$ and m the atomic electron's momentum and mass, respectively. In the dipole approximation for the vector potential $\vec{A}(\vec{R}) \approx \vec{A}(0)$, the interaction simplifies to

$$H_I = g(a + a^\dagger)(\sigma^+ - \sigma^-) \tag{4.4}$$

where we have used the commutators of $\vec{r}, \vec{p}$ and H_A and introduced $\sigma^+ = |1\rangle\langle 0|, \sigma^- = |0\rangle\langle 1|$. Here, the coupling strength between atom and radiation field was defined

$$g = \frac{E_{\text{rms}} d}{\hbar} = \sqrt{\frac{\omega_k}{2\hbar\varepsilon_0 V}} d \tag{4.5}$$

which is the product of the dipole matrix element of the atom d and the zero-point electric field of the mode E_{rms}, with ε_0 denoting the permittivity of free space and V the size of the quantization volume, i.e the effective mode volume of the cavity. The coupling strength increases with decreasing mode volume so that cavities with smaller dimensions will give stronger interaction between atom and radiation field. Applying the rotating-wave approximation to H_I by neglecting all counter-rotating terms $a\sigma^-$ and $a^\dagger\sigma^+$ gives

$$H_I = \hbar g(a^\dagger\sigma^- + \sigma^+ a)\,. \tag{4.6}$$

This Hamiltonian describes the simple process of emission and absorption in the cavity. A photon bouncing back and forth between the two mirrors can be absorbed by the atom in its ground state ($\sigma^+ a$). Similarly, if the atom is excited it can decay back to the ground state by emitting a photon into the cavity ($a^\dagger\sigma^-$). The rate of this atom-photon interaction is given by the coupling strength g. In a real system, photons leak out of the cavity at a rate $\kappa = \omega_r/Q$ determined by the quality factor of the cavity. In addition, the atom exhibits decoherence (i.e. energy relaxation) and decays at a corresponding rate γ. Summing up the different terms and accounting for the loss mechanisms, the total system is finally described by the Jaynes-Cummings Hamiltonian

$$\begin{aligned} H_{\text{JC}} &= H_R + H_A + H_I + H_\gamma + H_\kappa \\ &= \hbar\omega_r\left(a^\dagger a + \frac{1}{2}\right) + \frac{\hbar\omega_a}{2}\sigma_z + \hbar g(a^\dagger\sigma^- + \sigma^+ a) + H_\gamma + H_\kappa \end{aligned} \tag{4.7}$$

where we have set the resonance frequency of the cavity $\omega_r = \omega_k$. This Hamiltonian has a quite universal character and is not only used to describe the interaction of real atomic systems, but also for so-called artificial atoms such as quantum dots [30], micromechanical systems [102] or in particular superconducting qubits [1, 2].

In the microwave regime of solid-state circuit QED, the cavity is realized in the form of a quasi one-dimensional, coplanar transmission line resonator discussed in chapter 3 and the role of the two-level atom is played by a superconducting charge qubit as presented in chapter 2. The coupling of the two systems is achieved by fabricating the qubit directly inside the resonator such that the superconducting island sits between the center conductor and the ground planes of the CPW, as sketched in Fig. 4.2a. In that way, the qubit couples capacitively to the center con-

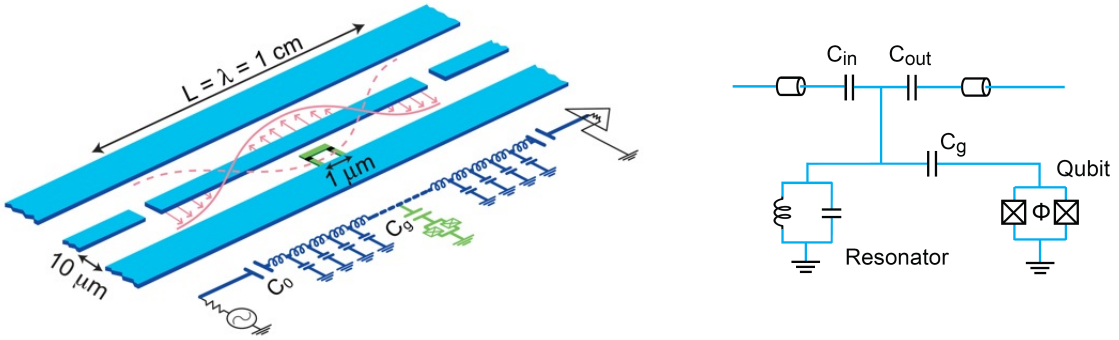

Figure 4.2: (a) Sketch and lumped element circuit model of a superconducting transmission line resonator (blue) coupled to a Cooper pair box (green) (taken from [1]). (b) Equivalent circuit diagram of the coupled qubit-cavity system.

ductor of the resonator, which can be expressed by the equivalent electrical circuit in Fig. 4.2b. The total qubit-cavity system then realizes a Jaynes-Cummings interaction [1] and is governed by the exact same Hamiltonian (4.7) as a real atom coupled to an optical cavity field. Here, the oscillator frequency ω_r is determined by the geometric and electrical properties of the CPW resonator and the atom transition frequency ω_a is given by the CPB level separation in the two state-approximation (see section 2.5.2)

$$\hbar\omega_a = \sqrt{E_{\mathrm{el}}^2 + E_{\mathrm{J0}}^2} = \sqrt{(4E_{C0}(1-n_g)^2 + E_{J0}^2}\,. \tag{4.8}$$

The typical separation between ground planes and center pin is on the order of a few μm with resonator lengths of about $\ell \sim 1$ cm so that the photons of the TEM field are tightly confined in the transversal dimension (see chapter 3). This in turn leads to large rms zero-point electric fields of about 0.2 V/m and hence to significant coupling strengths of currently up to $g/2\pi \sim 130$ MHz [1, 3]. By comparison, traditional atomic cavity QED realizes couplings of about $g/2\pi \sim 150$ MHz [103]. The relevant quantity, however, is the dimensionless coupling strength g/ω_r where we have about 2.5×10^{-2} for 1D transmission line resonators and only 3×10^{-7} for 3D optical cavities [1]. The capactive coupling of qubit and resonator can be expressed explicitly by considering the voltage operator derived in the quantization of the LC oscillator in section 3.1.2

$$V = \sqrt{\frac{\hbar\omega_r}{2C}}(a - a^\dagger)\,. \tag{4.9}$$

This quantum voltage $V = q/C$ is solely due to the photons in the single-mode radiation field and couples to the qubit with a strength determined by the gate capacitance C_g and the capacitance between center pin and ground plane C. Now plugging this into the electrostatic qubit Hamiltonian (2.65) as an additional voltage to the gate voltage gives a coupling term $H_c = 2g\hbar(a^\dagger + a)N$ with strength

$$g = \frac{e}{\hbar}\frac{C_g}{C_\Sigma}\sqrt{\frac{\hbar\omega_r}{2C}} = \frac{e}{\hbar}\beta V_{\mathrm{rms}}^0 \tag{4.10}$$

where $C_\Sigma = C_g + C_J + C + C_s$ with C_s accounting for possible stray capacitances. In the last step, the zero-point voltage fluctuations in the resonator $V^0_{\text{rms}} = \sqrt{\hbar\omega_r/2C}$ have been defined, which correspond directly to the rms vacuum field strengths in (4.5). Note that half of the zero point energy is stored in the electric field and half is in the magnetic field. Interestingly, there is a fundamental upper bound for the magnitude of the coupling, which limits the coupling strength to about 10 % of the resonator frequency ω_r [3, 69]. This can be seen explicitly by rewritting the dimensionless coupling strength g/ω_r in terms of the fine structure constant, see Ref. [5]. Comparing (4.10) to the general coupling strength $\hbar g = E_{\text{rms}} d$ as defined above, the Cooper pair box can be assigned an effective dipole moment $d = e\beta w$, where we have used $E_{\text{rms}} = V_{\text{rms}}/w$ with w denoting the separation between ground plane and center pin of the resonator. In that sense, the Cooper pair box can be thought of as a molecule inside an electric field generated by the gate voltage V_g across a width w.

4.1.2 Resonant Strong Coupling Limit

The strong coupling regime of cavity QED is obtained when the rate of photon absorption and emission g by the atom exceeds any of the two loss rates $g \gg \kappa, \gamma$ [14, 22]. This can be achieved by a combination of long coherence times, high Q cavities and large coupling strengths. In this regime, the leakage terms in the Jaynes-Cummings Hamiltonian can be effectively neglected so that it becomes possible to exactly diagonalize (4.7). Here, zeroth order degenerate perturbation theory already yields the exact eigenenergies. Using the product states $|\downarrow, n\rangle = |\downarrow\rangle \otimes |n\rangle$ and $|\uparrow, n+1\rangle = |\uparrow\rangle \otimes |n+1\rangle$ as the unperturbed eigenstates, where $|\downarrow,\uparrow\rangle$ denote the qubit eigenstate and $|n\rangle$ the photon number states of the cavity, it follows for the dressed excited eigenstates of the Jaynes-Cummings Hamiltonian

$$|+, n\rangle = \cos\Theta_n\,|\downarrow, n\rangle + \sin\Theta_n\,|\uparrow, n+1\rangle \tag{4.11}$$

$$|-, n\rangle = -\sin\Theta_n\,|\downarrow, n\rangle + \cos\Theta_n\,|\uparrow, n+1\rangle \tag{4.12}$$

with the mixing angle

$$\Theta_n = \frac{1}{2}\arctan\left(\frac{2g\sqrt{n+1}}{\Delta}\right) \tag{4.13}$$

and the qubit-cavity detuning $\Delta = \omega_a - \omega_r$. Note that the ground state of the coupled system is simply $|\uparrow, 0\rangle$. The corresponding eigenenergies are given by

$$E_{\pm,n} = (n+1)\hbar\omega_R \pm \frac{\hbar}{2}\sqrt{4g^2(n+1) + \Delta^2}\,, \tag{4.14}$$

$$E_{\uparrow,0} = -\frac{\hbar\Delta}{2} \tag{4.15}$$

and the energy level diagram is depicted in Fig. 4.3. One can distinguish between two qualitatively different regimes depending on the detuning Δ between qubit and cavity. For $\Delta > g$, qubit and cavity interact only dispersively and the unperturbed product states $|\downarrow, n\rangle = |\downarrow\rangle \otimes |n\rangle$ and $|\uparrow, n+1\rangle = |\uparrow\rangle \otimes |n+1\rangle$ are to a good approximation eigenstates of the Hamiltonian. This case will be discussed separately in section 4.1.3. On or near resonance $\Delta \to 0$, the excited

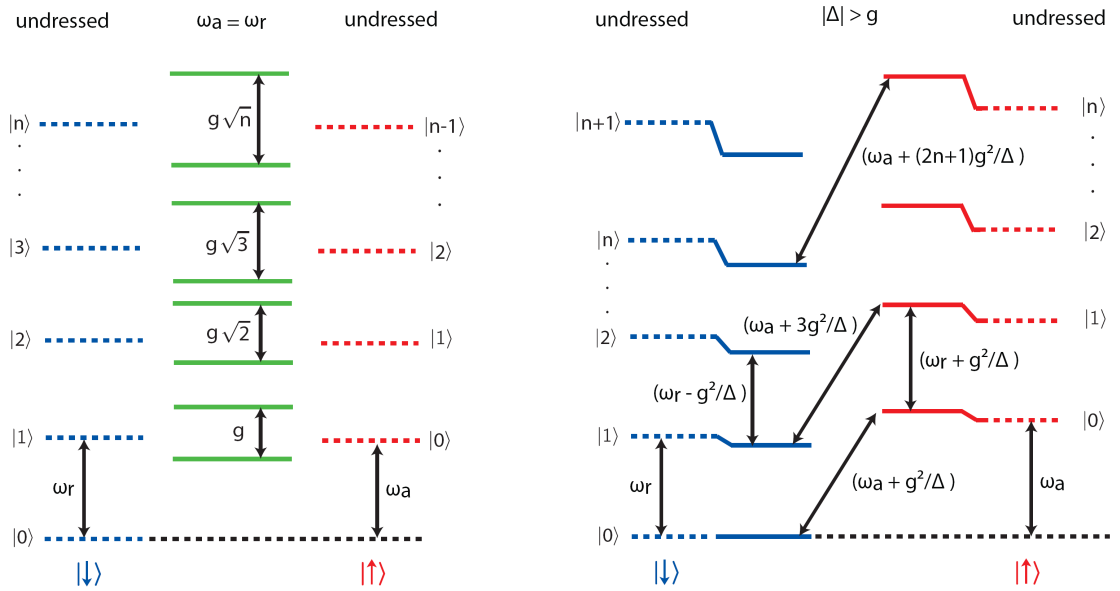

Figure 4.3: Energy levels of the Jaynes-Cummings Hamiltonian. (a) The dashed lines are the eigenstates of the uncoupled Hamiltonian, where left is qubit in the ground state and right in the excited state with $|n\rangle$ corresponding to the different photon number states. The solid lines are the energies in the presence of the dipole coupling. Both strong dispersive (right) and resonant strong regime (left) are shown with the energy level separations and dispersive shifts indicated accordingly (see discussion in the text).

eigenstates $|+/-, n\rangle$ are superpositions of the unperturbed states whose weight is determined by the mixing angle Θ_n. In the resonant limit $\Delta \to 0$ we have $\Theta_n \to \pi/2$ and the superposition states become equally weighted

$$|\pm, n\rangle = \frac{1}{\sqrt{2}} \left(|\uparrow, n+1\rangle \pm |\downarrow, n\rangle \right). \tag{4.16}$$

Thus for zero detuning, the excited eigenstates of the qubit-resonator system are maximally entangled and all excitations are equally shared between the qubit and the photon field. The two systems can then no longer be considered as separate entities in a quantum description. Indeed, an excitation placed in such a system will in fact coherently oscillate between qubit and cavity-photons, as can be seen explicitly from the time evolution of the system. For zero detuning, the probability for the qubit being in the excited state $|\uparrow\rangle$ and the resonator containing $n+1$ photons at time t can be calculated using $|\uparrow, n+1\rangle = (1/\sqrt{2})(|+, n\rangle + |-, n\rangle)$ so that

$$P_{\uparrow,n+1} = \left| \langle n+1, \uparrow | e^{-iH_1 t/\hbar} | \uparrow, n+1 \rangle \right|^2 = \cos^2(g\sqrt{n}t) \quad , \quad P_{\downarrow,n} = 1 - P_{\uparrow,n+1}\,. \tag{4.17}$$

Thus the excitation oscillates between qubit and cavity-photon at a frequency $\nu_{\text{rabi}} = g\sqrt{n}$. These oscillations are referred to as vacuum Rabi oscillations at the Rabi frequency ω_{rabi} and their observation represents an unambiguous proof that strong coupling between resonator and qubit has been achieved[22, 101]. Observing these oscillations naturally requires realizing a coupled system in which the coupling rate exceeds all decay rates $g > \kappa, \gamma$.

The observation of vacuum Rabi oscillations is very closely related to the so-called vacuum Rabi splitting. The superposition states (4.16) have a non-linear energy level spectrum (see Fig. 4.3) and they are separated by

$$\Delta E_n = \hbar g\sqrt{n} \tag{4.18}$$

which in turn results in two peaks separated by $g\sqrt{n}$ in a transmission measurement of the cavity. These peaks correspond to the transitions from the ground state to the two excited states of the system, as depicted in the center column of the energy level diagram Fig. 4.3. This splitting is clearly resolved in all of our experiments and will be discussed in detail in chapter 5.

4.1.3 The Dispersive Regime: Lamb and Stark Shifts

The resonant interaction of qubit and cavity allows for free, coherent exchange of energy and the two systems lose their individual character in this limit. A qualitatively different regime of circuit QED is obtained when qubit and cavity are far detuned from each other so that $\Delta > g$. In this dispersive limit of large detunings between qubit and cavity field, the interaction manifests itself only in the form of frequency shifts and the Jaynes-Cummings Hamiltonian can be effectively decoupled. Making a Schrieffer-Wolf-type transformation [1]

$$U = \exp\left[\frac{g}{\Delta}(a\sigma^+ - a^\dagger\sigma^-)\right] \tag{4.19}$$

of the Hamiltonian (4.7) and expanding to second order in the small parameter $g/\sqrt{\Delta}$ gives the effective Hamiltonian

$$H_{\text{eff}} = UHU^\dagger \approx \hbar\omega_r\left(a^\dagger a + \frac{1}{2}\right) + \frac{\hbar}{2}\left(\omega_a + 2\frac{g^2}{\Delta}a^\dagger a + \frac{g^2}{\Delta}\right)\sigma_z \tag{4.20}$$

in which the term H_I in Eq. (4.7) was adiabatically eliminated. The qubit-cavity interaction is now reduced to frequency shifts. The undressed qubit frequency ω_a experiences a shift from the populated cavity field with $n = \langle a^\dagger a\rangle$ photons, the ac Stark shift $\delta_S = 2\chi n = 2(g^2/\Delta)n$, as well as a virtual photon shift $\delta_L = \chi$ due to its interaction with the vacuum field fluctuations $\langle a^\dagger a\rangle = 0$, the Lamb shift. In other words, the presence of both 'real' and virtual photons inside the cavity manifests itself as a renormalization of the energy of the qubit. The ac Stark and the Lamb shift are closely related to the Rabi splitting in the near-resonant case as can also be seen from the energy level diagram Fig. 4.3. The Lamb shift represents the dispersive remains of the vacuum Rabi splitting whereas the ac Stark shift corresponds to the splittings higher up the Jaynes-Cummings ladder with photon numbers $n > 0$ [88].
The dispersive interaction does also have an effect on the cavity frequency. To highlight this, we regroup the effective Hamiltonian:

$$H_{\text{eff}} = \hbar\left(\omega_r + \frac{g^2}{\Delta}\sigma_z\right)\left(a^\dagger a + \frac{1}{2}\right) + \hbar\frac{\omega_a}{2}\sigma_z\,. \tag{4.21}$$

Apparently, the cavity resonance ω_r acquires a qubit-state-dependent shift given by $\langle\sigma_z\rangle\,(g^2/\Delta) = \pm(g^2/\Delta)$. The qubit-state-dependent cavity frequency shift forms the basis of quantum non-demolition readout in circuit QED systems [1, 104]. An ideal QND measurement allows repeatedly measuring a quantum-mechanical system without altering its state. In the Heisenberg picture, this means that the measurement operator A does not change during the time we are measuring and thus it has to fulfill the equation of motion

$$\frac{dA}{dt} = \frac{1}{i\hbar}[A, H] = 0 \tag{4.22}$$

i.e. it has to commute with the Hamiltonian. In the dispersive circuit QED regime, all of the individual terms in H_{eff} commute with the total Hamiltonian and thus the cavity shift $\pm(g^2/\Delta)$ can be used to readout the qubit state $\langle\sigma_z\rangle = \pm 1$ in a QND-type measurement.
Note that dispersively it also possible to exactly diagonalize the Jaynes-Cummings Hamiltonian in the basis of the decoupled states $|\downarrow, n\rangle = |\downarrow\rangle \otimes |n\rangle$ and $|\uparrow, n+1\rangle = |\uparrow\rangle \otimes |n+1\rangle$. This can be achieved by applying an exact dispersive transformation to the full Lindblad master equation of the system [105]. In that case the Lamb and Stark shifts are given by the exact expressions [105]

$$\delta_{\text{L}} = \frac{\Delta}{2}\left(\sqrt{1+4\lambda^2} - 1\right) \tag{4.23}$$

$$\delta_{\text{S}}(n) = \frac{\Delta}{2}\left(\sqrt{1+4\lambda^2(n+1)} - \sqrt{1+4\lambda^2} + \sqrt{1+4\lambda^2 n} - 1\right) \tag{4.24}$$

where we have defined $\lambda = g/\Delta$. A Taylor expansion around $\lambda = 0$ shows that these expressions can be reduced to the Lamb and Stark shifts derived above. Such an exact dispersive transformation is, however, conditioned by the degree to which the artificial atom realizes an ideal two-level system. For a regular Cooper pair box, such a transformation can be found, in contrast to the case of a transmon qubit.

4.2 Circuit QED for Transmon Qubits

In the discussion of cavity and circuit QED so far, the artificial atom was regarded as a perfect two-level system that has no higher energy states. Owing to the strong degree of level anharmonicity, it was shown in section 2.5.2 that this is indeed true to a very good approximation for a Cooper pair box. In the transmon design derived from the CPB, we saw, however, that a certain degree of anharmonicity is traded in for a decrease in charge noise sensitivity. Luckily, these two quantities scale differently, the latter one decreasing exponentially in the ratio E_J/E_C while the first one only does so with a weak power law [69, 70]. It was shown that there exists a parameter range of E_J/E_C values in which both charge noise insensitivity as well as sufficient anharmonicity for qubit operation are possible. However, the main price to pay for using the transmon is to keep track of its higher energy levels in a circuit QED treatment. All of the qubit experiments presented in this thesis were carried out with transmon qubits rather than conventional Cooper pair boxes and thus this section will spend some time on discussing the important implications

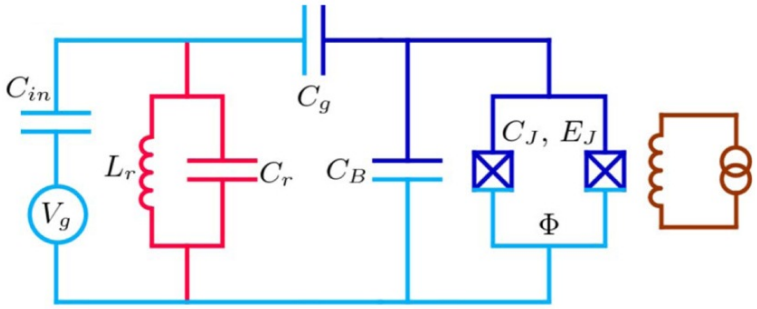

Figure 4.4: Equivalent circuit diagram of a Transmon qubit coupled to a transmission line cavity [69].

this has on the whole circuit QED system.

In analogy to the CPB case, the transmon is embedded directly inside the resonator and coupled capacitively to the center conductor. This time, however, the superconducting qubit has an additional large shunting capacitance C_B, as shown in the equivalent circuit diagram Fig. 4.4. C_B changes the capacitance ratio β and thus also the actual coupling strength (4.10). As discussed in section 2.7, the transmon is described by the same Hamiltonian as the CPB and thus the Hamiltonian of the coupled qubit-cavity system is also given by [69]

$$H = 4E_C(N - n_g)^2 - E_J(\Phi)\cos\phi + \hbar\omega_r\left(a^\dagger a + \frac{1}{2}\right) + 2\beta e V_{\text{rms}} N(a + a^\dagger)\,. \tag{4.25}$$

In the CPB case, we have used the two-state approximation for the qubit Hamiltonian to realize a Jaynes-Cummings model from this. For the transmon, however, it is important to also account for the higher energy levels. Rewriting (4.25) in the basis of the undressed transmon states $|i\rangle$ and applying the rotating wave approximation yields [69]

$$H = \hbar\sum_j \omega_j |j\rangle\langle j| + \hbar\omega_r\left(a^\dagger a + \frac{1}{2}\right) + \left[\hbar\sum_i g_{i,i+1}|i\rangle|i+1\rangle\, a^\dagger + \text{h.c.}\right] \tag{4.26}$$

which represents an effective, generalized Jaynes-Cummings Hamiltonian. Here, the coupling strength of the transition $|i\rangle \to |i+1\rangle$ reads

$$g_{i,i+1} = \frac{2e}{\hbar}\beta V_{\text{rms}}\langle i|N|i+1\rangle \approx \frac{2e}{\hbar}\beta V_{\text{rms}}\sqrt{\frac{i+1}{2}}\left(\frac{E_J(\Phi)}{8E_C}\right)^{1/4} \tag{4.27}$$

with $\beta = C_g/C_\Sigma$, $C_\Sigma = C_B + C_g + C$. Apparently, the coupling strength also depends on the ratio of Josephson to charging energy and even increases weakly with E_J/E_C. This comes somewhat as a pleasant side-effect and has helped the second generation of circuit QED experiments to go even deeper into the strong-coupling regime [5, 9, 6, 88]. The dispersive regime of the transmon-cavity interaction is especially interesting for the experiments presented in this thesis. Using a canonical transformation similiar to the Schrieffer-Wolf transformation discussed before,

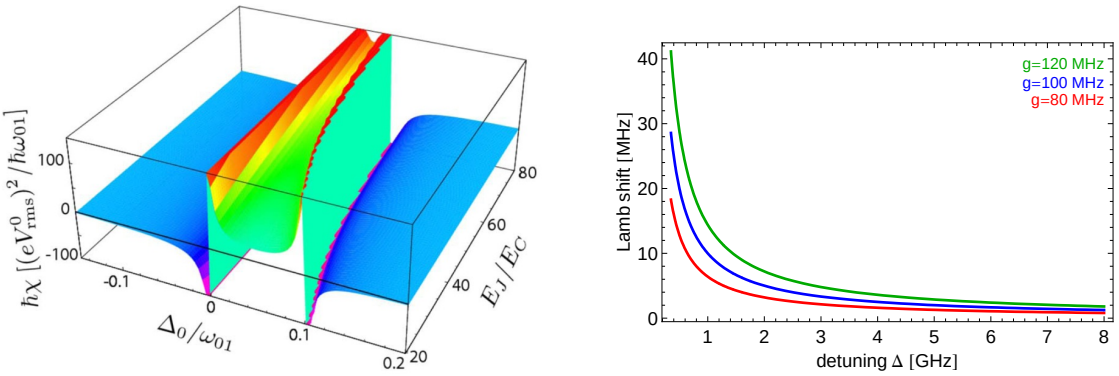

Figure 4.5: (a) Dispersive shift χ in transmon circuit QED as a function of normalized detuning Δ_{01}/ω_{01} and the ratio E_J/E_C [69]. (b) Lamb shift as a function of detuning for three different typical coupling strengths.

one arrives to lowest order at the effective dispersive Hamiltonian [69]

$$\mathcal{H}_{\rm eff} = \hbar\omega_r' \left(a^\dagger a + \frac{1}{2}\right) + \frac{\hbar}{2}\left(\omega_{01} + \chi_{01} + 2\chi a^\dagger a\right)\sigma_z \tag{4.28}$$

where

$$\omega_r' = \omega_r - \frac{\chi_{12}}{2} \quad , \quad \chi = \chi_{01} - \frac{\chi_{12}}{2} \tag{4.29}$$

$$\chi_{ij} = \frac{g_{ij}^2}{\omega_{ij} - \omega_r} \equiv \frac{g_{ij}^2}{\Delta_{ij}}\,. \tag{4.30}$$

Here ω_{ij} denotes the bare, undressed frequency of the transition $i \to j$. Note that in the transmon case both qubit *and* cavity resonances are renormalized simultaneously. The cavity resonance acquires a slight shift due the presence of the third transmon level $\omega_r' = \omega_r - \chi_{12}/2$. The original Stark shift per photon in the qubit frequency is also modified to $\delta_S = 2\chi = 2\chi_{01} - \chi_{12}$. Only the Lamb shift due to the interaction with the virtual photons stays the same

$$\delta_{\rm L} = \chi_{01} = \frac{g_{01}^2}{\Delta}\,. \tag{4.31}$$

The dispersive shift χ is plotted in Fig. 4.6a as a function of normalized detuning Δ_{01}/ω_{01} and the ratio E_J/E_C [69]. Three distinct regions separated by the two poles are identified: A negative dispersive shift is observed for negative detunings Δ_{01} as well as for positive detunings exceeding the charging energy $\Delta_{01} > E_C$. In the range of small positive detunings $0 < \Delta_{01} < E_C$, the shift becomes positive.

Furthermore, we see from the new Lamb and Stark shift expressions that it has become possible for the qubit vacuum interaction to exceed the coupling to the actual photon field. The Stark shift per photon is reduced by the third transmon level by a factor of χ_{12} which can reach significant values for small anharmonicities. The qubits used in our experiments are operated deep in the transmon regime $E_J(0)/E_C \simeq 160$ with minimum anharmonicities of $\alpha = E_{01} - E_{12} \simeq 240\,\text{MHz}$. As demonstrated in chapter 5, we indeed reach the case of $2\chi < \chi_{01}$ in which the Lamb shift

exceeds the Stark shift per photon.
General plots of the Lamb shift as a function of detuning Δ are shown in Fig. 4.6b for different coupling strengths. As can be seen, the Lamb shift converges towards zero for large detunings, allowing to effectively 'switch it off' by far detuning cavity and qubit. Note, however, that in reality one also has to account for higher cavity modes. On the other hand, δ_L strongly increases for $\omega_r \to \omega_a$, producing large shifts in the dressed qubit transition $\widetilde{\omega}_a = \omega_a + \delta_L$ for small detunings. For $\Delta = 0$, all excitations in the system become equally shared between qubit and cavity and there are no separate transitions or energy levels anymore. This leads to the vacuum Rabi splittings discussed above and the pure qubit transition disappears. Chapter 5 will present the experimental observation of a smooth transition from Lamb shift to vacuum Rabi splitting.

4.3 Tunable Cavity - Qubit Systems

Following the discussion of cavity QED with Cooper pair boxes and transmons in sections 4.1 and 4.2, the final part of this chapter will focus on what circuit quantum electrodynamics looks like when using the flux-tunable cavity of section 3.2 instead of a regular transmission line cavity. The discussion is split into two parts. First, we will assume a linear tunable resonator where the Kerr-type non-linearity introduced by the SQUID is neglected. In that case, the physics stays essentially the same as in regular circuit QED systems, however, providing us with an additional control parameter in our experiments. The non-linear case accounting for the higher-order effects in the SQUID Josephson potential is then presented at the end of this section, where both the resonant strong and the dispersive limit are discussed in detail.

The Linear Case

In the generic treatment of the tunable cavity with the electrical model of section 3.2.1, the non-linearity introduced by the Josephson elements is effectively neglected and the presence of the SQUID simply leads to a flux-dependent resonance frequency $\omega_r(\Phi)$. The coupled CPB-cavity system is then described by the usual Jaynes-Cummings type interaction. The total Hamiltonian is written in complete analogy to regular circuit QED systems, except for the flux-dependent cavity resonance

$$H_{JC} = \hbar\omega_r(\Phi)\left(a^\dagger a + \frac{1}{2}\right) + \frac{\hbar\omega_a(\Phi)}{2}\sigma_z + \hbar g(a^\dagger\sigma^- + \sigma^+ a) + H_\gamma + H_\kappa\,. \tag{4.32}$$

In a typical experiment with a conventional qubit-transmission line resonator system, the modes of the resonator are fixed and the qubit resonance frequency is flux-tuned to enter the different regimes of circuit QED in the resonant ($\Delta = 0$) and the dispersive limit ($\Delta \gg g$). Using a tunable resonator, however, effectively allows switching the roles of qubit and cavity. For instance, in a Rabi splitting experiment, the qubit can be held at a fixed position in frequency space while the cavity is tuned in and out of resonance. Such an experiment is, however, quantitatively

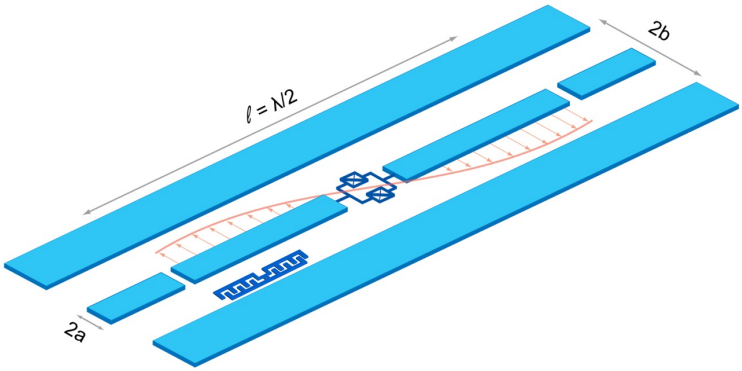

Figure 4.6: Sketch of a transmon qubit (dark blue) coupled to a flux-tunable superconducting cavity incorporating a SQUID loop at the center position.

different due to the dependence of the coupling strength on the cavity frequency which gives a flux-dependent Rabi splitting $\Delta E_n = \hbar g(\Phi)\sqrt{n}$. In that sense, also the Lamb and Stark shifts of the dispersive regime have different values.
The fact that entanglement ($\Delta \to 0$) and disentanglement ($\Delta \gg g$) can now be achieved by tuning the cavity rather than the qubit leads to a number of interesting possibilities. In section 2.7 it was shown that there exist flux sweet spots in the qubit parameter space at $\Phi = n\Phi_0, (n/2)\Phi_0$ at which the CPB becomes to first order insensitive to flux noise, in complete analogy to the charge sweet spots. Although flux noise is not the limiting factor at the current stage of superconducting qubit experiments, operating at these points would in principle lead to a decrease in dephasing and thus increased coherence times. This is, however, not possible in conventional circuit QED as we need to be able to tune the qubit in and out of resonance with the cavity. On the other hand, using a tunable transmission line resonator instead allows us to switch the roles of qubit and cavity as the active elements in our experiments. Here, we can keep the qubit at a fixed flux sweet spot and use the cavity for tuning in and out of resonance. Now since the resonator can also be used to mediate the coupling between two different qubits [8, 9], a tunable cavity would in turn allow entanglement between the two systems using only a single flux bias, as has been proposed theoretically in Ref. [10].

The Non-Linear Case

The situation becomes much more complicated when the non-linearity of the resonator is taken into account. In that case, the system is no longer described by a pure Jaynes-Cummings Hamiltonian. The second-order perturbative treatment of the SQUID Josephson potential gave

the anharmonic, single-mode resonator Hamiltonian (see section 3.2.3)

$$H = \hbar\left(\omega_k - \Delta\omega_k a_k^\dagger a_k\right)\left(a_k^\dagger a_k + \frac{1}{2}\right) \tag{4.33}$$

with the flux-dependent frequency shift

$$\Delta\omega_k \equiv \Delta\omega_k(\Phi) = \frac{E_j(\Phi)}{4\hbar}\left(\frac{2\pi}{\Phi_0}\Delta_k\right)^4 . \tag{4.34}$$

where coupling to all higher modes has been neglected. The qubit-nonlinear resonator system is then described by a Hamiltonian of the form

$$H = \hbar(\omega_k - \Delta\omega_k a_k^\dagger a_k)a_k^\dagger a_k + \frac{\hbar\omega_a}{2}\sigma_z + g_k\hbar(a_k^\dagger\sigma^- + \sigma^+ a_k) . \tag{4.35}$$

where the vacuum field fluctuations have been dropped for the moment. Solving the eigenvalue equation in zeroth order degenerate perturbation theory yields the exact eigenenergies

$$E_{1,2} = \hbar\omega_r(n+1) - \hbar\Delta\omega_r n(n+1) \pm \frac{1}{2}\sqrt{\left[\hbar\Delta_{ar} + \hbar\Delta\omega_r(2n+1)\right]^2 + 4\hbar^2 g^2(n+1)} \tag{4.36}$$

where we have dropped the mode index and introduced the detuning $\Delta_{ar} = \omega_a - \omega_r$. The excited eigenstates of the system are then written in analogy to section 4.1.2 as

$$|+, n\rangle = \cos\Theta_n\,|\downarrow, n\rangle + \sin\Theta_n\,|\uparrow, n+1\rangle \tag{4.37}$$

$$|-, n\rangle = -\sin\Theta_n\,|\downarrow, n\rangle + \cos\Theta_n\,|\uparrow, n+1\rangle \tag{4.38}$$

where, however, the mixing angle of the states has acquired an additional flux-dependence

$$\Theta_n = \frac{1}{2}\arctan\left(\frac{2g\sqrt{n+1}}{\Delta_{ar} + \Delta\omega_r(\Phi)(2n+1)}\right) . \tag{4.39}$$

Maximum entanglement between CPB and tunable cavity is then achieved for

$$\Delta\omega_r = \frac{1}{2n+1}(\omega_r - \omega_a) \tag{4.40}$$

which results in the Bell-states (4.16). The corresponding vacuum Rabi splitting then turns out to be photon-number dependent

$$\Delta E^n_{\text{rabi}} = \sqrt{\hbar^2\Delta_{ar}^2 + 4\hbar^2 g^2(n+1)} . \tag{4.41}$$

These simple calculations already hint at the rich physics to be found in such a non-linear cavity qubit device. Ultimately, this system no longer consists of a harmonic and an anharmonic oscillator. It merely has to be thought of as the coupled system of two different forms of anharmonic oscillators, a photonic and a superconducting one. The photon number dependence in both the mixing angle as well as the Rabi splitting is a consequence of the 'self-Stark shift' of the cavity $\delta_S = \Delta\omega_k a_k^\dagger a_k$ that pulls itself through the whole calculation. Some of the fascinating

possibilities that arise from this shift are discussed in section 3.2.3.
In the dispersive regime of large detunings $\Delta \gg g$, the interaction term in (4.33) can be adiabatically eliminated in the same way as was done in the linear Jaynes-Cummings Hamiltonian. We get for the effective dispersive Hamiltonian

$$H_{\text{eff}} = \hbar(\omega_k' - \Delta\omega_k a_k^\dagger a_k) a_k^\dagger a_k + \hbar\left(\frac{\omega_a}{2} - \chi\left(1 + \frac{\Delta\omega_k}{\Delta}\right) - 4\frac{\chi}{\Delta}\Delta\omega_k a_k^\dagger a_k\right)\sigma_z \tag{4.42}$$

where

$$\omega_k' = \omega_k + \chi - \frac{\chi}{\Delta}\Delta\omega_k \quad , \quad \Delta\omega_k' = \Delta\omega_k\left(1 - \frac{\chi}{\Delta}\right) \tag{4.43}$$

In analogy to the linear case, the qubit experiences a Lamb and an ac Stark shift. The Lamb shift due to the virtual photons inside the cavity takes the form $\delta_{\text{L}} = \chi + (\chi/\Delta)\Delta\omega_k$, while the ac Stark shift is identified as $\delta_S = 4(\chi/\Delta)\Delta\omega_k a_k^\dagger a_k$. In addition, also the cavity frequency acquires shifts due to the Kerr-type non-linearity of the SQUID loop.

5 On-Chip Quantum Optics Experiments

This chapter represents the core of this thesis and discusses the major results that have been obtained in our experiments over the course of the last ten months. Throughout the final part of this thesis, we will systematically explore the different regimes of circuit quantum electrodynamics that have been introduced theoretically in chapter 4. On-chip quantum optics experiments are presented in which we were able to investigate the interaction of matter and light down to the level of single quanta, ultimately reaching the limit where a superconducting qubit dispersively interacts with the pure vacuum fluctuations of the electromagnetic cavity field. Here, the presence of the virtual photons manifests itself as a small renormalization of the energy of the qubit in the form of the Lamb shift, which is observed in our experiments for the first time in a macroscopic solid-state system. The transition from the strong dispersive to the resonant strong limit is shown as a smooth, continuous overlap of cavity transmission and qubit spectroscopy data, in a region where the Lamb shift turns into the Vacuum Rabi splitting of the entangled cavity-qubit superposition states. Following the vacuum field measurements, the photon number is sequentially increased. In this regime, some interesting experiments will be presented that allow us to put the Lamb shift in a consistent picture and to resolve individual photon number states of the cavity [5]. Finally, the strong coupling of a superconducting qubit to a flux-tunable transmission line cavity is experimentally demonstrated. Section 5.5 discusses the first preliminary results from these experiments. The presented data have been obtained in the very final stage of this thesis and thus only hint at the vast number of possible experiments that might be done with this device in the future.
Chapter 5 is outlined as follows. First, the measurement setup including cryogenics, filtering and circuitry will be discussed. Section 5.2 presents the results from transmission measurements of four tunable resonator devices and characterizes them in terms of their tuning behavior and quality factors. The concepts of continuous and pulsed qubit spectroscopy are then discussed in section 5.3. A detailed, in-depth analysis of the main quantum optics experiments and the Lamb shift observation is given in the final two parts of this chapter, where we also demonstrate the strong coupling of a superconducting qubit to a tunable resonator.

5.1 The Setup

In this section, the measurement setup, that was used and adapted for the experiments presented throughout this thesis, is discussed. The results described in this chapter were in fact obtained from measurements in two different, although similar setups. The measurements of the two-qubit device discussed in section 5.4 were carried out in a setup that has been developed prior

to this thesis [106]. This setup already allowed for a number of successful experiments [88, 107] and was ready to use from the start, for which the author would like to express his gratitude. The implementation of this setup will not be described here and is presented in detail in Ref. [106].
All other experiments that included tunable superconducting cavities were performed in a second, neighboring setup in a different cryostat. A significant amount of time for this thesis was invested in optimizing the circuitry, installing new filtering, setting up new lines and getting the setup ready for qubit experiments. The remainder of this section will focus on describing this setup.

Cryogenics

The experiments presented in this thesis have been exclusively conducted at ultra-low temperatures down to a few tens of mK above absolute zero. Such low temperatures are a stringent requirement for the observation of coherent quantum-mechanical effects in solid-state circuits. In section 2.1, it was shown that energy dissipation must be suppressed for a circuit to behave quantum-mechanically and to preserve its quantum coherence. Hence, as discussed throughout this thesis, only superconducting materials such as Nb or Al are used in the circuit QED architecture, which in turn means operating below the corresponding critical temperatures of T_c[Nb] $\sim$ 9.2K and T_c[Al] $\sim$ 1.2K, respectively. Furthermore, the need for ultra-low temperatures is also expressed by the relevant energy scales in our system. Superconducting qubits typically have transition frequencies on the order of 10 GHz corresponding to temperatures of $k_B T \sim$ 500 mK. Above these temperatures, thermal excitations would induce qubit transitions and completely destroy any coherent effects. To obtain base temperatures of about 15 mK, two dilution refrigerators are operated in the Quantum Device Lab at ETH Zurich, a *Kelvinox* 400 μW dilution cryostat from *Oxford Instruments* and a novel pulse-tube cooled dilution refrigerator [108, 109, 110] developed by *Vericold Technologies*. This section gives a description of the latter one. In part due to the surging market prices for liquid He, this new type of cryostat has become quite popular over the course of the last year or so, in particular among groups in the circuit QED community.

The operation of a cryogenic refrigeration system is based on a closed-loop Helium expansion cycle, as explained in detail in Ref. [111]. The dilution of liquid ^{3}He into liquid ^{4}He is currently the only method known to produce temperatures in the millikelvin regime in a continuous and stable way. In a conventional dilution refrigerator, the necessary precooling of the circulating ^{3}He/^{4}He mixture is accomplished by a dewar filled with liquid helium (sometimes also nitrogen). In addition to precooling from room temperature to 4.2 K, this helium bath also acts as a thermal radiation shield and cools the returning He in the cycle and helps to condense it [111]. Note that such a ^{4}He-filled dewar does not realize a closed cycle and must therefore be refilled periodically in continuous operation mode. A number of alternatives for precooling, that do not require any cryogenic liquids, have recently been developed. These novel types of 'dry' dilution refrigerators rely on closed-cycle refrigerators, such as in the form of Gifford-McMahon refrigerators [112] or pulse tube cryocoolers [113, 108, 109], rather than on a ^{4}He bath to handle

Figure 5.1: The pulsed-tube cooled dilution refrigerator used in the experiments of this thesis: closed state with all thermal and outer vacuum shields (left) and 'undressed' interior (right)

the precooling.

The *Vericold* pulse-tube cooled dilution refrigerator has two separate cycles, a pre-cooling and a dilution cycle, and consists of five different temperature stages as indicated on the left-hand side of Fig. 5.2, where the estimated cooling powers of each stage are also shown on the right. The refrigerant gas used in both cycles is 99.999 % pure Helium. In contrast to conventional cryostats, the precooling of the ^{3}He/^{4}He mixture is achieved by a pulse-tube cooler (PTC) rather than by a helium bath [108, 109]. In that way, the *Vericold* system does not require the use of any external cryogens, in particular liquid helium, for operation. This in turn supersedes periodic filling of the cryostat and allows using a simple vacuum can instead of a He dewar. The PTC used in our dilution refrigerator is a two-stage cryocooler whose first stage reaches a loaded temperature of $\sim$ 70K while the second stage reaches about 4K, as also indicated in Fig. 5.2. The circulating ^{3,4}He gas is first purified in a charcoal trap which is thermally anchored at the first stage of the PTC and is then pre-cooled in a heat exchanger at the second stage of the PTC to about 4 K. For more details on the construction and operation of dry refrigerators see Refs. [113], [109] and [110].

In the *Vericold* system, full automated cooldowns are possible in which pre-cooling and condensing are handled automatically by the software. In a typical cooldown, two steps can be distinguished. First, the 700 mK, 100 mK and the base stages are pre-cooled by the dilution unit via the mixture in the precooling cycle, while the 70 K and 4 K stages are cooled by the PTC. The pre-cooling cycle is controlled by the temperature on the base plate. Once a value of 12 K is reached, the He mixture is recovered from the pre-cooling cycle back into the external mixture tank and consequently directed into the condensing cycle. From this point on, the system is

in condensing mode and the base plate ultimately reaches a temperature of ∼15 mK. Almost all valves in the refrigerator system are software-controlled, the major exceptions being the two mixture tank valves. Pictures of the *Vericold* dilution refrigerator in its 'dressed' (with thermal and outer vacuum shields) and in its 'undressed' state are shown in Fig. 5.1.

Filtering and Circuitry

As discussed throughout this thesis, the relevant energy scale of the coupled qubit-cavity system is set in the microwave regime, where we are typically dealing with frequencies in the range of 1 to 10 GHz. To manipulate, control and readout the state of the system, classical highly phase coherent microwave signals are required which allow us to reveal the quantized nature of our devices. In addition, probing the matter-light interaction of a solid-state system down to the single and ultimately the zero photon limit requires signals of extremely low powers which can only be generated, modulated and resolved by careful filtering, amplification and attenuation/isolation. The use of cryogenic temperatures down to 15 mK effectively eliminates thermal excitations due to phonons entering the system from room temperature. However, the coaxial cables used for transmitting and extracting information from the sample go down from room temperature and thus they will also inevitably carry thermal photons to the sample. To effectively suppress this thermal noise source, the lines have to be strongly attenuated and isolated, with each component of the circuit properly thermalized at the relevant temperature stage of the cryostat.
The implemented microwave setup used for measuring all devices with tunable cavities is depicted in Fig. 5.2. In many aspects, this setup is identical to the one presented in [106], which was used for the Lamb shift measurements in section 5.4. We will thus restrict ourselves here to a rough description of the newly implemented setup rather than an exhaustive discussion of the individual components. In principle, three different parts can be distinguished in the setup of Fig. 5.2: (i) The signal synthesis part in which the required microwave signals are generated and modulated before entering the cryostat, (ii) the microwave circuit at the different temperature stages that attenuates the signals and isolates the sample from thermal noise and (iii) the amplification and down-conversion part.
For the generation of the RF microwave signals, a *Rhode & Schwarz* SMR 40 signal generator with an operating range of 10 MHz to 40 GHz was used, while for the local oscillator (LO) unit we employed an *Agilent* E8257D signal generator with a range of 250 kHz to 20 GHz (upper left-hand corner in Fig. 5.2). All microwave sources are phase coherent and phase locked. Note that the spectroscopy generator (upper left corner of Fig. 5.2) is illustrated in grey since it was not required, respectively, not yet implemented in the setup up to this stage of the tunable cavity experiments. Two 20 dB microwave attenuators are directly connected to the output of the RF generator, followed by a DC block so that the power of the signal is already strongly reduced before entering the dilution refrigerator. Once inside, the signal is further attenuated and thermalized at the 4 K, 100 mK and the base temperature stages by 50 dB in total. Typically, the coaxial cables themselves exhibit some frequency-dependent attenuation depending on their length and material properties. Here, we use two different types of cables, stainless steel cables (low thermal conductivity, strong signal attenuation) as well as Copper

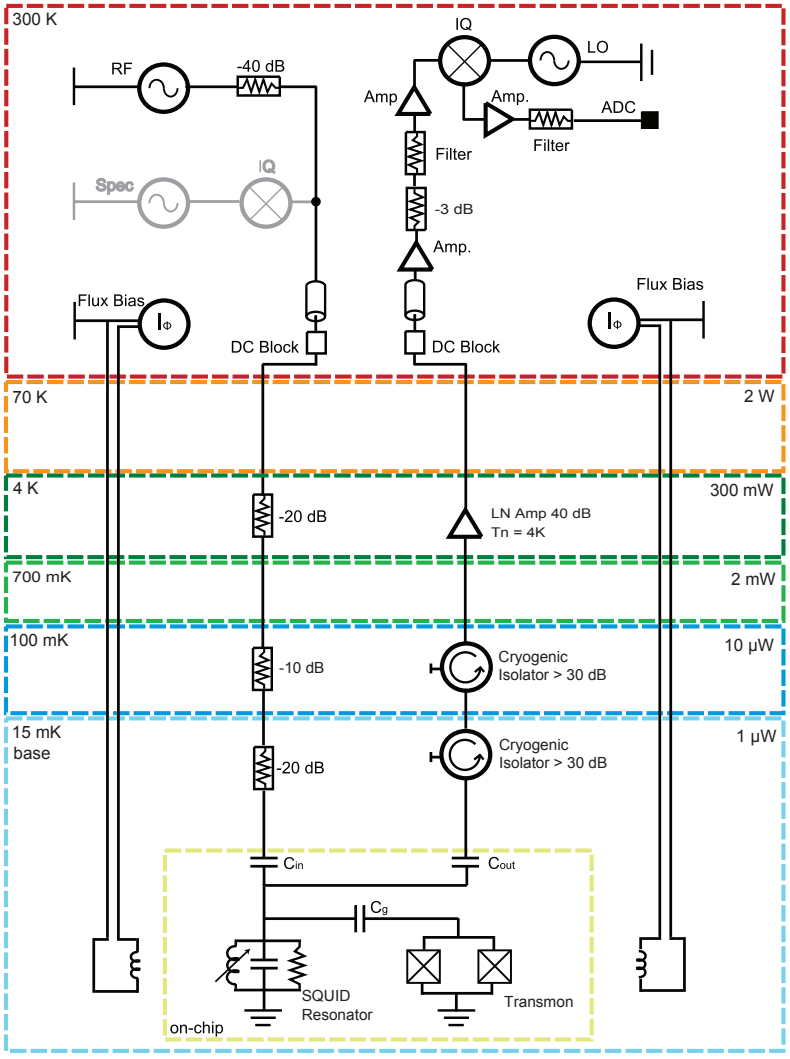

Figure 5.2: Implemented setup and circuitry in the pulse-tube cooled dilution refrigerator. The different temperature stages and estimated cooling powers are indicated in the right- and left-hand corners, respectively. A detailed discussion of the individual components is given in the text.

cables (high thermal conductivity, little attenuation). In this setup, the cable attenuation was estimated at roughly 18 dB at 5 GHz on the whole (upward and downward lines combined). In total, the signal at the output of the RF generator is attenuated by more than 100 dB before arriving at the input capacitor of the resonator. Note that the choice of the attenuator positions in the refrigerator is contrained by the relevant cooling powers at each stage (indicated on the left-hand side in Fig. 5.2). While the input side naturally suppresses thermal photons due to the strong attenuation that is required for the low powers at the sample level, any excessive attenuation on the output lines would absorb the signals transmitted through the sample and strongly reduce the signal to noise ratio. To this end, two cryogenic isolators from *Pamtech* (model CWJ1019) with a frequency range of 4 to 12 GHz are used instead of regular attenuators. Each of them is characterized by a very low (measured) attenuation in one direction ($<$0.6 dB) and very strong attenuation in the opposite one ($>$ 30 dB). In that way, the signals from the sample are transmitted nearly without loss while all thermal photons, travelling down the lines from the warmer stages, are effectively absorbed. Having passed the isolators, the signal is subsequently amplified at the 4 K stage by an ultra-low noise amplifier with a noise temperature of $T_n = 4$ K and 40 dB gain (manufactured at *Caltech*). Back at room temperature, the signal passes another DC block and is further amplified by two *Miteq* amplifiers and filtered in a 4.25 - 10 GHz band pass filter from *Mini-Circuits*. In the following, the signal is down-converted and mixed with the LO signal (offset by 10 MHz from the original RF signal) using an IQ mixer (*Marki* M07079). Before entering the data acquisition card for post-processing, the signal gets amplified further by a *Mini-Circuits* ZFL 500 low noise amplifier (24 dB gain, 1 to 500 MHz operating range) and filtered by another band pass. In total, this setup allows for ultra-low power GHz signals at the sample level, strong isolation from thermal photon noise and a signal to noise ratio high enough to observe the quantum nature of our devices.
To manipulate the transition frequencies of both the qubit and the cavity, two coils wound with superconducting Nb-Ti alloy wires are installed underneath the chip directly in the Copper sample holder. A small coil with an inner loop diameter of $d = 3$ mm is centered below the qubit and a larger one with $d = 11$ mm is positioned so that its center axis is aligned with the middle of the whole chip. The chassis is made out of *Torlon* polyamide-imide, an ultra-high strength thermoplastic. The coils are either current or voltage biased using a *Yokogawa* 7561 programmable DC source to generate a stable flux bias.

5.2 Superconducting Tunable Cavities

In total, 30 different tunable transmission line resonators have been designed in the framework of this thesis (see section 3.2), four of which have been measured in the setup discussed above with one successfully coupled to a superconducting transmon qubit. In summary, all of the devices are in excellent agreement with the theory developed in chapter 3 and had parameters remarkably close to the actual design. The two most important quantities of a tunable cavity are its total tuning range $\Delta_\nu = \nu_r(\Phi_0) - \nu_r(\Phi_0/2)$ and the behavior of its quality factor under flux bias $Q(\Phi)$. This section focuses on the results from the measurements of the bare resonators which have not been coupled to a qubit. The coupled transmon-cavity system will be discussed separately

Mask ID	ℓ [μm]	C_κ	I_{c1} [μA]	I_{c2} [μA]	d	loop size
H 1	7600	1+2 finger - 74 μm	2.20	1.95	6.0 %	30 μm^2
J 1	7800	1+2 finger - 74 μm	2.32	2.05	6.2 %	30 μm^2
L 1	13200	1+1 finger - 74 μm	2.35	2.03	7.5 %	30 μm^2
L 3	13200	1+1 finger - 74 μm	2.00*	2.6*	13.0 %	30 μm^2

Table 5.1: Designed and measured parameters of the four realized SQUID-cavity devices. Here, d denotes the junction asymmetry, I_{c1} and I_{c2} the critical currents extracted from fits and C_k the symmetric coupling capacitances. All of the devices are coupled by finger capacitances with a length of 74 μm per finger. (* Designed values. This device is still being analyzed.)

in section 5.5.

5.2.1 Tuning Range

The total tuning range of a superconducting transmission line resonator incorporating a SQUID loop is ultimately determined by how symmetrically the two Josephson junctions can be fabricated. As shown in detail in section 3.2, the degree of asymmetry of the SQUID junctions can be effectively used as a design parameter that sets both the absolute tuning range as well as the flux noise sensitivity of the cavity. Perfectly symmetric junctions yield the maximum tuning range $\Delta_\nu = \nu_r(n\Phi_0)$, while devices with asymmetric junctions are less sensitive to magnetic flux noise. The behavior of the resonance frequency under flux bias can be modeled either numerically using the ABCD matrix formalism or by means of a mapped LCR oscillator model (see section 3.2). There, the resonance frequency was derived as

$$\omega_0(\Phi) = \frac{\omega_r}{1 + \frac{L_s(\Phi)}{L}} \tag{5.1}$$

with ω_r denoting the resonance frequency of the equivalent cavity without SQUID. Here, the linear flux-tunable SQUID inductance is given by

$$L_s(\Phi) = \frac{\Phi_0}{2\pi}\left[(I_{c1} - I_{c2})^2 + 4I_{c1}I_{c2}\cos^2\left(\pi\frac{\Phi}{\Phi_0}\right)\right]^{-1/2}. \tag{5.2}$$

To test the models and see how accurate the fabrication and design processes are, four different tunable resonators have been fabricated and systematically measured. The parameters of the different resonators are summarized in Tab. 5.1. To experimentally verify the tuning behavior, each of the four test resonators was measured in transmission and sweeped over several flux periods using the setup presented above. Here, the coils for generating the flux are voltage biased over a series combination of two RC filters. To avoid non-linear effects and keep the current at the SQUID position below its critical current, the input power of the microwave signals P_{rf} was set in the approximate single photon range, corresponding to -30 to -35 dBm at the RF generator output and roughly -140 dBm to -145 dBm at the input capacitance of the

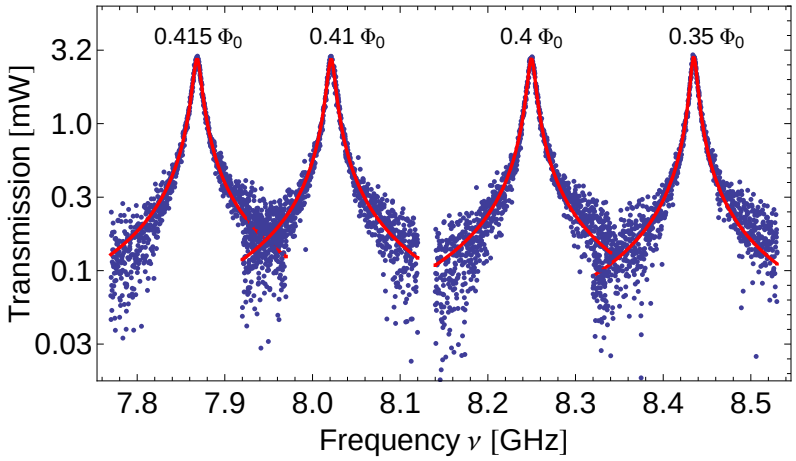

Figure 5.3: Transmission spectra and Lorentzian fits at different flux for device J1 (see Tab. 5.1 for sample parameters).

resonator [1]. Since all resonators are characterized by low quality factors ($Q \sim 1000-3000$), the peaks in the transmission are broad and the microwave signals get transmitted nearly without loss, i.e. the resonators are over-coupled [92]. Thus only little averaging ($\sim$ factor 500) and large frequency step sizes ($\sim$ 0.5 - 3 MHz) are required for these sweeps. The transmission spectrum at each flux bias step was measured, recorded and fitted to a Lorentzian, which yields both the frequency of maximum transmission as well as the quality factor. Typical transmission spectra and Lorentzian fits at different flux biases are depicted in Fig. 5.3 for device J1. The tuning behavior is clearly demonstrated as the resonances shift by more than 600 MHz under a small flux variation of $0.35\Phi_0 \leq \Phi \leq 0.415\Phi_0$ close to half a flux quantum. Fig. 5.4 shows the resonance frequencies extracted from Lorentzian fits for devices L1 and J1 over one flux period each. Here, the solid lines are fits to the theoretical expression (5.1) from which we are able to determine the critical currents and the junction asymmetry, see Tab 5.1. The devices realize tuning ranges of several GHz, by far exceeding those reported in Refs. [11, 90], where the maximum measured range was 700 MHz. The tuning curves $\omega_r(\Phi)$ exhibit broad maxima and narrow, pronounced minima with total tuning ranges of $\Delta_\nu(\mathrm{H1}) = 2.66$ GHz and $\Delta_\nu(\mathrm{L1}) = 900$ MHz [2].

5.2.2 Quality Factors

The total quality factor of a transmission line resonator is given by the parallel combination of the internal and external quality factors (see chapter 3)

$$\frac{1}{Q_L} = \frac{1}{Q_{\mathrm{int}}} + \frac{1}{Q_{\mathrm{ex}}} \tag{5.3}$$

[1] See also the discussion on the operating constraints in chapter 3.
[2] This value is most likely higher, since the true minimum cannot be identified due to the strong degrading of the quality factor in this case (see also section 5.2.2).

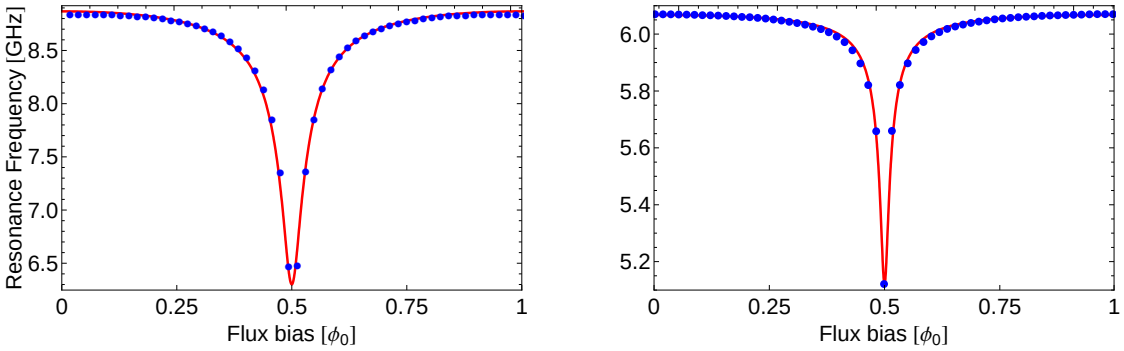

Figure 5.4: Extracted resonance frequencies for devices H1 and L1 as a function of applied flux bias.

where we had for the external quality factor in case of symmetric coupling

$$Q_{\text{ex}} = \frac{n\pi}{4Z_0}\left(\frac{1}{C_\kappa^2 R_L \omega_n^2} + R_L\right) . \tag{5.4}$$

For large coupling capacitances, Q_{ex} becomes small and the loaded quality factor is dominated by the external contribution $Q_L \sim Q_{\text{ex}}$. On the other hand, weak coupling to the input/output lines yields a large external quality factor and we have $Q_L \sim Q_{\text{int}}$. All of the measured tunable cavities are quite strongly over-coupled due to their comparably large coupling capacitances of a few fF (see Tab. 5.1). Thus it holds for the measured quality factor $Q_L \sim Q_{\text{ex}}$. In principle, one would expect an increase in quality factor for $\Phi \to \Phi_0/2$ as the resonance frequency reaches its minimum and all other parameters in (5.4) are constant. However, this expression does not account for the non-linearity and the bias current dependence of the SQUID. This effect translates to an inhomogeneous broadening of the resonances which can become significant at points of high noise sensitivity. This broadening is a result of the shifts of the resonance frequency that are generated by the SQUID non-linearity. In section 2.4.2, we found for the Taylor expansion of the non-linear resonance frequency of the SQUID loop

$$\begin{aligned} \omega_s &= \frac{1}{\sqrt{(L_{s0}(\Phi_{\text{ext}}) + A_3(\Phi_{\text{ext}})I^2)C_s}} \\ &= \omega_{s0} - \frac{1}{2!}A_3 I^2 \frac{1}{2\sqrt{L_{S0}^3 C_s}} + \frac{1}{3!}A_3^2 I^4 \frac{3}{4\sqrt{L_{S0}^5 C_s^3}} - \dots . \end{aligned} \tag{5.5}$$

and equivalently for the flux-dependent inductance

$$\begin{aligned} L_s(\Phi) &= \frac{\Phi_0}{2\pi I_c(\Phi)}\left[1 + \frac{1}{2!}\left(\frac{I}{I_c(\Phi)}\right)^2 + \frac{1}{4!}9\left(\frac{I}{I_c(\Phi)}\right)^4 + \dots\right] \\ &= \frac{\Phi_0}{2\pi I_c(\Phi)} + A_3 I^2 + 9A_5 I^4 + \dots . \end{aligned} \tag{5.6}$$

Here, we see that fluctuations in the current I result in fluctuating shifts of the resonance frequency of the SQUID circuit and its inductance, which in turn also causes the resonance fre-

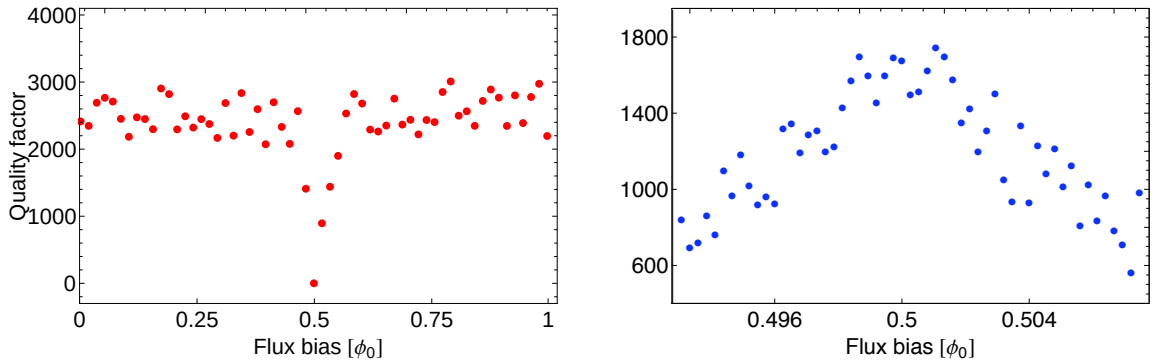

Figure 5.5: Extracted quality factors as a function of applied flux bias for device L1 over a whole flux period (left) and device H1 around half a flux quantum (right).

quency of the total cavity-SQUID system to fluctuate. This leads to inhomogeneous broadening of the resonances and thus an increase of the cavity linewidth, i.e. a decrease of the quality factor. More rigorously, the corresponding decrease in quality factor can also be expressed as [11]

$$Q_{\text{inh}} = \left[\frac{2\omega_0(\Phi)}{\pi R_L(1+2\frac{L_s(\Phi)}{L})}\right]^{-2} \frac{16\pi I_c^3(\Phi)}{\Phi_0} \frac{1}{\sqrt{\overline{\delta E^2}}} \tag{5.7}$$

where symmetric junctions have been assumed. Here, $\overline{\delta E^2}$ are the average energy fluctuations due to the fluctuating number of photons $\overline{n^2 - \overline{n}^2}$ inside the resonator, which is equivalent to a fluctuating current (see section 3.2.4). (5.7) explicitly shows that the total quality factor

$$\frac{1}{Q_L} = \frac{1}{Q_{\text{int}}} + \frac{1}{Q_{\text{ex}}} + \frac{1}{Q_{\text{inh}}} \tag{5.8}$$

reaches a sharp minimum at $\Phi_0/2$ where $I_c \to 0$ for symmetric Josephson junctions. Apparently, a certain degree of asymmetry helps in reducing this strong decrease.

The degrading of the quality factor is indeed observed in our measurements. The extracted quality factors for device $L1$ are depicted in Fig. 5.5a over one flux period. Here, Q_L exhibits a sharp decrease around $\Phi_0/2$ down from its maximum value $Q_{\text{max}} \sim 2900$ to effectively zero. At $\Phi_0/2$, the critical current reaches a minimum and thus small fluctuations in the ac current at the SQUID position due to thermal noise will have a strong effect.

This degrading of the quality factor can, however, be circumvented due to the fact that the overall quality factor decrease depends on the actual parameters of the cavity. If the resonator is sufficiently over-coupled with large C_κ and in addition has a moderate degree of junction asymmetry, it is in fact possible that the decrease in Q predicted by (5.5) and (5.7) can be compensated by the increase due to (5.4) around $\Phi_0/2$. Indeed in Fig. 5.5b a flux sweep in the vicinity of $\Phi_0/2$ of the highly over-coupled device H1 shows a strong increase of the quality factor by a factor of 3 around the minimum, consistent with the above discussion. The possibilities arising from such a suppression of the Q degrading could help achieve better control over the quality factor and should be further systematically investigated in terms of a parameter design study.

5.3 Qubit Spectroscopy and Readout

The dispersive regime of circuit QED allows for a quantum non-demolition measurement and readout of the qubit state and its transition frequency via the dispersive cavity frequency shifts discussed in chapter 4. The qubit-state dependent shift of the resonances in the cavity transmission forms the basis of superconducting qubit spectroscopy. In the experiments presented here, two different types of spectroscopic measurements have been employed, a continuous version where the cavity is populated with photons while the qubit transition is probed and a pulsed version where the cavity mode remains unpopulated.

5.3.1 Continuous Spectroscopy

Under microwave irradiation, a superconducting coplanar waveguide cavity essentially behaves like a driven harmonic oscillator and thus the corresponding transmission power spectrum exhibits a Lorentzian line shape of the general form (see chapter 3)

$$P(\nu) = P_0 \frac{\delta\nu_0^2}{(\nu-\nu_0)^2+\delta\nu_0^2} \tag{5.9}$$

where ν is the frequency of the microwaves passing through the cavity, ν_0 the resonance frequency, $\delta\nu_0$ the cavity linewidth (half width at half maximum) and P_0 the input power. Using the definition of the quality factor $Q = \nu_0/2\delta\nu_0$, the transmission spectrum reads

$$P(\nu) = \frac{P_0}{4Q^2} \frac{1}{\left(\frac{\nu}{\nu_0}-1\right)^2 + \frac{1}{4}\left(\frac{1}{Q}\right)^2} . \tag{5.10}$$

In addition to the change in amplitude (5.9), the waves also acquire a phase shift when passing the cavity, just like optical photons do when being transmitted or reflected by an optical medium. The general form of this phase shift is given by

$$\delta(\nu) = \arctan\left(\frac{1}{\delta\nu_0}(\nu-\nu_0)\right) . \tag{5.11}$$

Thus far off-resonant photons $|\nu-\nu_0| \gg 1$ will acquire a phase shift close to $\pm\pi/2$ whereas resonant or near-resonant photons match the resonance condition of the cavity and therefore have a vanishing phase shift.
The presence of a qubit inside the cavity results in a change of the resonance frequency ν_0. In the dispersive regime $\Delta \gg g$ where qubit and resonator are essentially decoupled, the qubit-cavity interaction manifests itself in the form of frequency shifts as described by the dispersive circuit QED Hamiltonian (section 4.1.1)

$$H_{\text{eff}} = \frac{\hbar}{2}\left(\omega_a + \frac{g^2}{\Delta}\right)\sigma_z + \hbar\left(\omega_0 + \frac{g^2}{\Delta}\sigma_z\right)a^\dagger a . \tag{5.12}$$

As can be seen, the bare qubit frequency ω_a is shifted by $\chi = g^2/\Delta$ due to the interaction with

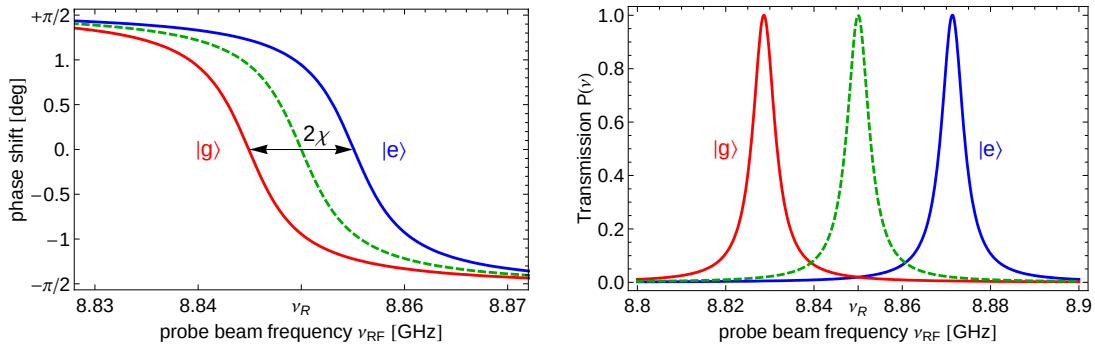

Figure 5.6: (a) State-dependent phase shift as a function of probe beam frequency. (b) Qubit state-dependence of transmitted amplitude with excited state (blue), ground state (red) and unshifted peaks (dashed green) calculated for typical qubit and resonator parameters.

the vacuum field fluctuations $\langle a^\dagger a \rangle = 0$, i.e. it is the Lamb-shifted, whereas the cavity resonance frequency ω_0 acquires a shift $\chi\sigma_z$ that depends on the state of the qubit $\langle \sigma_z \rangle = \pm 1$. Hence the qubit state can be inferred from a quantum non-demolition measurement of the frequency shift that an incident wave experiences when passing the cavity (see also section 4.1). Using the cavity decay rate $\kappa = 4\pi\delta\nu_0$ and the shifted resonance frequency $\tilde{\nu}_0 = \nu_0 \pm g^2/\Delta$, the general phase shift (5.11) is rewritten as

$$\delta(\nu) = \arctan\left(\frac{4\pi}{\kappa}(\nu - \nu_0) \pm \frac{2g^2}{\kappa\Delta}\right) . \tag{5.13}$$

For near-resonant photons $\nu \sim \nu_0$ it then follows

$$\delta\nu_\pm \approx \pm \arctan\left(\frac{2g^2}{\kappa\Delta}\right) , \tag{5.14}$$

i.e. the sign of the phase shift of a wave passing the cavity depends on the state of the qubit. Hence, monitoring the phase and transmission spectrum of a probe microwave beam of constant frequency ν_{rf} and power P_{rf} represents an effective method for a readout of the qubit state. As the peak in the cavity transmission spectrum shifts by $\pm g^2/\Delta$ depending on the state of the qubit, both the phase shift as well as the amplitude, i.e. the number of transmitted photons of the probe beam, change. Note that this measurement is quantum non-demolition as qubit and cavity states are essentially decoupled in the dispersive regime. This is discussed explicitly in section 4.1.3, where the QND character of the dispersive readout was established from the fact that the qubit operator σ_z commutes with the total effective Hamiltonian $[H_{\mathrm{eff}}, \sigma_z] = 0$ in this regime.

The phase shift as a function of the probe beam frequency is depicted in Fig. 5.6a for typical qubit and cavity parameters. The dependence on the qubit state is clearly visible in the vicinity of the resonance frequency $\tilde{\nu}_0$. For a given constant probe beam frequency $\nu_{\mathrm{rf}} \sim \nu_0$, the phase shift for a certain qubit state can be inferred from the intersections with the $\delta\nu_\pm$ curves. Furthermore, Fig. 5.6b shows the qubit-dependent shift in the transmission spectrum of the cavity. So how can these phase and resonance frequency shifts be used for spectrosopic measurements

of the qubit?
Assuming the qubit to be initially in its ground state with no driving pulses applied, the constant probe beam ν_{rf} will experience a constant phase shift $\delta\nu_-$. If however a spectroscopic driving beam ν_s is applied in addition to the constant probe beam ν_{rf}, the qubit's transition $|e/g\rangle \rightarrow |g/e\rangle$ will be driven for $\nu_s = \nu_a$. Thus according to Eq. (5.14) also the phase shift of the probe beam ν_{rf} changes sign. This is the underlying principle of superconducting qubit spectroscopy. Sweeping ν_s through resonance with the qubit, the transition frequency can be sensitively measured by means of monitoring the phase shift of the probe beam while the spectroscopic tone is swept through. When ν_s reaches ν_a, the qubit is excited and the phase shift changes sign at exactly $\nu_s = \nu_a$. The shape of this change in $\delta\nu$ is Lorentzian as given by (5.9), where this time $\delta\nu_0$ is the qubit linewidth and $\nu_0 = \nu_a$ the qubit transition frequency. The Lorentzian 'power' P_0 here is directly related to the excited state population of the qubit [1, 4, 84]

$$P_\uparrow = 1 - P_\downarrow = \frac{1}{2}\frac{n_s\omega_{\mathrm{vac}}^2 T_1 T_2}{1 + n_s\omega_{\mathrm{vac}}^2 T_1 T_2} \tag{5.15}$$

where $T_{1,2}$ are the energy relaxation and dephasing times, respectively, n_s the average number of spectroscopy photons and $\omega_{\mathrm{vac}} = 2g$ the vacuum Rabi frequency. The qubit linewidth is given by the inverse of the 'broadened' T_2 time

$$2\pi\delta\nu_a = \frac{1}{T_2'} = \left(\frac{1}{T_2^2} + n_s\omega_{\mathrm{vac}}^2\frac{T_1}{T_2}\right)^{1/2} \tag{5.16}$$

which in the unbroadened case of vanishing n_s reduces to the inverse of the pure dephasing time $\delta\nu_a = 1/2\pi T_2$. Note that this readout and spectroscopy scheme only works in the dispersive regime. On resonance $\Delta \rightarrow 0$, the probe beam itself is driving the qubit and causes it to flip back and forth between ground and excited state. Therefore also the phase shift δ_ν of the probe beam changes sign. On resonance $\nu_0 = \nu_a$, all excitations in the system become equally shared bectween qubit and cavity and there are no separate transitions or energy levels anymore.
It is important to note that in the continuous spectroscopy scheme the cavity mode is populated while the qubit transition is probed. The probe beam $(\nu_{\mathrm{rf}}, P_{\mathrm{rf}})$ and the spectroscopy tone ν_s are applied simultaneously. Since the probe beam frequency is in the vicinity of the cavity resonance $\nu_{\mathrm{rf}} \approx \nu_r$, it populates the resonator mode with photons to an extent depending on the actual input power P_{rf} that is applied. Of course, the probe beam power P_{rf} can be chosen low enough to be in the zero photon limit $\overline{n} \sim 0$. However, this in turn drastically reduces the signal to noise ratio and implies a lot more averaging, making the overall spectroscopy much slower. More importantly though, the qubit transition is in general ac-Stark shifted (section 4.1.3) and thus proportional to the number of photons n in the cavity mode. Fluctuations in n then translate directly to fluctuations in ω_a which in turn leads to dephasing effects in the continuous spectroscopy scheme [4, 104].

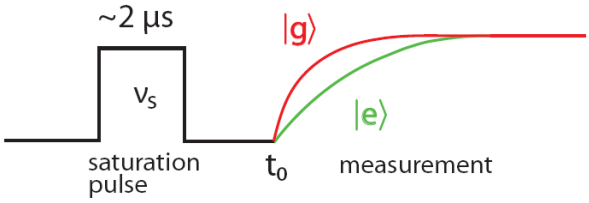

Figure 5.7: Schematic pulse sequence in a pulsed spectroscopy measurement of the qubit state and transition frequency.

5.3.2 Pulsed Qubit Spectroscopy

In a continuous spectroscopy scheme, the probe beam of power P_{rf} and frequency ν_{rf} effectively populates the cavity during the time the qubit transition is probed by the spectroscopy tone ν_s. Naturally, this implies Stark shifts and thus also photon number splitting of the qubit peak [5, 104], see also the results presented in section 5.4.2. This leads to dephasing as the qubit frequency is now sensitive to fluctuations in the photon number. These problems can be effectively circumvented by means of using a pulsed rather than a continuous spectroscopy scheme.

Pulsed qubit spectroscopy represents a quite recent development, in which the two tones ν_{rf} and ν_s are separated in time so that the cavity is not populated while the spectroscopy drive is swept. The corresponding pulse sequence is schematically depicted in Fig. 5.7. The qubit is assumed to be initially in its ground state $|g\rangle$. In the first step, the probe beam ν_{rf} is sweeped through to determine the resonance frequency of the cavity $\nu_r(|g\rangle)$ when the qubit is in its ground state. This represents a calibration in which we determine what the resonator response looks like when the qubit is not excited (red curve in Fig. 5.7). In the second step, a rectangular saturation pulse of frequency ν_s and fixed duration of about 2 μs is applied to probe the qubit transition. This long microwave pulse prepares a fully mixed qubit state. If ν_s matches the qubit frequency ν_a, the qubit is excited $|g\rangle \rightarrow |e\rangle$, otherwise the qubit stays in the ground state. At a time $t_0 \sim 5$ ns after the saturation pulse[3] the probe beam of fixed frequency $\nu_{\mathrm{rf}} = \nu_r(|g\rangle)$ is applied and the transmission of the resonator is measured. If the saturation pulse frequency ν_s was not in vicinity of the qubit transition ν_a, the qubit remained in the ground state and the resonator response will be the same as in the calibration. If, however, ν_s was on or near-resonant with ν_a, the qubit has been excited and thus also the resonator frequency shifts away from $\nu_r(|g\rangle)$ to $\nu_r(|e\rangle)$. In that case, the probe beam frequency no longer matches the cavity resonance and hence the response is different from the calibration (green curve in Fig. 5.7). To see how 'different' the transmission is, the measured response is subtracted off the calibration response and the area under the resulting curve is integrated. A small or vanishing area says that the qubit was not excited by the saturation pulse ν_s, while large areas show that ν_s was in the vicinity of ν_a or matched. This whole procedure is now repeated for each step in the spectroscopy frequency

[3] The actual time between saturation and measurement pulse is chosen such that the signals can be well separated and is thus ultimately determined by technical specifications of the equipment used.

sweep over the chosen intervall.
It should be highlighted here that the cavity is not populated at all times when probing the qubit transition. No cavity-resonant probe beam is applied during the time the spectroscopy pulse is applied and thus also no resonant photons are present. The pulsed qubit spectroscopy scheme makes it possible to measure the qubit's frequency while it is solely interacting with the vacuum field and has ultimately allowed us to measure the Lamb shift.

5.4 Resolving Vacuum Fluctuations via the Circuit QED Lamb Shift

The discussion of circuit quantum electrodynamics in chapter 4 has shown that the coherent interaction between a superconducting qubit and a transmission line cavity can be investigated in two qualitatively different regimes. In the resonant limit, qubit and cavity can freely exchange energy and the two systems lose their individual character. In the dispersive limit of large detunings between qubit and cavity field, the interaction manifests itself only in the form of frequency shifts present in the decoupled Jaynes-Cummings Hamiltonian (see section 4.1.3). This limit yields some rich physics and has allowed for a number of hallmark experiments such as the detection of the ac Stark shift or the resolution of individual photon number states of a cavity, see Refs. [2, 4, 5] and section 5.4.2. In the light of these developments, the observation of the dispersive interaction in the form of the Lamb shift seems somewhat overdue as it represents the only term in the circuit QED Hamiltonian that has not been identified so far. In the framework of quantum field theory, the Lamb shift represents a manifestation of the interaction of the qubit with the virtual photons inside the cavity and it is closely related to other important observable effects of the quantized vacuum field, such as the Casimir forces [114], the vacuum Rabi mode splitting [22] or spontaneous emission and the Purcell effect [115, 116]. Historically, the observation of the Lamb shift in a Hydrogen atom [20] and its correct theoretical calculation [117] marked the birth of quantum electrodynamics and the theory of renormalization [118]. In the following, we present the first experimental observation of the Lamb shift in a solid state system by making use of the strong dispersive coupling of an individual quantum two-level system (qubit) to the vacuum radiation field contained in a high quality factor transmission line resonator.

5.4.1 Lamb Shift Observation and Vacuum Rabi Splitting

The detection of the Lamb shift and the observation of its detuning behavior can be entirely carried out using the spectroscopic concepts discussed in section 5.3. The dispersive readout in circuit QED systems has turned out to be a powerful tool for characterizing superconducting qubits and its quantum non-demolition nature represents an important aspect for future quantum information processing. Although the basic techniques of qubit spectroscopy are by now well-established and understood, a direct observation of the dispersive interaction with the vacuum photonic field poses a number of additional challenges:

- The coupling to the vacuum electromagnetic field is very weak in the dispersive regime

	$E_J^0/\hbar$	$E_C/\hbar$	$g_{\max}/2\pi$	$\nu_a^{\max}$
Qubit A	35.11 GHz	231.7 GHz	133 MHz	7.84 GHz
Qubit B	37.63 GHz	232.5 GHz	134 MHz	8.10 GHz

Table 5.2: Parameters of the two-qubit device used for the Lamb shift observation.

and leads only to small frequency shifts on the order of MHz.

- Unlike the ac Stark shift, the Lamb shift is always present and cannot be 'switched off' by simply reducing the photon population of the resonator. In other words, a pure, undressed qubit transition frequency does not exist and thus cannot be measured by any means.

- To make sure the cavity is in its vacuum state $\langle a^\dagger a\rangle = 0$ and to avoid any Stark shifts, measurements have to be carried out in the zero photon limit which requires a high degree of isolation and attenuation on input and output lines of the setup as well as very low probe beam powers to suppress thermal and coherent photons. Moreover, this also implies using pulsed rather than continuous qubit spectroscopy (see section 5.3).

Sample Characterization

The experiments that lead to the observation of the Lamb shift were carried out on a device consisting of two superconducting transmon qubits coupled to a high-quality transmission line cavity . Optical microscope pictures of the complete chip and a zoom on one of the two transmons are shown in Fig. 5.8 together with a simplified circuit diagram of our experimental setup. The device was fabricated in the clean room facilities at ETH Zurich using the techniques and methods discussed in detail in section 3.2.5 and Refs. [71, 92, 95]. The coplanar transmission line resonator is characterized by a length of $\ell = 9420\,\mu$m and symmetric input/output coupling capacitances of $C_\kappa \sim 9.5$ fF (1+2 fingers, 97 μm each). Transmission measurements with both qubits far detuned yielded a resonance frequency of $\nu_r = 6.441$ GHz and a quality factor of $Q = 4100$. The two transmon qubits were designed to have identical properties, which was achieved to a satisfying degree in fabrication. They are both operated deep in the transmon regime $E_J^{\max}/E_C \simeq 160$ with minimum anharmonicities of $\alpha = E_{01} - E_{12} \simeq 250\,$MHz (see also section 2.7). An overview of the parameters of the two qubits is given in Tab. 5.2. Here, the fundamental qubit parameters (E_J^0, E_C) were determined in independent continuous spectroscopy measurements (see section 5.3.1). A detailed discussion of the determination of the qubit parameters and their dependence on the control variables is given below in 'Results and Discussion'. Note from Fig. 5.8 that both transmon qubits are connected to on-chip gate lines that allow us to locally drive the qubit transitions in a controlled way. In the experiments discussed here, these gate lines have been used to apply the spectroscopy pulses to the qubits. The design and underlying theoretical concepts of the gate lines are presented in detail in Ref. [119].

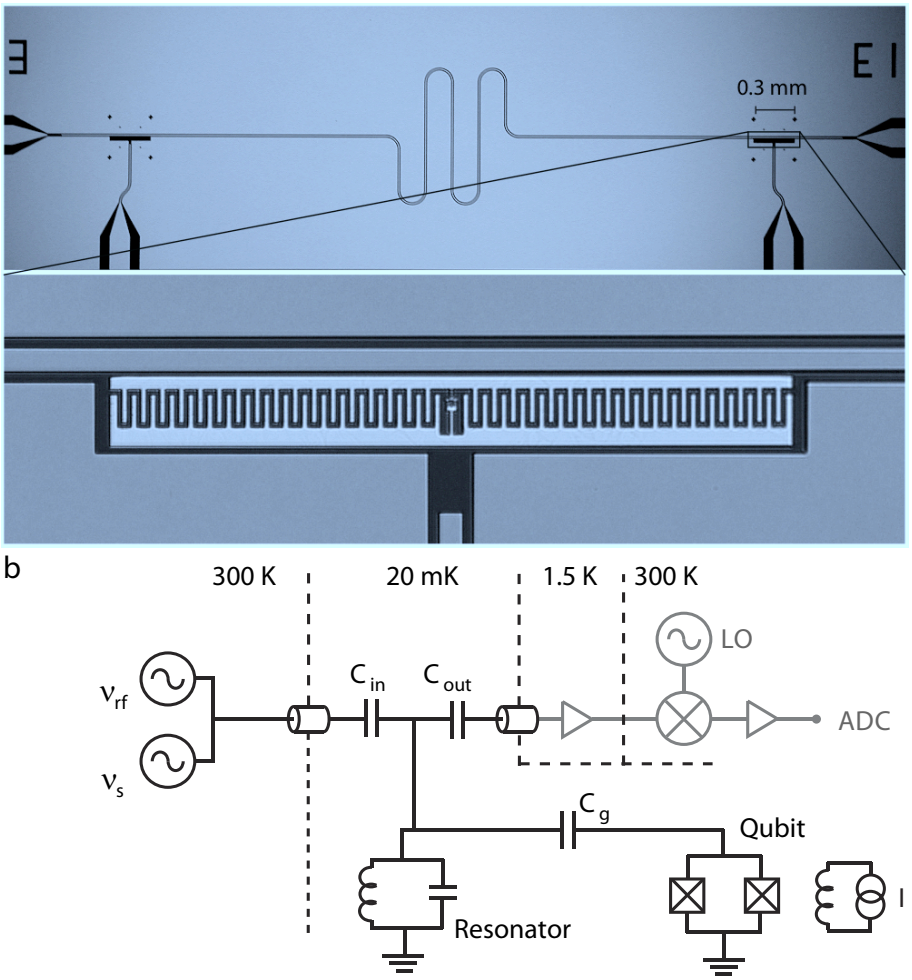

Figure 5.8: Sample and experimental setup. (a) Top, optical image of a superconducting coplanar waveguide resonator, equivalent to the one used in our experiments, with the transmon type superconducting qubit embedded at the position shown boxed. Bottom, magnified view of boxed area, showing the qubit with dimensions 300 $\times$ 30 μm^2 close to the center conductor. (b) Simplified circuit diagram of the set-up, similar to the one used in Ref. [2]. The qubit at temperature 20 mK is capacitively coupled to the radiation field contained in the resonator through C_g. The resonator, represented by a parallel LC circuit, is coupled to input and output transmission lines via the capacitors C_{in} and C_{out}. The qubit transition frequency is controlled via a current biased (I) coil generating a magnetic flux Φ threading the qubit loop. Microwave signal generators for populating the resonator with photons (ν_{rf}) and for exciting the qubit spectroscopically (ν_{s}) are shown. Using ultralow-noise amplifiers at 1.5 K and a mixer at 300 K, the transmitted microwave signal is down-converted with a local oscillator (LO) and digitized with an analog-to-digital converter (ADC) for measuring the qubit and photon states, see also detailed discussion in the text.

Local Flux Control

The possibility to fabricate devices with multiple qubits paves the way for a new generation of circuit QED experiments [3, 9]. However advantageous a two-qubit device might be, the Lamb shift observation becomes in fact a bit more challenging in such a system. Here, we are interested in probing the vacuum field interaction of a single, undisturbed qubit. Luckily, in these experiments we are in a position to effectively realize local qubit control, which allows us to adjust the transition frequencies of both qubits almost independently. In particular, we can tune the transition frequency of one qubit while the other is kept constant. For flux-biasing the transmons, two coils wound with superconducting Nb-Ti alloy wires have been installed underneath the chip in the Copper sample holder. A small coil of loop size $d = 3$ mm (inner diameter) is centered below qubit B and a larger one with $d = 11$ mm is positioned so that its center axis is aligned with the middle of the whole chip. As the two qubits are spatially separated on the chip by 4800 μm, the flux generated by the small coil can be used to locally control qubit B while having only a very small influence on qubit A. The flux from the large coil affects both qubits equally and can be used to tune either one of them. The two coils are voltage biased over series RC filters at room temperature and their coupling to each qubit can be described in terms of a matrix equation. The voltage biases and the fluxes at the two qubits are related by

$$\begin{pmatrix} \Phi_A \\ \Phi_B \end{pmatrix} - \begin{pmatrix} \Phi_A^{\text{off}} \\ \Phi_B^{\text{off}} \end{pmatrix} = \begin{pmatrix} A & B \\ C & D \end{pmatrix} \begin{pmatrix} V_L \\ V_S \end{pmatrix} \tag{5.17}$$

where $V_{L/S}$ denotes the bias voltage of the large/small coil in Volts, $\Phi_{A/B}$ the absolute flux at qubit A/B and $\Phi_{A/B}^{\text{off}}$ the offset in units of flux quanta Φ_0. The matrix elements are given by the inverse voltage periods, with $A = 1/V_{L,A}^0$, $B = 1/V_{S,A}^0$, $C = 1/V_{L,B}^0$ and $D = 1/V_{S,B}^0$.
To effectively realize a one qubit sample out of a two qubit one, qubit B is tuned to $\Phi_B = \Phi_0/2$ at all times during the experiments. This is achieved by dynamically compensating the flux from the large coil, which is used to control qubit A, via the local small coil. The corresponding compensation factors are easily calculated from the ratios of the matrix elements, i.e. $(-B/A)$ for compensating the small coil with the large one and $(-F/G)$ for the other way around. The actual compensation that keeps qubit B at $\Phi_0/2$ is then carried out using a simple *Labview* code. Following a careful determination of the various voltage periods for the two qubits, the matrix elements in (5.17) were calculated and used to keep qubit B at a constant flux bias $\Phi_B = \Phi_0/2$, far detuned from both the resonator and qubit A throughout the whole experiment. In that way, we can effectively turn a two-qubit device into a single one. Note that even if qubit B was not set to its minimum Josephson energy $E_J(\Phi_0/2)$, it would only lead to a *constant* renormalization of the resonator frequency and the transition of qubit A. Precise knowledge of qubit A's tuning behavior is a stringent requirement to be able to unambiguously identify the small frequency shifts we are looking for. Hence, both voltage period and offset of qubit A were measured carefully before each run by means of sweeping over two adjacent maxima $\nu_a(n\Phi_0)$.

Numerical Calculations of the Lamb shift

A pure, undressed qubit transition frequency does not exist as the vacuum field fluctuations are always present. Hence, the Lamb shift cannot be determined by simply doing spectroscopy on a dressed and (presumably) undressed qubit and comparing the two results, as is possible, for instance, in an ac Stark shift measurement. The only way to determine the Lamb shift from the measured data is by means of comparing them to a precise as possible theoretical calculation of the Lamb-shifted and the ideal, undressed transmon frequency. The accuracy to which we can determine the Lamb shift is ultimately limited by *both* the precision with which we are able to measure the qubit frequency and with which we can calculate it from the measured qubit parameters.

In the first generation of circuit QED experiments with the conventional Cooper pair box [2, 4], the coupling between cavity and qubit was comparably low ($g/2\pi \sim$30 MHz), though sufficiently high to reach the strong coupling regime and observe vacuum Rabi splittings. Since g also sets the magnitude of the dispersive Lamb shift $\delta_L = g^2/\Delta$, it was not possible in these experiments to resolve δ_L. Owning to the increased coupling strength of the transmon of up to $g/2\pi \sim 140$ MHz, also the dispersive interaction becomes much stronger and the Lamb shift is now on the order of several ten MHz, by far exceeding the qubit linewidth. This greatly helped the experiments presented here, as it enabled us to clearly separate δ_L in a comparison with the calculated undressed frequencies. Also, our understanding of the underlying theory and the ability to use it for precise numerical calculations has also strongly improved since the beginning of circuit QED [1, 8, 104].

For the comparison with our data shown below, we use exact numerical solutions of the full one-qubit Jaynes-Cummings Hamiltonian and the analytically exact undressed transitions obtained from Mathieu functions. In our numerical calculations, the full Hamiltonian is diagonalized on a $d = 10$ dimensional Hilbert space, accounting for the first five cavity eigenstates $|n\rangle$ and the lowest five transmon levels $\{|g\rangle, |e\rangle, |f\rangle, |h\rangle, |k\rangle\}$ of the qubit. The corresponding matrix is parametrized in terms of the fundamental transmon parameters $\{E_J^0, E_C\}$, the cavity resonance frequency ν_r and the maximum coupling strength g_{max}. These parameters were taken from the measured values shown in Tab. 5.2 (see also discussion below). Additionally, the gate charge n_g, the junction asymmetry d as well as the number of charge eigenstates n_c of the electrostatic part in the transmon Hamiltonian are required as input for the calculations. These were held fixed at the values $n_g = 1/2$ (sweet spot), $d = 0$ (symmetric junctions) and $n_c = 7$. Given all of the above parameters, the only variable remaining in the matrix equation is the flux bias Φ, i.e. we have

$$\mathbf{H}_{10\times10}\Psi_{10\times1} = E\vec{\Psi} \quad , \quad \mathbf{H} = \mathbf{H}(E_J^0, E_C, g_{\mathrm{max}}, \nu_r; \Phi) \tag{5.18}$$

where $\vec{\Psi}$ is a 10 component column vector and E are the eigenenergies of the complete qubit-cavity system. The numerical code for solving this equation was implemented in a *Mathematica* notebook by A. Blais. As shown below, the solutions obtained from this numerical treatment are in very good agreement with the measured data.

Results and Discussion

To resolve the relatively small Lamb shift of our solid state quantum system, an accurate measurement of the characteristic qubit parameters and their dependence on the control variables is required. In a first set of measurements we determine the period of modulation of the transition frequency of qubit A with magnetic field applied to the SQUID loop of the qubit. This is achieved by measuring the cavity transmission spectrum and simultaneously performing qubit spectroscopy using a dispersive measurement of the cavity frequency shift, see section 5.3 for details. With this procedure, we can determine both the flux periodicity and the flux offset due to magnetic offset fields to an accuracy better than $10^{-3}\phi_0$ using the flux matrix method discussed before. For generating the voltage bias of the coils a *Yokogawa* 7561 programmable DC source was used throughout the experiments. As mentioned above, qubit B was kept constant at $\Phi_0/2$ at all times during these experiments and could thus be ignored. Now tuning the flux bias applied to qubit A to $\Phi/\Phi_0 = 0$, the qubit is set to its maximum transition frequency $\omega_{ge}/2\pi = 7.84$ GHz (see Tab. 5.2), which we determine spectroscopically. At this bias point, we also determine the transition frequency $\omega_{gf}/2\pi$ between ground $|g\rangle$ and second excited qubit state $|f\rangle$ via two-photon absorption spectroscopy. With these two quantities we can in turn determine the maximum Josephson coupling energy $E_J^0 = 35.11$ GHz and the charging energy of our device $E_C = 231.7$ MHz at maximum positive detuning, where the dispersive shifts are negligibly small and the qubit is effectively undressed and described by the exact Mathieu solutions of the bare transmon Hamiltonian. The qubit parameters resulting from this first set of measurements are also summarized in Tab. 5.2. Finally, the input power from the microwave generators was ac-Stark shift calibrated [4], which gave a value of -35 dBm corresponding to one photon inside the resonator. This was done at large detunings between qubit and resonator where photon number splitting is effectively suppressed.

Following the accurate determination of the qubit parameters and their dependence on the control variables, we then proceed to observe the anti-crossing of the flux-tunable qubit and the fixed frequency resonator. This is achieved by measuring the resonator transmission spectrum while sweeping the flux bias around small detunings Δ, which in turn allows us to determine the coupling strength g between qubit and resonator. The probe beam microwave signals and the LO signal for the transmission measurements were generated with two separate, phase-locked *Agilent* E8257C signal generators (see also section 5.1). The individual spectra have been analyzed in *Mathematica*, where the maxima could be determined using a simple peak finding routine. The position of the peaks in each spectrum marks the transition frequencies and the FWHM gives the corresponding linewidth. The extracted frequencies $\nu_{\pm 1}$ of the qubit/cavity superposition states $|\pm n\rangle$ for $n = 1$ are shown as blue data points in Fig. 5.9a, measured with a probe tone power populating the resonator field with much less than one photon on average. On resonance ($\Delta = 0$), we determine the qubit/cavity coupling strength from the observed vacuum Rabi mode splitting to $g_{ge}/2\pi = 133$ MHz, see Fig. 5.9b. The extracted eigenfrequencies $\nu_{\pm 1}$ are in excellent agreement with the exact numerical solution of the full Jaynes-Cummings hamiltonian (solid green lines in Fig. 5.9a), as discussed above. At this point, we have fully determined the parameters governing the coupled qubit/resonator system and can set out at measuring the Lamb shift of the qubit spectroscopically.

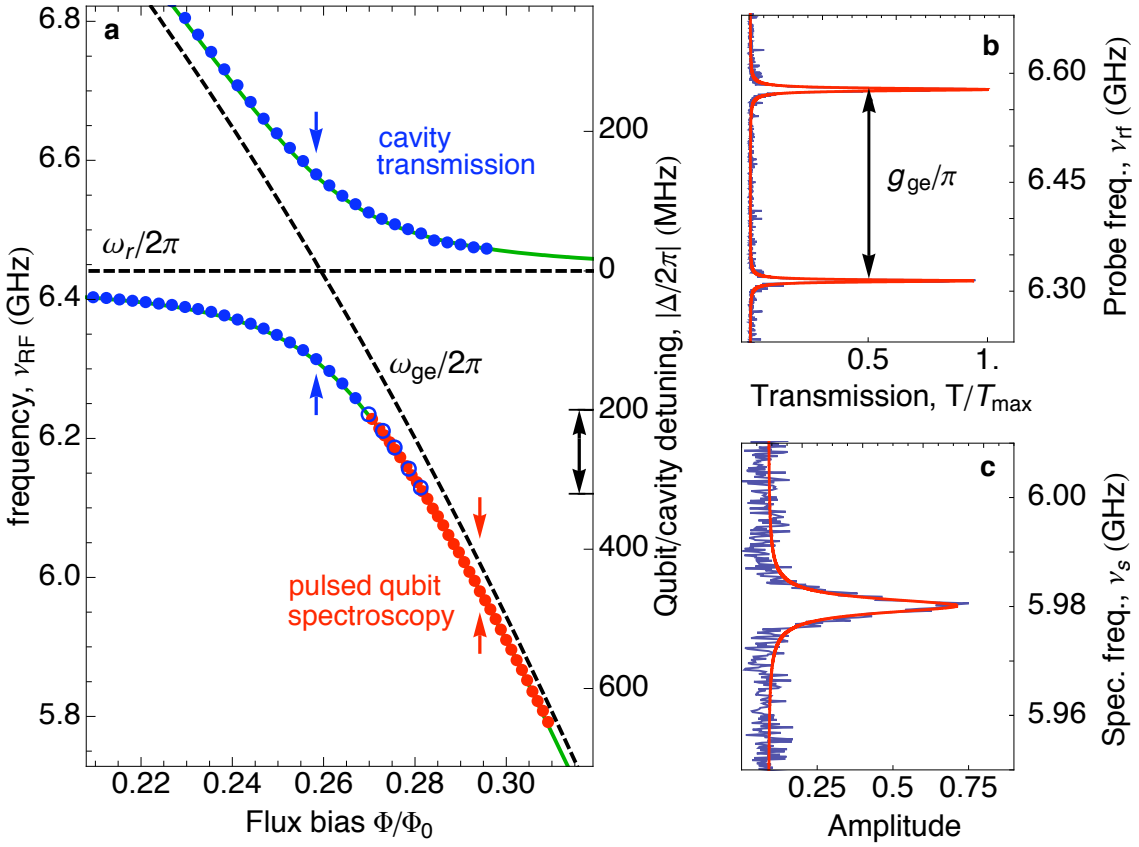

Figure 5.9: Spectrum of coupled qubit/cavity system. (**a**) Measured transition frequencies of cavity (blue data points) and qubit (red data points) versus normalized flux bias Φ/Φ_0. Dashed horizontal line is cavity transition frequency ν_r, dashed slanted line is calculated bare qubit transtion frequency ν_{ge}. Green solid lines are numerically calculated eigen-frequencies of the coupled system. See text for details. (**b**) Measured resonant vacuum-Rabi mode-split cavity transmission spectrum T (blue line) vs. probe frequency ν_{rf} at flux bias indicated by blue arrows in (**a**). Solid red line is a fit to a double-peak Lorentzian. (**c**) Measured spectroscopic qubit line shape (blue line) vs. spectroscopy frequency ν_s at flux bias indicated by red arrows in (**a**). Solid red line is a fit to a Lorentzian.

In section 4.1.3, we found for the Lamb shift of the transmon in the dispersive approximation

$$\delta_L = \chi_{01} = \frac{g_{01}^2}{\Delta} \tag{5.19}$$

with

$$\chi_{ij} = \frac{g_{ij}^2}{\omega_{ij} - \omega_r} \equiv \frac{g_{ij}^2}{\Delta_{ij}} \quad , \quad g_{ij} = \frac{2e}{\hbar}\beta V_{rms}\sqrt{\frac{i+1}{2}}\left(\frac{E_J}{8E_C}\right)^{1/4} . \tag{5.20}$$

The Lamb shift depends on the flux bias in two different ways. First, the coupling strength exhibits a weak power law dependence on the Josephson energy, which is in turn a function of flux. Furthermore, δ_L is inversely proportional to the detuning of qubit and cavity and thus also depends on the flux bias via the qubit frequency. This latter dependence is much stronger and will in a practice outweigh the flux dependence via the coupling. Hence, we can 'tune' the Lamb

shift and observe its behavior as a function of detuning by varying the external flux. This is the basic strategy in our measurements.
Using magnetic flux bias, we detune the qubit to well below the cavity resonance frequency ($\Delta \gg g_{ge}$) and spectroscopically determine its transition frequency $\tilde{\omega}_{ge}/2\pi$ by probing the resonator response in a dispersive measurement, see section 5.3. A typical qubit spectral line obtained in this way is shown in Fig. 5.9c. The qubit line width is on the order of $\delta_{ge} \sim 3\,\mathrm{MHz}$, slightly power broadened by the spectroscopy tone. Here it is important to point out that we are using the pulsed qubit spectroscopy scheme of section 5.3.2. This means, that first a long microwave pulse is applied to the qubit to prepare a fully mixed state and only after that we apply a measurement tone to the resonator. In this pulsed spectroscopy scheme, excitation and measurement tone are separated in time and the cavity is left approximately in the vacuum state $|0\rangle$ while the spectroscopy pulse is applied to the qubit. In contrast, using the continuous spectroscopy scheme of section 5.3.1 would result in an observation of a photon number-split qubit spectrum. In that case, the strong dispersive coupling leads to distinct, well-separated qubit lines corresponding to the individual photon number states, as is discussed theoretically in Ref. [104] as well as in section 5.4.2 and observed experimentally in Ref. [5].
In the following, we sequentially reduce the detuning Δ and extract the qubit transition frequency from the maximum in the pulsed spectroscopic line, as depicted in Fig. 5.9c. The extracted dressed frequencies $\widetilde{\omega}_{ge}/2\pi$ are shown as red data points in Fig. 5.9a. We observe that the measured frequencies coincide for all detunings with the frequencies calculated from the exact numerical diagonalization of the Jaynes-Cummings hamiltonian (solid green line). The difference between the measured and the bare qubit transition frequency (dashed slanted line in Fig. 5.9a), resulting from the interaction with the vacuum fluctuations, is clearly observed and well resolved by many line widths. This represents a direct spectroscopic observation of the Lamb shift in a solid-state system and demonstrates the dispersive interaction of a superconducting qubit with the vaccuum field in a cavity.

The measured transition frequencies are in very good agreement with the numerical solution of the Jaynes-Cummings Hamiltonian which in turn puts us in a position to explicitly extract the Lamb shift from the pulsed spectroscopy data vs. flux-controlled detuning . The frequency shift δ_L is determined by means of subtracting the measured qubit transition frequency $\widetilde{\omega}_{ge}/2\pi$ from the undressed transition frequencies $\omega_{ge}/2\pi$ obtained from the exact Mathieu solution of the transmon Hamiltonian (dashed slanted line in Fig. 5.9a), as shown by red data points in Fig. 5.10. The measured data is good agreement with the Lamb shift calculated from the full Jaynes-Cummings hamiltonian including counter-rotating terms, shown as the solid red line in Fig. 5.10. For the measured range of detunings, we find that the Lamb shift varies from about 30 MHz at a detuning of $\Delta \sim 620\,\mathrm{MHz}$ to 85 MHz at $\Delta \sim 130\,\mathrm{MHz}$, corresponding to a maximum value of roughly 1.4 % of the bare qubit transition frequency. By comparison, the 1s-2s transition in a Hydrogen atom has a transition frequency of 2466.06 THz with an absolute Lamb shift of 1040 MHz, corresponding to a relative shift of only 0.0001% [20, 21]. Note that the strongly increased Lamb shifts we observe here are ultimately a result of the enhancement of the qubit-vacuum interaction by the cavity. For comparison the Lamb-shift g_{ge}^2/Δ expected from the simple dispersive approximation of the hamiltonian is shown as a dashed green line in the same plot. The dispersive approximation is in good agreement with the data for large

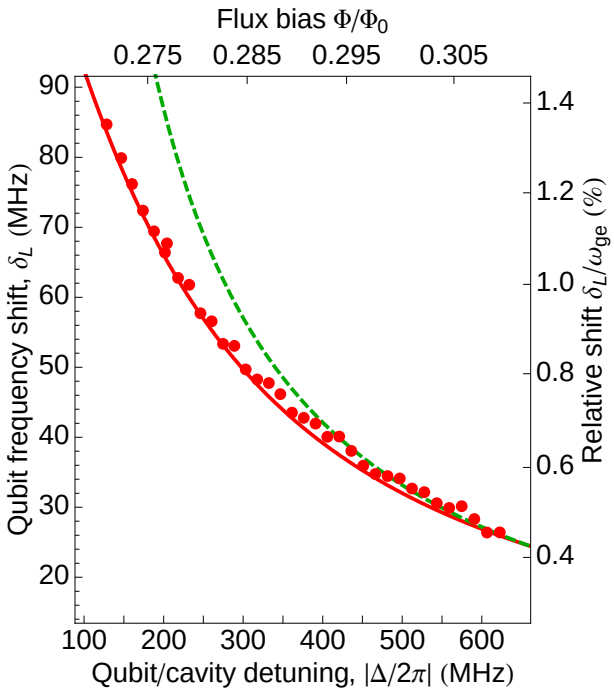

Figure 5.10: Lamb shift. Difference between measured qubit transition frequency $\widetilde{\omega}_{ge}/2\pi$ dressed by the vacuum field fluctuations (red data points) and calculated bare qubit transition frequency $\omega_{ge}/2\pi$ *vs.* qubit-cavity detuning $\Delta/2\pi$ (bottom axis) and normalized flux bias Φ/Φ_0 (top axis). Red line is predicted Lamb shift calculated using exact numerical diagonalization of the Jaynes-Cummings hamiltonian. Also shown is a comparison to the approximate dispersive result $\delta_L = g^2/\Delta$ (dashed green line)

detunings and is seen to break down for small Δ. The Bloch-Siegert shift resulting from the counter-rotating terms [120] is small for the given coupling strengths in our system and could not be clearly resolved.

Moreover, we also note that, over the range of detunings indicated by the double-headed arrow in Fig. 5.9a, the energy of the coupled qubit/resonator system can be extracted from both the photonic component, measured by probing the cavity resonance frequency, as well as from the qubit component measured spectroscopically. We observe virtually identical, and thus consistent frequencies in the overlap of the data from the two independent measurements (open blue and solid red data points).

5.4.2 Stark Effect and Photon Number Splitting

In the measurement of the Lamb shift, we have made the transition from the dispersive to the resonant vacuum field interaction, with the cavity populated one photon at maximum. In order to carefully check that the observed energy shifts are in fact solely due to the vacuum fluctuations of the radiation field and are not confused with a.c. Stark shifts induced by residual photons in the cavity, the system can now be investigated further by letting the qubit interact with a coherent photon field and compare the resulting frequencies with the Lamb shift data obtained

in section 5.4.1. Each of the individual photon number states in the cavity dispersively shifts the qubit transition frequency. In section 4.1.3, it was shown that the qubit frequency acquires a photon number dependent shift in the dispersive regime of large detunings. For the transmon, the ac Stark shift is given to lowest order by [69]

$$\delta_S = 2\chi \langle a^\dagger a \rangle = (2\chi_{01} - \chi_{12}) \langle a^\dagger a \rangle \tag{5.21}$$

with

$$\chi = \chi_{01} - \frac{\chi_{12}}{2} \quad , \quad \chi_{ij} = \frac{g_{ij}^2}{\omega_{ij} - \omega_r} \equiv \frac{g_{ij}^2}{\Delta_{ij}} \tag{5.22}$$

and the coupling strength $g_{i,i+1}$ as given in (5.20). If the shift per photon becomes large enough and exceeds the qubit linewidth, the qubit transition peak in a spectroscopic measurement will split up into multiple peaks, each one corresponding to an individual photon number state of the cavity. This so-called photon number splitting was successfully observed for the first time in [5]. Here, we are interested in resolving these photon number peaks to establish a consistent picture of the dispersive matter-light interaction with the vacuum (Lamb shift) as well as the real photon field (Stark shift) and ensure that our Lamb shift measurements have indeed been carried out in absence of any coherent or thermal photons, i.e. in pure vacuum. To observe these distinct peaks, the cavity has to be controllably populated with photons. This is achieved naturally in a continuous spectroscopy measurement (section 5.3.1).

The measurements and data analysis were carried out in complete analogy to the Lamb and vacuum Rabi splitting observation presented in section 5.4.1, the only difference being that here we used continuous instead of pulsed qubit spectroscopy. This means, that we apply a continuous wave coherent microwave field at the resonator frequency with the qubit in the ground state $(\omega_r - \delta_S/2n)$, populating the cavity with a small mean photon number. As discussed in section 5.3, the same microwave tone is simultaneously used to perform a dispersive measurement of the qubit state.

The extracted dressed qubit frequencies as functions of flux bias are shown in Fig. 5.11 for different intra-cavity photon numbers. The number-split qubit transition frequencies for $n = 0, 1, 2, 3, 4$ are shown as colored dots (blue to cyan) and compared to the numerical calculations depicted by the solid lines. For comparison, the pulsed spectroscopy data from section 5.4.1 is also shown (red open circles). To arrive at a coherent cavity population, we applied a probe microwave signal ν_{rf} with a power of -24 dBm at the RF generator output, corresponding to roughly -120 dBm at the sample level. Again, we clearly observe that the qubit frequency ifs Lamb-shifted with respect to its bare frequency by the $|n = 0\rangle$ vacuum state of the cavity. The individual photon number states $|n\rangle$ for $n = 0, 1, 2, 3, 4$ are clearly resolved and the coherent nature of the excitations is visible from the non-monotonic peak heights in the number-split qubit spectra shown in Fig. 5.11b and c, taken at the two different detunings indicated by colored arrows in Fig. 5.11a. The relative area under each peak in the transmission represents a qualitative measure of the cavity photon statistics [5]. In a thermal photon distribution the weights of the peaks decrease monotonically, while in a coherent distribution they exhibit a non-monotonic behavior [121]. In summary, the complete set of data is in very good agreement with the numerical solution of the Jaynes-Cummings Hamiltonian and it convincingly and consistently

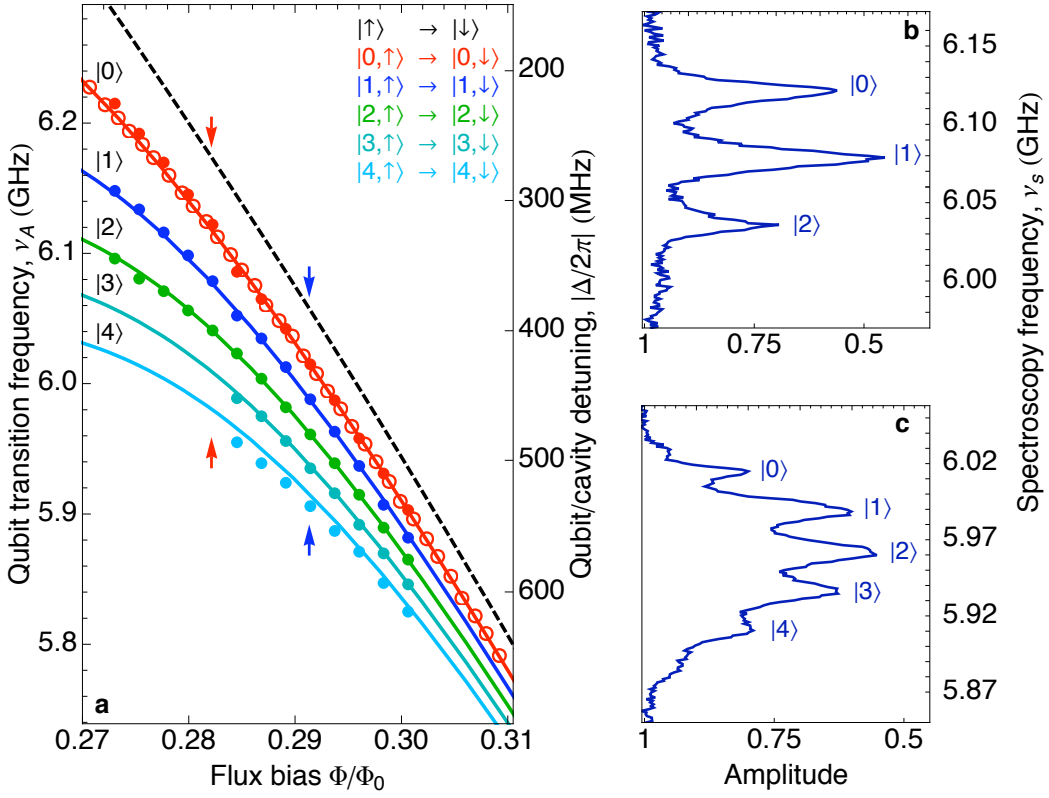

Figure 5.11: Number splitting and a.c. Stark Shift. (a) Spectroscopically measured qubit transition frequency $\tilde{\omega}_{ge}/2\pi$ (data points) dressed by a weak coherent field. Colors (red to cyan) correspond to number-split qubit states with $n = 0, 1, 2, 3, 4$, respectively. Solid lines are corresponding dressed state energy levels calculated by exact diagonalization of the Jaynes-Cummings hamiltonian, dashed line is bare qubit transition frequency. (b,c) Measured number-split qubit spectrum at flux bias indicated by blue (red) arrows in (a). The photon number states $|n\rangle$ corresponding to each peak are indicated.

demonstrates that the measured frequency shift for an empty cavity ($n = 0$) can be associated with the vacuum fluctuations of the cavity radiation field.

As a final check, we have determined the background thermal photon number in our circuit QED system by carefully probing the resonant vacuum Rabi mode splitting. A small thermal population of the $|\pm 1\rangle$ states can be detected through the transitions from the first doublet of the Jaynes-Cummings ladder into the second doublet $|\pm 1\rangle \rightarrow |\pm 2\rangle$, appearing as weak lines in the transmission spectrum of the resonator. The effective temperature of the radiation field is estimated to be $T_r \approx 90\,\mathrm{mK}$, corresponding to a mean thermal photon number of $\bar{n}_{th} \approx 0.03$, where we have analyzed in detail the amplitudes of these lines in the vacuum Rabi mode splitting [122, 123].

Another particularly interesting observation concerns the relative size of the Lamb and a.c. Stark shifts. In general, the a.c. Stark shift per photon is expected to be twice as large as the shift induced by the vacuum field. However, we make the surprising observation that the measured Stark shift per photon is in fact smaller than the Lamb shift. This phenomenon can be explained by considering the higher excited states of our qubit beyond $\{|e\rangle, |g\rangle\}$. As discussed theoretically

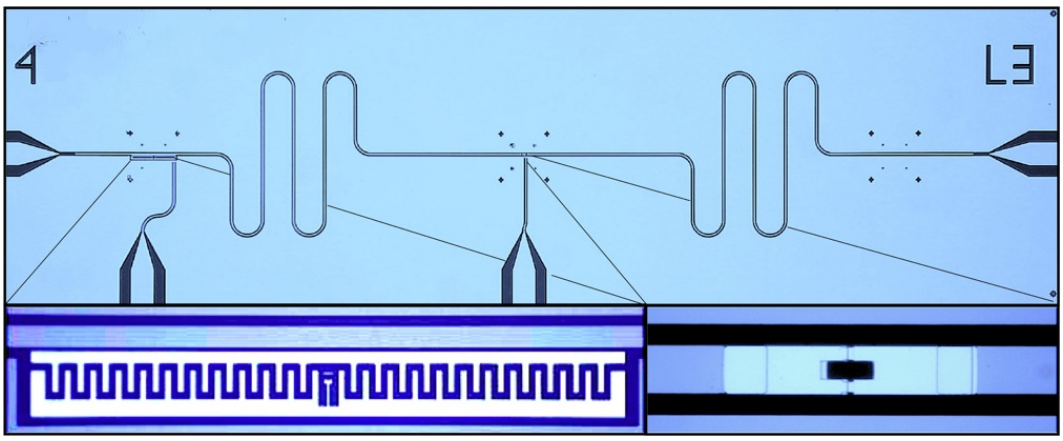

Figure 5.12: (Top) Optical image of the tunable superconducting coplanar waveguide resonator with the transmon type superconducting qubit and the SQUID loop embedded at the positions shown boxed. (Bottom) magnified view of boxed areas, showing the qubit with dimensions 300 $\times$ 30 μm^2 close to the center conductor and the SQUID of loop size 30 μm^2 incorporated at the center position.

in [69] and section 4.1.3, the a.c. Stark shift per photon is renormalized by presence of the third transmon level $|f\rangle$ and consequently reduced by a factor proportional to the level anharmonicity. The minimum measured anharmonicity of our artificial atom is on the order of $\alpha = E_{01} - E_{12} \sim$ 250 MHz, a value for which we indeed reach the limit of $\delta_S/n < \delta_L$. In this way, the qubit appears to couple more strongly to the vacuum field than to a single photon inside the cavity.

5.5 Single Qubit Coupled to Tunable Cavity

This section presents some preliminary results from the first successful coupling of a superconducting qubit to a flux-tunable cavity. Although preliminary, these results already hint at the fascinating possibilites for future experiments opening up in such a system. As the results have only been obtained very recently [4], this section will focus on a first characterization of the tunable cavity-qubit device rather than on more elaborate experiments. The strong coupling nature of the cavity qubit system is revealed by the observation of the vacuum Rabi splitting. The splitting is measured in two ways, first by tuning both qubit and cavity simultaneously (though with different periods) and second, by tuning the resonator nearly independently from the qubit. These results demonstrate that the roles of qubit and cavity can be effectively 'switched' in our Rabi splitting experiments.

The Sample

The sample consists of a superconducting transmon qubit coupled to a flux-tunable transmission line cavity incorporating a SQUID loop and was entirely fabricated in the clean room facilities at ETH Zurich. SQUID and transmon were patterned in the same electron beam lithography

[4] A measurement is running while these words are written.

run and deposited in a two step Aluminum shadow evaporation process. By means of covering half of the chip with a simple Aluminum foil, it was possible to fabricate SQUID and transmon under different angle configurations and thus with different metallization layer thicknesses. The SQUID was evaporated under +30° (30 nm Al) and -30° (150 nm), while the deposition of the transmon was carried out under 0° (20 nm) and +30° (80 nm). Optical microscope pictures of the complete chip as well as the transmon and the SQUID loop are depicted in Fig. 5.12. The cavity is characterized by a length of $\ell = 13200\,\mu$m and symmetric input/output coupling capacitances of $C_\kappa \sim 3.7$ fF (1+1 fingers, 74 μm each), identical to the device L1 discussed in section 5.2. There, transmission measurements yielded a maximum resonance frequency of $\nu_r = 5.85$ GHz and a quality factor of $Q = 3000$ at zero applied flux bias. For the SQUID loop, we have chosen a large degree of asymmetry of $d \sim 13\,\%$ with designed critical currents of $I_{c1} = 2.00\,\mu$A and $I_{c2} = 2.60\,\mu$A. In that way, the noise sensitivity of the tunable resonator system is drastically reduced, in principle allowing for a more stable operation under flux bias and a suppression of the quality factor degradation.

Flux Control and Cross Coupling

For applying the external flux bias to both the SQUID-cavity and the transmon qubit, two coils wound with superconducting Nb-Ti alloy wires in a *Torlon* chassis have been installed underneath the chip in the Copper sample holder, as discussed in detail in section 5.1. A small coil of loop size d = 3 mm is centered below the qubit and a larger one with d = 11 mm is positioned so that its center axis is aligned with the middle of the whole chip, i.e. with the SQUID-loop. As qubit and SQUID are spatially separated on the chip by 2400 μm, the flux generated by the small coil can be used to locally control the transmon while having only a very small influence on the SQUID loop. On the other hand, the flux generated by the large coil couples much more strongly to the SQUID loop than to the qubit. In turn we expect the qubit to have a large flux periodicity when biasing the large coil and a small one when applying a bias via the small coil. Likewise, the SQUID-loop will have a small flux periodicity on the large coil and a large one on the small coil. In that sense, we are able to drastically reduce cross coupling and allow for nearly independent flux control of the two systems. In order to further suppress cross coupling, the SQUIDs of the transmon and the cavity have been fabricated with different loop sizes. For the qubit, we have chosen the standard loop size of $A = 5\,\mu\text{m}^2$. In contrast, the SQUID loop inside the resonator was designed for a loop area of $A = 30\,\mu\text{m}^2$, giving an additional factor of 6 for independent flux control. Therefore, the resonator can in general be tuned with smaller flux periods than the transmon which in turn allows us to change the cavity resonance frequency $\omega_r(\Phi)$ while keeping the qubit transition frequency ω_a nearly constant. In the experiments presented here, the two coils are current-biased using two separate *Yokogawa* 7561 programmable DC sources.

5.5.1 Vacuum Rabi Splitting with Cavity Tuning

The first step in characterizing the tunable cavity-qubit system consists of a determination of the various flux periods and offsets from the two bias coils. In the set of measurements presented

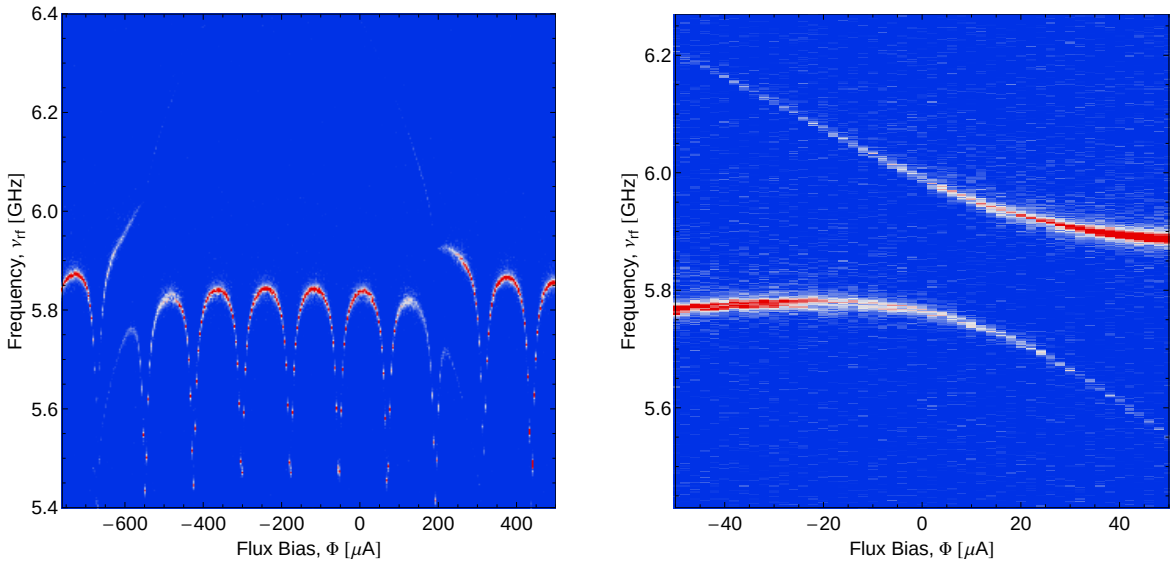

Figure 5.13: Measured resonator transmission spectra. (a) Density plot of resonator transmission with simultaneous tuning of qubit and cavity via the large coil. The flux periodicity of the resonator is clearly resolved and two anti-crossings are observed over the given range of current bias values. (b) Magnified view of anti-crossing between qubit and resonator. Note the different flux offset in comparison to (a).

here, the system is solely probed in transmission without applying separate spectroscopy pulses on the transmon qubit. In section 4.3, we found for the Hamiltonian of the tunable resonator-qubit system in the linear approximation

$$H_{\mathrm{JC}} = \hbar\omega_r(\Phi)\left(a^\dagger a + \frac{1}{2}\right) + \frac{\hbar\omega_a(\Phi)}{2}\sigma_z + \hbar g(a^\dagger\sigma^- + \sigma^+ a) + H_\gamma + H_\kappa\,. \tag{5.23}$$

In a typical experiment with a conventional qubit-transmission line resonator system, the modes of the resonator are fixed and the qubit resonance frequency is flux-tuned to enter the different regimes of circuit QED in the resonant ($\Delta = 0$) and the dispersive limit ($\Delta \gg g$). In the experiments presented here, however, these two limits can be reached either by tuning the cavity, the qubit or even by tuning both of them simultaneously. In order to determine the flux periods and show that qubit and cavity are in the strong coupling regime, the resonator transmission spectrum is measured while consecutively sweeping the flux bias of both the large and the small coil separately. The probe beam microwave signals and the LO signal for the transmission measurements were generated with two separate, phase-locked microwave signal generators, an *Agilent* E8257C and a *Rhode & Schwarz* SMR 40 generator, as is discussed in detail in section 5.1. A low input power of −35 dBm was chosen at the RF output such that the cavity is on average populated only with a single photon. In that way, possible nonlinear effects due the SQUID inside the resonator can be avoided (see also section 3.2.4).

In the first measurement that has been carried out, the large coil is sweeped over a wide range of flux values by applying a current bias in the range of $-750 \leq I_{\mathrm{bias}} \leq +450\,\mu$A. The small coil underneath the transmon qubit is kept constant with no current bias applied. Since here we are only interested in the frequencies, we have chosen comparably large frequency step sizes of 3

MHz in the transmission measurements. The corresponding density plot is shown in Fig. 5.13. Here, we observe two anti-crossings over the given range of flux bias values which demonstrates that the strong coupling regime between transmon and tunable resonator has been reached. The flux periodicity of both qubit and cavity is well resolved. As expected from the discussion of flux control given above, the resonator indeed has a much smaller period under the bias from the large coil than the transmon. As can be seen, the fact that both systems are tuned simultaneously results in splittings that stretch over several flux periods of the resonator. The flux periodicity of both the qubit and the cavity can then be determined by means of fitting the measured data to the corresponding theoretical expressions, from which we can also extract the critical currents and the degree of asymmetry of the SQUID. A magnified view of the vacuum Rabi splitting with simultaneous qubit and cavity tuning is shown in Fig. 5.13b. Here, we observe the avoided crossing of resonator and qubit by tuning the cavity with a small flux period and the qubit with a larger one using the same coil. The analysis of the measured spectra is more involved than for the simpler case of a fixed frequency resonator and has to be carried out using the theoretical expressions derived in section 4.3.

In summary, this very first transmission measurement presented here demonstrates the successful strong coupling of a superconducting qubit to a flux-tunable transmission line resonator. We observe vacuum Rabi splittings and show that the two different SQUID loops of qubit and cavity can be tuned with different periods. This experiment only represents the starting point of our investigations of the coupled system and thus only hints at the vast number of possibilities for future experiments.

6 Conclusion and Outlook

The results presented throughout this thesis summarize the achievements of one year of theoretical and experimental investigations in the Quantum Device Laboratory at ETH Zürich. The Lamb shift of a solid state quantum system has been observed spectroscopically for the first time. Here, it was successfully demonstrated that the coupling of a superconducting quantum bit to the vacuum fluctuations, strongly enhanced by the cavity, leads to maximum relative shifts of up to 1.4 % of the qubit transition frequency, allowing us to clearly resolve the dispersive interaction with the virtual photons of the electromagnetic field inside a transmission line resonator. Observing this small shift explicitly shows the presence of an important term in the dispersive circuit QED Hamiltonian that has not been investigated up until now. The clear observation of vacuum fluctuations in our strongly coupled system can serve as a motivation for further experiments aimed at investigating other effects triggered by quantum fluctuations in solid state systems. The Lamb shift is only one of many observable effects of the electromagnetic vacuum and the circuit QED architecture still offers a wide range of possible experiments on interesting related phenomena such as the Purcell effect and spontaneous emission [115, 116], the squeezing of quantum noise [124], amplification at the quantum limit [36] or the Casimir force [114].

The second part of this thesis consisted of the development of transmission line cavities whose resonance frequency can be tuned with an external magnetic field. All of the tunable coplanar waveguide resonators presented here have been developed from scratch. Starting from extensive theoretical simulations, an optical mask containing over 30 different resonators was designed. In the following, four tunable devices have been fabricated in the clean room facilities at ETH Zürich using photo- and electron beam lithography techniques. The cavities have been successfully measured in transmission and characterized in terms of their tuning behavior. Here, tuning ranges of up to 2.5 GHz have been demonstrated. Moreover, it was shown that for highly over-coupled resonators, the reported degrading of the quality factor [11, 90] can be effectively suppressed by choosing appropriate SQUID and resonator parameters. Finally, the strong coupling of a tunable cavity to a superconducting transmon qubit was achieved, where the corresponding vacuum Rabi splitting was observed in a transmission measurement. The first results presented here only give a hint of the vast number of possible experiments that can be carried out with these novel devices, such as in-situ tuning of single photons [90], detection of the quantum Zeno effect of itinerant photons [125], the implementation of a solid state photonic qubit [89] or ultra-fast entanglement between two qubits [10].

Acknowledgements

First of all I would like to thank my thesis supervisor Prof. Dr. Andreas Wallraff. He gave me the chance to work with a young and dynamic team on a project that greatly satisfied both my scientific as well as technological interests and introduced me to one of the currently most exciting and active areas of research in physics. The discussions with him provided me with a much deeper understanding and insight of the challenges of experimental quantum physics than I would have imagined possible and the results presented in thesis could not have been achieved without his continuous support, encouragement and advice. Most importantly, his fascination and excitement for circuit QED clearly passed on to me and motivated me to continue working in this field.

Furthermore, I would like to express my gratitude to all of my colleagues at the Quantum Device Lab. The development of the flux-tunable resonators was the result of a close collaboration with Martin Göppl, who introduced me to the art of micro- and nano-fabrication and with whom I had the chance to work on a resonator design study - a small side project to this thesis that was not presented here. Almost all of the devices he fabricated worked fantastically well, which paved the way for a successful project. Peter Leek supported me in the whole design process for the tunable cavities and readily answered the thousands of *Mathematica*-related questions I had. Moreover, I would like to thank Romeo Bianchetti for his help and patience in all things cryogenics-related, Johannes Fink for his advice on circuit QED measurements, Lars Steffen for working with me on the powder filters and Matthias Baur for taking late night calls on apparent *Labview* mysteries.

The theoretical calculations for the Lamb shift project were based on an extremely helpful *Mathematica* notebook by Prof. Dr. Alexandre Blais from Universite de Sherbrooke, for which I owe him a great deal of gratitude. In addition, he also readily provided the theory and quantization procedure for tunable resonators. Also, I would like to thank Prof. Dr. Karl Svozil from Vienna University of Technology for helping me in the formal difficulties that come along with doing a diploma thesis in a foreign country. Finally, I want to thank my parents for encouraging my curiosity and supporting me throughout the whole time of my studies, as well as all my friends in Zürich and Vienna who have made this final year of my Master's program an exciting and inspiring time.

Bibliography

[1] Blais, A., Huang, R. S., Wallraff, A., Girvin, S. M., and Schoelkopf, R. J. *Physical Review A* **69**(6), 062320 June (2004).

[2] Wallraff, A., Schuster, D. I., Blais, A., Frunzio, L., Huang, R. S., Majer, J., Kumar, S., Girvin, S. M., and Schoelkopf, R. J. *Nature* **431**, 162–167 (2004).

[3] Schoelkopf, R. and Girvin, S. *Nature* **451**, 664 (2008).

[4] Schuster, D. I., Wallraff, A., Blais, A., Frunzio, L., Huang, R. S., Majer, J., Girvin, S. M., and Schoelkopf, R. J. *Physical Review Letters* **94**(12), 123602 April (2005).

[5] Schuster, D. I., Houck, A. A., Schreier, J. A., Wallraff, A., Gambetta, J. M., Blais, A., Frunzio, L., Majer, J., Johnson, B., Devoret, M. H., Girvin, S. M., and Schoelkopf, R. J. *Nature* **445**(7127), 515–518 February (2007).

[6] Houck, A., Schuster, D., Gambetta, J., Schreier, J., Johnson, B., Chow, J., Frunzio, L., Majer, J., Devoret, M., Girvin, S., and Schoelkopf, R. *Nature* **449**, 328 (2007).

[7] Wallraff, A., Schuster, D. I., Blais, A., Frunzio, L., Majer, J., Girvin, S. M., and Schoelkopf, R. J. *Physical Review Letters* **95**, 060501 (2005).

[8] Blais, A., Gambetta, J., Wallraff, A., Schuster, D. I., Girvin, S. M., Devoret, M. H., and Schoelkopf, R. J. *Physical Review A* **75**(3), 032329 March (2007).

[9] Majer, J., Chow, J. M., Gambetta, J. M., Koch, J., Johnson, B. R., Schreier, J. A., Frunzio, L., Schuster, D. I., Houck, A. A., Wallraff, A., Blais, A., Devoret, M. H., Girvin, S. M., and Schoelkopf, R. J. *Nature* **449**(7161), 443–447 September (2007).

[10] Wallquist, M., Shumeiko, V. S., and Wendin, G. *Physical Review B* **74**(22), 224506 December (2006).

[11] Palacios-Laloy, A., Nguyen, F., Mallet, F., Bertet, P., Vion, D., and Esteve, D. *Journal of Low Temperature Physics* **(submitted)** (2007).

[12] Planck, M. *Annalen der Physik* **1**, 719–737 (1900).

[13] Einstein, A. *Annalen der Physik* **17**, 132–148 (1905).

[14] Haroche, S. and Kleppner, D. *Physics Today* **24** (1989).

[15] Raimond, J. M., Brune, M., and Haroche, S. *Rev. Mod. Phys.* **73**(3), 565–582 Aug (2001).

[16] Mabuchi, H. and Doherty, A. C. *Science* **298**(5597), 1372–1377 (2002).

[17] Walther, H., Varcoe, B. T. H., Englert, B.-G., and Becker, T. *Reports on Progress in Physics* **69**(5), 1325–1382 (2006).

[18] Thompson, R. J., Rempe, G., and Kimble, H. J. *Physical Review Letters* **68**(8), 1132–1135 Feb (1992).

[19] Sillanpaa, M. A., Park, J. I., and Simmonds, R. W. *Nature* **449**(7161), 438–442 September (2007).

[20] Lamb, W. E. and Retherford, R. *Physical Review* **72**, 241 (1947).

[21] Niering, M., Holzwarth, R., Reichert, J., Pokasov, P., Udem, T., Weitz, M., and Hänsch, T. *Physical Review Letters* **84**, 5496 (2000).

[22] Walls, D. and Milburn, G. *Quantum optics*. Spinger-Verlag, Berlin, (1994).

[23] Shor, P. W. *SIAM Journal on Scientific and Statistical Computing* **26**, 1484 (1997).

[24] Grover, L. K. In *Proceedings of the twenty-eighth annual ACM symposium on Theory of computing*, 212–219 (ACM, Philadelphia, Pennsylvania, United States, 1996).

[25] Nielsen, M. A. and Chuang, I. L. *Quantum Computation and Quantum Information*. Cambridge Univertity Press, (2000).

[26] Bennett, C. and Brassard, G. *Int. Conf. on Computers, Systems and Signal Processing* , 175 (1984).

[27] Cirac, J. I. and Zoller, P. *Physical Review Letters* **74**, 4091–4094 (1995).

[28] Gulde, S., Riebe, M., Gavin, P., Lancaster, T., Becher, C., Eschner, J., Häffner, H., Schmidt-Kaler, F., Chuang, I., and Blatt, R. *Nature* **421**, 48–50 (2003).

[29] Loss, D. and DiVincenzo, D. P. *Physical Review A* **57**(1), 120– January (1998).

[30] Hennessy, K., Badolato, A., Winger, M., Gerace, D., Atature, M., Gulde, S., Falt, S., Hu, E. L., and Imamoglu, A. *Nature* **445**(7130), 896–899 February (2007).

[31] Jones, J. A., Mosca, M., and Hansen, R. *Nature* **393**, 344 (1998).

[32] Chuang, I. L., Vandersypen, L. M. K., Zhou, X., Leung, D. W., and Lloyd, S. *Nature* **393**, 143 (1998).

[33] Nakamura, Y., Pashkin, Y. A., and Tsai, J. S. *Nature* **398**(6730), 786–788 April (1999).

[34] Bouchiat, V., Vion, D., Joyez, P., Esteve, D., and Devoret, M. H. *Physica Scripta* **T76**, 165–170 (1998).

[35] van der Wal, C. H., ter Haar, A. C. J., Wilhelm, F. K., Schouten, R. N., Harmans, C. J. P. M., Orlando, T. P., Lloyd, S., and Mooij, J. E. *Science* **290**(5492), 773–777 October (2000).

[36] Castellanos-Beltran, M. and Lehnert, K. *Appl. Phys. Lett.* **91**, 083509 (2007).

[37] Manucharyan, V. E., Boaknin, E., Metcalfe, M., Vijay, R., Siddiqi, I., and Devoret, M. *Physical Review B* **76**, 014524 (2007).

[38] Clarke, J. and Braginsky, A. *The SQUID Handbook*. Wiley-VCH, (2006).

[39] Martinis, J. M., Nam, S., Aumentado, J., and Urbina, C. *Physical Review Letters* **89**(11), 117901 September (2002).

[40] Goldstein, H. *Classical Mechanics*. Addison-Wesley, (1980).

[41] Devoret, M. *Quantum Tunnelling in Condensed Media*. Elsevier, Amsterdam, (1992).

[42] Caldeira, A. O. and Leggett, A. J. *Annals of Physics* **149**(2), 374–456 September (1983).

[43] Leggett, A. *Journal of Physics* **CM 14**, R415 (2002).

[44] Devoret, M., Martinis, J., and Clarke, J. *Physical Review Letters* **55**, 1908 (1985).

[45] Martinis, J. M., Devoret, M. H., and Clarke, J. *Physical Review B* **35**(10), 4682–4698 Apr (1987).

[46] Leggett, A. *Prog. Theoret. Phys.* **69**, 80 (1980).

[47] Devoret, M. *Quantum Fluctuations*. Elsevier, Amsterdam, (1996).

[48] Devoret, M. H., Wallraff, A., and Martinis, J. M. *cond-mat/0411174* (2004).

[49] Tinkham, M. *Introduction to Superconductivity*. McGraw-Hill International Editions, (1996).

[50] Josephson, B. D. *Physics Letters* **1**(7), 251–253 July (1962).

[51] Anderson, P. and Rowell, J. *Physical Review Letters* **10**, 230 (1963).

[52] Feynman, R., Sands, M., and Leighton, R. *The Feynman Lectures on Physics Vol.3*. Addison-Wesley, (1971).

[53] Ambegaokar, V. and Baratoff, A. *Physical Review Letters* **10**, 486 (1963).

[54] Gersten, J. and Smith, F. *The Physics and Chemistry of Materials*. Wiley, New York, (2001).

[55] Stewart, W. *Applied Physics Letters* **12**, 277 (1968).

[56] McCumber, E. *Journal of Applied Physics* **39**, 3113 (1968).

[57] London, F. *Superfluids*. Wiley, New York, (1950).

[58] Deaver, B. and Fairbank, W. *Physical Review Letters'* **7**, 43–46 (1961).

[59] Doll, R. and Näbauer, M. *Physical Review Letters* **7**, 51–52 (1961).

[60] Silver, A. and Zimmermann, J. *Physical Review* **158**, 423 (1967).

[61] de Bruyn-Ouboter, R. and de Waele, A. *Progress in Low Temp. Phys.* **4** (1970).

[62] Makhlin, Y., Schön, G., and Shnirman, A. *Rev. Mod. Phys.* **73**(2), 357–400 May (2001).

[63] Vion, D., Aassime, A., Cottet, A., Joyez, P., Pothier, H., Urbina, C., Esteve, D., and Devoret, M. H. *Science* **296**, 886–889 (2002).

[64] Cottet, A., Vion, D., Aassime, A., Joyez, P., Esteve, D., and Devoret, M. H. *Physica C* **367**(1-4), 197–203 February (2002).

[65] Mooij, J., Orlando, T., Levitov, L., Tian, L., van der Wal, C., and Lloyd, S. *Science* **285**, 1036 (1999).

[66] Friedman, J. R., Patel, V., Chen, W., Tolpygo, S. K., and Lukens, J. E. *Nature* **406**(6791), 43–46 July (2000).

[67] Büttiker, M. *Physical Review B* **36**, 3548 (1987).

[68] Cottet, A. *Implementation of a quantum bit in a superconducting circuit*. PhD thesis, Universite Paris 6, (2002).

[69] Koch, J., Yu, T. M., Gambetta, J., Houck, A. A., Schuster, D. I., Majer, J., Blais, A., Devoret, M. H., Girvin, S. M., and Schoelkopf, R. J. *Physical Review A* **76**(4), 042319 (2007).

[70] Schreier, J., Houck, A., Koch, J., Schuster, D. I., Johnson, B., Chow, J., Gambetta, J., Majer, J., Frunzio, L., Devoret, M., Girvin, S., and Schoelkopf, R. *Physical Review B* **77**, 180502(R) (2008).

[71] Schuster, D. I. *Circuit Quantum Electrodynamics*. PhD thesis, Yale University, (2007).

[72] Bouchiat, V. *Quantum fluctuations of the charge in single electron and single Cooper pair devices*. PhD thesis, Universite Paris VI, CEA-Saclay, (1997).

[73] Di Vincenzo, D. *Science* **270**, 255 (1995).

[74] Martinis, J. M., Cooper, K. B., McDermott, R., Steffen, M., Ansmann, M., Osborn, K. D., Cicak, K., Oh, S., Pappas, D. P., Simmonds, R. W., and Yu, C. C. *Physical Review Letters* **95**, 210503 (2005).

[75] Van Harlingen, D., Robertson, T., Plourde, B., Reichardt, P., Crane, T., and Clarke, J. *Physical Review B* **70**, 064517 (2004).

[76] Wellstood, F., Urbina, C., and Clarke, J. *Applied Physics Letters* **50**, 772 (1987).

[77] Wellstood, F., Urbina, C., and Clarke, J. *Applied Physics Letters* **85**, 5296 (2004).

[78] Constantin, M. and Yu, C. *Physical Review Letters* **99**, 207001 (2007).

[79] Koch, R., DiVincenzo, D., and Clarke, J. *Physical Review Letters* **98**, 267003 (2007).

[80] Eroms, J., van Schaarenburg, E., Driessen, C., Plantenberg, J., Huizinga, C., Schouten, R., Verbruggen, A., Harmans, C., and Mooij, J. *Applied Physics Letters* **89**, 122516 (2006).

[81] Wendin, G. and Shumeiko, V. In *Handbook of Theoretical and Computational Nanotechnology,* Rieth, M. and Schommers, W., editors, volume 3. American Scientific Publishers (2006).

[82] Bialczak, R., McDermott, C., Ansmann, M., Hofheinz, M., Katz, N., Lucero, E., Neeley, M., O'Connell, A., Wang, H., Cleland, A., and Martinis, J. *Physical Review Letters* **99**, 187006 (2007).

[83] Schoelkopf, R. J., Clerk, A. A., Girvin, S. M., Lehnert, K. W., and Devoret, M. H. *cond-mat/0210247* (2002).

[84] Abragam, A. *Principles of Nuclear Magnetism*. Oxford University Press, (1961).

[85] Gruska, J. *Quantum Computing*. McGraw Hill, (2000).

[86] Ithier, G., Collin, E., Joyez, P., Meeson, P. J., Vion, D., Esteve, D., Chiarello, F., Shnirman, A., Makhlin, Y., Schriefl, J., and Schon, G. *Physical Review B* **72**, 134519 (2005).

[87] Martinis, J. M., Nam, S., Aumentado, J., Lang, K., and C., U. *Physical Review B* **67**, (9):094510 (2003).

[88] Fink, J. M., Göppl, M., Baur, M., Bianchetti, R., Leek, P. J., Blais, A., and Wallraff, A. *Nature* **454**, 315–318 (2008).

[89] Bourassa, J. and Blais, A. unpublished, (2007).

[90] Sandberg, M., Wilson, C., Persson, F., Johansson, G., Shumeiko, V., Duty, T., and Delsing, P. *arXiv:0801.2479v1* (2008).

[91] Pozar, D. M. *Microwave Engineering*. Addison-Wesley Publishing Company, (1993).

[92] Goeppl, M., Fragner, A., Bianchetti, R., Fink, J., Leek, P., Puebla, G., and Wallraff, A. *arXiv:0807.4094v1* (2008).

[93] Wen, C. *IEEE Trans. Microwave Theory Tech.* **17**, 1087–1090 (1969).

[94] Simons, R. N. *Coplanar waveguide circuits, components and systems*. Wiley Series in Microwave and Optical Engineerging. Wiley Inter-Science, (2001).

[95] Frunzio, L., Wallraff, A., Schuster, D., Majer, J., and Schoelkopf, R. *IEEE Transactions On Applied Superconductivity* **15**(2), 860–863 June (2005).

[96] Watanabe, K., Yoshida, K., Aoki, T., and Kohjiro, S. *Jap. J. Appl. Phys.* **33**, 5708 (1994).

[97] Yoshida, K., Watanabe, K., Kisu, T., and Enpuku, K. *IEEE Trans. Appl. Supercond.* **5**(2), 1979–1982 (1995).

[98] Gorter, C. and Casimir, H. *Z. Physik* **15**, 549 (1934).

[99] Wallraff, A. *Fluxon Dynamics in annular Josephson juctions: From relativistic strings to quantum particles*. PhD thesis, University of Erlangen-Nürnberg, Germany, (2000).

[100] Jaynes, E. and Cummings, F. *Proceedings of the IEEE* **51**(1), 89–109 (1963).

[101] Lambropoulos, P. and Petrosyan, D. *Fundamentals of Quantum Optics and Quantum Information*. Springer, New York, (2006).

[102] Thompson, J., B. M. Zwickl, B., Jayich, A. M., Marquardt, F., Girvin, S. M., and Harris, J. G. *Nature* **452**, 72–75 (2008).

[103] Hood, C., Lynn, T. W., Doherty, A. C., Parkins, A. S., and Kimble, H. J. *Science* **287**, 5457 (2000).

[104] Gambetta, J., Blais, A., Schuster, D. I., Wallraff, A., Frunzio, L., Majer, J., Devoret, M. H., Girvin, S. M., and Schoelkopf, R. J. *Physical Review A* **74**(4), 042318 October (2006).

[105] Boissonault, M. Master's thesis, Universite de Sherbrooke, (2007).

[106] Fink, J. Master's thesis, Universität Wien, (2007).

[107] Leek, P. J., Fink, J. M., Blais, A., Bianchetti, R., Göppl, M., Gambetta, J. M., Schuster, D. I., Frunzio, L., Schoelkopf, R. J., and Wallraff, A. *Science* **318**(5858), 1889–1892 (2007).

[108] Uhlig, K. *Cryogenics* **44**, 53–57 (2004).

[109] Uhlig, K. and Wang, C. *AIP Conf. Proc.* **823**, 939 (2006).

[110] Uhlig, K. *AIP Conf. Proc.* **1287**, 985 (2008).

[111] Pobell, F. *Matter and Methods at Low Temperatures*. Springer, 3rd edition,, (2006).

[112] Uhlig, K. and Hehn, W. *Cryogenics* **37**, 279 (1997).

[113] Uhlig, K. *Cryogenics* **42**, 73–77 (2002).

[114] Casimir, H. and Polder, D. *Physical Review* **73**, 360 (1948).

[115] Purcell, E. M. *Physical Review* **69**, 681 (1946).

[116] Houck, A. A., Schreier, J. A., Johnson, B. R., Chow, J. M., Koch, J., Gambetta, J. M., Schuster, D. I., Frunzio, L., Devoret, M. H., Girvin, S. M., and Schoelkopf, R. J. *arXiv:0803.4490v1* (2008).

[117] Bethe, H. *Physical Review* **72**, 339 (1947).

[118] Schwinger, J. *Selected Papers on Quantum Electrodynamics*. Dover, New York, (1958).

[119] Steffen, L. Master's thesis, ETH Zurich, (2008).

[120] Bloch, F. and Siegert, A. *Physical Review* **57**, 522–527 (1940).

[121] Dykman, M. and Krivoglaz, M. *Sov. Phys. Solid State* **29**, 210 (1987).

[122] Rau, I., Johansson, G., and Shnirman, A. *Physical Review B* **70**, 054521 (2004).

[123] Bishop, L., Chow, J., Koch, J., Houck, A., Devoret, M., Thuneberg, E., Girvin, S., and Schoelkopf, R. *arXiv:0807.2882v1* (2008).

[124] Castellannos-Beltran, M., Irwin, K., Hilton, G., Vale, L., and Lehnert, K. W. *arXiv:0806.0659* (2008).

[125] Helmer, F., Mariantoni, M., Solano, E., and Marquardt, F. *arXiv:0712.1908v1* (2007).

[126] Wüster, W. , Semester Thesis, ETH Zürich (2008).

[127] Lukashenko, A. and Ustinov, A. V. *Review of Scientific Instruments* **79**(1), 014701–4 January (2008).

Appendix

A Full Circuit Quantization for Tunable Resonators

In section 3.2.2, it was shown that the Lagrangian of the transmission line resonator-SQUID circuit shown in Fig. 3.9 reads [89, 10]

$$\begin{aligned}\mathcal{L} &= \mathcal{L}_{\text{lhs}} + \mathcal{L}_{\text{s}} + \mathcal{L}_{\text{rhs}} \\ &= \sum_{i=1}^{N} \frac{1}{2}\left[C_1\dot{\Phi}_i^2 - \frac{(\Phi_{i+1}-\Phi_i)^2}{L_1}\right] \\ &+ \frac{C_J}{2}(\dot{\theta}_1 - \dot{\Phi}_{N+1})^2 - \frac{E_J}{2\phi_0^2}(\theta_1 - \Phi_{N+1})^2 \\ &+ \sum_{i=1}^{M} \frac{1}{2}\left[C_2\dot{\theta}_i^2 - \frac{(\theta_{i+1}-\theta_i)^2}{L_2}\right] \end{aligned} \tag{A.1}$$

where we have used the SQUID Lagrangian of section 2.4 and introduced the reduced flux quantum $\phi_0 = 2\pi/\Phi_0$. Note that here the harmonic approximation for the Josephson energy has already been made, i.e. $\mathcal{L}_s$ only contains the first non-vanishing term of the Josephson cosine potential

$$\mathcal{L}_s = \frac{C_J}{2}(\dot{\theta}_1 - \dot{\Phi}_{N+1})^2 - \sum_{n=0}^{\infty} \frac{(-1)^n}{2n!}\frac{E_J}{\phi_0^{2n}}(\theta_1 - \Phi_{N+1})^{2n}\,. \tag{A.2}$$

All higher order terms are neglected. Later on, we will recover the non-linearity from the harmonized Hamiltonian by means of treating the quartic order term of the Josephson potential perturbatively. Furthermore, note that we assume a flux-independent Josephson energy in (3.42), i.e. the SQUID is first treated as a single junction with Josephson energy E_J throughout the quantization procedure. The flux-dependence of the SQUID will then be recovered later on by making the simple transition $E_J \to E_J(\Phi)$.

Wave Equation

The Euler Lagrange equations $(d/dt)(\partial\mathcal{L}/\partial\dot{q}) - (\partial\mathcal{L}/\partial q_i) = 0$ resulting from the Lagrangian density (A.1) are wave equations for the generalized position coordinate on both sides of the SQUID ($x = 0$), i.e. for the node flux Φ_i ($x < 0$) and θ_i ($x > 0$). Making the transition to a

continuous description in (A.1)

$$\Delta x \to 0 \quad , \quad \sum_{i=1}^{N} \to \int_{-\ell_1}^{0} \quad , \quad \sum_{i=1}^{M} \to \int_{0}^{\ell_2} \quad , \quad (\Phi_i, \theta_i) \to (\Phi(x), \theta(x)) \tag{A.3}$$

and using the connection between lumped element and TL quantities per unit length $C_{1,2} = C^0_{1,2}\Delta x$ and $L_{1,2} = L^0_{1,2}\Delta x$, the Lagrangian is rewritten as

$$\begin{aligned} L &= \int_{-\ell_1}^{0} \frac{1}{2}\left[C(x)\dot{\Phi}^2 - \frac{1}{L(x)}\left(\frac{\partial\Phi}{\partial x}\right)^2\right] + \int_{0}^{\ell_2}\left[C(x)\dot{\theta}^2 - \frac{1}{L(x)}\left(\frac{\partial\theta}{\partial x}\right)^2\right] \\ &+ \frac{C_J}{2}\left(\dot{\theta}(0) - \dot{\Phi}(0)\right)^2 - \frac{1}{2L_J}\left(\theta(0) - \Phi(0)\right)^2 \end{aligned} \tag{A.4}$$

where we have defined

$$C(x) = \begin{cases} C_1^0 & x < 0 \\ C_2^0 & x > 0 \end{cases} \quad , \quad L(x) = \begin{cases} L_1^0 & x < 0 \\ L_2^0 & x > 0 \end{cases} \quad . \tag{A.5}$$

The wave equations for the flux field are then simply found as the Euler-Lagrange equations corresponding to (A.4):

$$\ddot{\Phi}(x,t) - \frac{1}{L(x)C(x)}\frac{\partial^2\Phi(x,t)}{\partial x^2} = 0 \quad , \quad \ddot{\theta}(x,t) - \frac{1}{L(x)C(x)}\frac{\partial^2\theta(x,t)}{\partial x^2} = 0 \tag{A.6}$$

with the standard plane wave solutions of the form

$$\Phi(x,t) = \sum_k e^{-i\omega_k t}\left(A_k e^{-ikx} + B_k e^{ikx}\right) \quad , \quad \theta(x,t) = \sum_q e^{-i\omega_q t}\left(C_q e^{-iqx} + D_q e^{iqx}\right) \tag{A.7}$$

where k and q are the wave numbers on the l.h.s and r.h.s of the SQUID, respectively. The corresponding frequencies are given in the usual form

$$\omega_k = \frac{k}{\sqrt{L_1^0 C_1^0}} \quad , \quad \omega_q = \frac{q}{\sqrt{L_2^0 C_2^0}}\,. \tag{A.8}$$

In the end, we are interested in continuous modes of the flux field rather than in the two separate wave functions (A.7). Such an expression can be derived by considering three fundamental constraints on the field: (i) the continuity condition at the SQUID position $x = 0$, (ii) the boundary condition that no current should flow outside the resonator on both ends $I_1(x = -\ell_1) = I_2(x = \ell_2) = 0$ and (iii) the conservation of current at the origin $I_1(x = 0) = I_2(x = 0)$. Consecutively applying these constraints leads to a transcendental equation for the field whose solutions form a complete, infinite set of orthogonal eigenfunctions [10, 89]. The detailed calculations that lead to this equation are presented in appendix A, where it is also shown that the eigenmodes of the total system $\Psi(x,t)$ can be written in a separational form $\Psi(x,t) = \sum_k \Psi_k(t)\chi_k(x)$.

Boundary Conditions and Solutions

Since we are interested in a single, continuous mode of the flux field that extends over the whole resonator rather than in the two separate wave functions (A.7), we can use the continuity condition at the singularity $x = 0$

$$\omega_k \equiv \omega_q \qquad k v_1 = q v_2 \tag{A.9}$$

so that the continuous mode we're looking for has the same frequency on both sides of the SQUID. Here, the phase velocities $v_1 = 1/\sqrt{L_1^0 C_1^0}$ and $v_2 = 1/\sqrt{L_2^0 C_2^0}$ have been introduced. Another constraint on the wavefunctions (A.7) is imposed by the boundary condition that no current should flow outside the resonator, i.e. the current must vanish at the ends of the resonator $I_1(x = -\ell_1) = I_2(x = \ell_2) = 0$. Since charge is the conjugate variable to flux, it holds for the current on the l.h.s that (see also section 2.1)

$$I_1(x,t) = \dot{q}(x,t) = -\frac{1}{L_1^0}\left(\frac{\partial \Phi(x,t)}{\partial x}\right) . \tag{A.10}$$

and similarly for the r.h.s current $I_2(x,t)$. Thus the boundary condition can be expressed as

$$\left(\frac{\partial \Phi(x,t)}{\partial x}\right)_{x=-\ell_1} = 0 \quad , \quad \left(\frac{\partial \theta(x,t)}{\partial x}\right)_{x=\ell_2} = 0 \tag{A.11}$$

from which it follows for the wave amplitudes that $B_k = A_k e^{2ik\ell_1}$ and $C_q = D_q e^{2iq\ell_2}$. Hence using this in combination with the continuity condition (A.9), the total flux field is obtained from (A.7) as

$$\Psi(x,t) = \sum_k \Psi_k(t) \begin{cases} A_k \cos[k(x+\ell_1)] & \text{for} \quad x < 0 \\ D_k \cos[k\frac{v_1}{v_2}(x-\ell_2)] & \text{for} \quad x > 0 \end{cases} \tag{A.12}$$

The third and final constraint is given by the conservation of current. The current flowing into the SQUID at $x = 0$ must be equal to the current flowing out $I_1(x = 0) = I_2(x = 0)$. Using (A.12) and the definition of the currents (A.10), we get

$$-A_k \frac{Z_2^0 \sin k\ell_1}{Z_1^0 \sin q\ell_2} = D_k \tag{A.13}$$

where the characteristic impedance $Z_i^0 = \sqrt{L_i^0/C_i^0}$, $i = 1, 2$ has been introduced. This equation fixes A_k with respect to D_k. The corresponding Euler Lagrange equation at $x = 0$ is obtained from (A.1) as

$$-C_J\left(\ddot{\theta}_1 - \ddot{\Phi}_{N+1}\right) + \frac{\Phi_{N+1} - \Phi_N}{L_1} - \frac{1}{L_J}(\theta_1 - \Phi_{N+1}) = 0 \tag{A.14}$$

which in the continuous limit (A.3) becomes

$$-C_J\left(\ddot{\theta}_k(0,t) - \ddot{\Phi}_k(0,t)\right) + \frac{1}{L(x)}\frac{\partial \Phi(x,t)}{\partial x}\,|_{x=0} - \frac{1}{L_J}(\theta_k(0,t) - \Phi_k(0,t)) = 0\,. \tag{A.15}$$

Now plugging in (A.12) and using (A.13), we find

$$\omega_k^2 C_J(D_k \cos q\ell_2 - A_k \cos k\ell_1) - \frac{k}{L(x)} A_k \sin k\ell_1 - \frac{1}{L_J}(D_k \cos q\ell_2 - A_k \cos k\ell_1) = 0\,. \quad \text{(A.16)}$$

Dividing this by $(A_k/L_J)\sin k\ell_1$ and using the definition of the resonance frequencies (A.8) as well as the condition (A.9), one finally arrives at a transcendental equation for the wave number k

$$\frac{L(x)}{L_J}\left(1 - \frac{\omega_k^2}{\omega_p^2}\right)\left(\frac{Z_2^0}{Z_1^0}\cot k\frac{v_1}{v_2}\ell_2 + \cot k\ell_1\right) = k \quad \text{(A.17)}$$

which was first derived in [10] for the case of a SQUID terminating a TL resonator and in [89] for a SQUID at arbitrary position. Here we have used the plasma frequency $\omega_p = 1/\sqrt{C_J L_J}$ of the SQUID which was already introduced in section 2.4. There it was shown, that the SQUID-loop essentially behaves like an oscillator of resonance frequency ω_p. Since we are only interested in single, well-isolated modes of the total system, excitations of the SQUID alone have to be avoided. Thus we have to ensure that $\omega_k \ll \omega_p$ so that the SQUID oscillator's resonances are effectively deactivated when driving the system at ω_k (see also section 3.2.4). In this limit, the transcendental equation reduces to

$$\frac{L(x)}{L_J}\left(\frac{Z_2^0}{Z_1^0}\cot k\frac{v_1}{v_2}\ell_2 + \cot k\ell_1\right) = k\,. \quad \text{(A.18)}$$

The solutions to this equation form a complete, infinite set of orthogonal eigenfunctions $\chi_k(x)$ and they are given by [89]

$$\chi_k(x) = \begin{cases} A_k \cos[k(x+\ell_1)] & \text{for} \quad x < 0 \\ D_k \cos[k\frac{v_1}{v_2}(x-\ell_2)] & \text{for} \quad x > 0 \end{cases} \quad \text{(A.19)}$$

so that we can finally write the eigenmodes of the total system in separation form

$$\Psi(x,t) = \sum_k \Psi_k(t)\chi_k(x)\,. \quad \text{(A.20)}$$

Note that here the amplitude A_k is determined by the normalization condition of the eigenfunctions $\{\chi_k\}$ which in turn also fixes D_k via (A.13). The continuous Lagrangian (A.4) can now be conveniently written as

$$L = \frac{1}{2}\int_{-\ell_1}^{\ell_2}\left[C(x)\dot{\Psi}(x,t)^2 - \frac{1}{L(x)}\left(\frac{\partial\Psi(x,t)}{\partial x}\right)^2\right]dx - \frac{1}{2L_j}(\Psi(0^+,t) - \Psi(0^-,t))^2\,. \quad \text{(A.21)}$$

The decomposition of the field into a spatial $\chi_k(x)$ and a time-dependent part $\Psi_k(t)$ in turn allows rewriting this Lagrangian as a sum of harmonic oscillators of frequency ω_k

$$L = \sum_k \frac{C_{\text{cav}}}{2}\dot{\Psi}(x,t) - \frac{C_{\text{cav}}\omega_k^2}{2}\Psi_k^2(t) \quad \text{(A.22)}$$

where the total capacitance of the cavity $C_{\text{cav}} = \int_{-\ell_1}^{\ell_2} C(x)dx$ was introduced. The fact that the Lagrangian can be written as a sum of harmonic functions results from the linear approximation of the Josephson potential that was made in the very beginning in (A.1). As shown below, the anharmonicity can be recovered by means of treating higher order terms of the potential perturbatively.
Using the fact that charge is the conjugate variable to the flux Ψ_k

$$q_k = \frac{\partial L}{\partial \dot{\Psi}_k}\,, \tag{A.23}$$

a Legendre transformation $H = \Psi_k q_k - L$ of the Lagrangian leads to the classical Hamiltonian

$$H_0 = \sum_k \frac{q_k^2}{2C_{\text{cav}}} + \frac{1}{2} C_{\text{cav}} \omega_k^2 \Psi_k^2\,. \tag{A.24}$$

As usual, the last step now consists of a second quantization where we introduce the ladder operators through

$$\Psi_k = \sqrt{\frac{\hbar}{2C_{\text{cav}}\omega_k}} \left(a_k^\dagger + a_k\right) \quad , \quad q_k = \sqrt{\frac{\hbar C_{\text{cav}}\omega_k}{2}} \left(a_k^\dagger - a_k\right)\,. \tag{A.25}$$

with the final Hamiltonian

$$H_0 = \sum_k \hbar\omega_k \left(a_k^\dagger a_k + \frac{1}{2}\right)\,. \tag{A.26}$$

This shows explicitly that in the linear SQUID regime $I \ll I_c$, the tunable cavity can be treated as a harmonic oscillator just like the regular cavities of section 3.1, the only difference being the flux-dependence of the resonance frequencies ω_k, which becomes obvious from the presence of the SQUID inductance L_J in the transcendental equation. If, however, higher order terms of the Josephson potential can not be neglected (i.e. for $I \gg I_c$), the harmonic oscillator description is no longer valid and the perturbed Hamiltonian acquires an anharmonic terms, as is discussed in detail in section 3.2.2.

B Ion Gun Etching

An important point in the tunable cavity fabrication process presented in section 3.2.5 is to clean the niobium surface of the resonators and remove any oxide layers before the deposition of the SQUIDs. Since the resonator structures and the SQUIDs are fabricated separately, the niobium surface can oxidize in between the two steps, resulting in NbO_x layers of several nm thickness. If the Aluminum SQUIDs were fabricated right on top of this layer, large contact resistances are possible and the $Nb/NbO_x/Al$ interface can in fact form a tunnel junction itself. In order to avoid this, the oxide layers are removed using an ion gun etching technique. This chapter discusses the measurements that were carried out for testing the equipment and determining the corresponding etching rates of the different materials used in our devices.

The *Veeco 3 cm DC Ion Source* as built-in in the PLASSYS evaporator system (herein referred to as 'ion gun') is an accurate tool for removing thin layers on wafers in the nm-range. Most importantly, it can be used to remove thin oxide layers on different materials that would otherwise influence their electrical properties. The target of the measurements presented here is an accurate determination of the ion gun etch rates on the different materials used in the fabrication of superconducting qubits and resonators, such as SiO_x, Nb and PMMA resist. To this aim, step heights and profiles have been measured on each material after different, well-defined time intervals of exposure to the ion gun. The simple test structure depicted in Fig.B.1a has been designed to allow for measuring the profiles with an Alpha Step 500 mechanical surface profiler system. With this test structure, an arbitrary number of measurements can be taken on different, spatially well-separated points of a given sample. The chosen measurement points are represented by the blue bars in Fig.B.1a, with the white areas corresponding to PMMA resist and the gray ones to the wafer surface (SiO_x or Nb).
A film of PMMA resist was first spun on each piece of sample-wafer (3000 rpm for 120 s) and then the simple test structure was written using standard electron beam lithography and developed in MIBK (90 s) and IPA (60 s), leaving the gray squares in Fig.B.1a uncovered by the resist and giving the initial profile shown in Fig.B.1b.
In total, more than 490 measurements have been made on 16 different samples with the Alpha Step 500 system. The following measurement procedure has been applied for each sample, with the variables as given in Fig. B.1b:

1. Measure initial step height h_1 at each designated point, giving 16 datapoints per sample. (h_1 should be identical to the thickness of the PMMA resist layer.)

2. Expose sample to ion gun beam for a time t_i with the following fixed parameters: beam current of $I_B = 10\,\text{mA}$, beam voltage $V_B = 300$ V, discharge current $I_D = 2.5$ A and

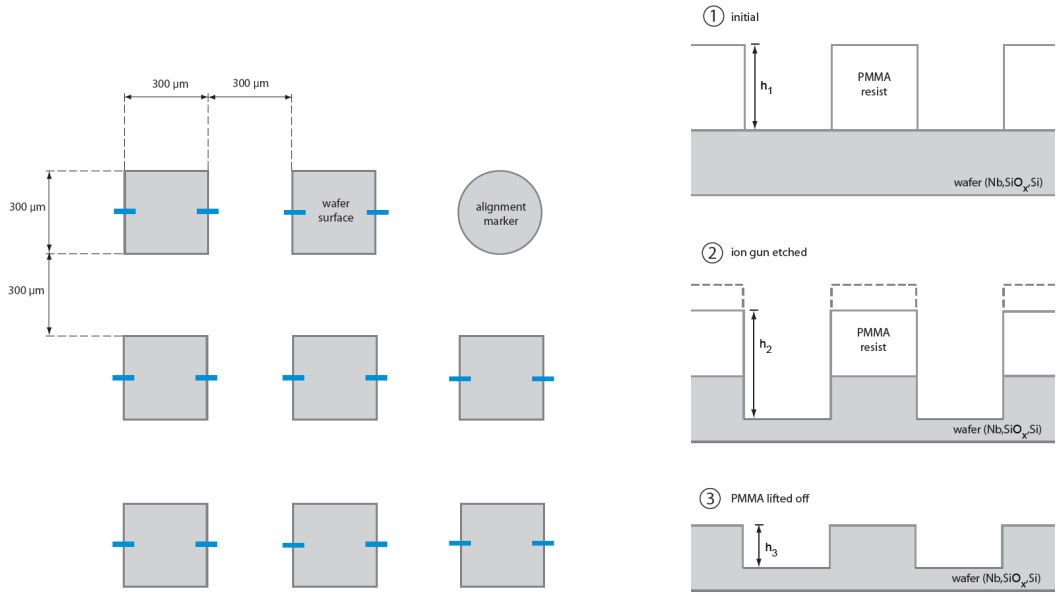

Figure B.1: (a) Design of the ion gun test structure. Measurement positions are indicated by the blue bars. Gray areas correspond to wafer surface and white ones to PMMA resist. (b) Illustration of the measurement procedure. Three different step heights h_1, h_2, h_3 are recorded at each measurement point from which the etching rates can be determined using Eqs. (B.1) - (B.3).

discharge voltage $V_D = 35$ V. These are the company-recommended parameters and they are totally sufficient for significant etching.

3. Measure resulting step height h_2 at each designated point before PMMA liftoff. In order to avoid any additional post-ion gun oxidation, the step heights have been measured *immediately* after the samples were removed from the PLASSYS loadlock chamber.

4. Lift-off PMMA resist layer using the following recipe: (1) 15 min. ultrasonic aceton bath at 50° C and medium power[1] (level '5' on a 40 kHz ultrasonic bath), (2) 5 min. ultrasonic aceton bath at 50° C and medium power, (3) 3 min. ultrasonic IPA bath at 50° C and medium power.

5. Measure resulting step height h_3 at each designated point after PMMA liftoff (This should be identical to the etched height of the substrate/metal layer). Again, in order to avoid formation of a new oxdation layer, the step heights have been measured *immediately* after the liftoff.

6. The etch rates for measurement point i are determined as follows:

   - Total etch rate:

$$R_{\text{total}}^{(i)} = \frac{h_1 - h_2}{t_i} \quad [\text{nm/min.}] \tag{B.1}$$

[1] Higher powers have been tried first, which however resulted in some samples breaking apart during liftoff. Thus a lower power has been chosen in the end.

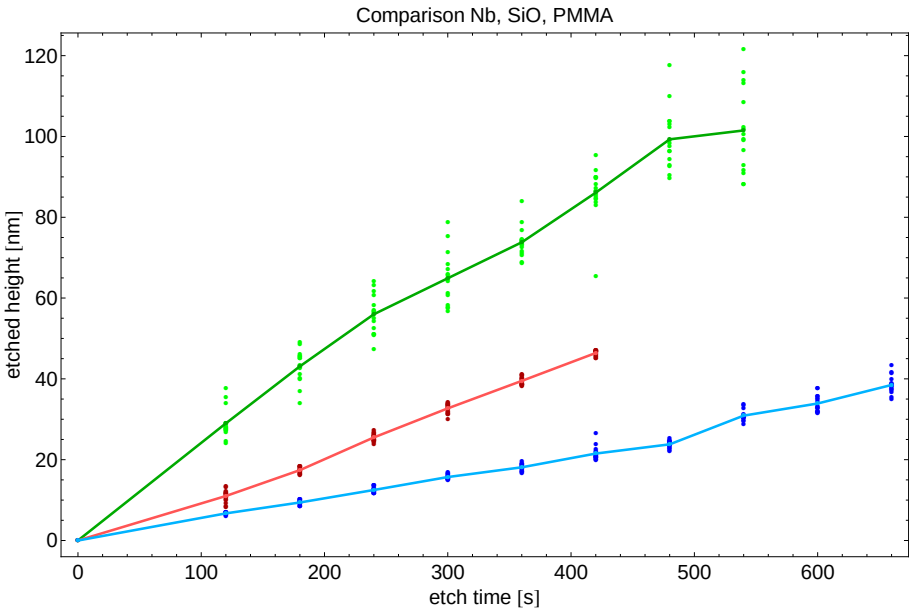

Figure B.2: Comparison of measured step heights on the different materials as a function of ion gun exposure time: PMMA (1:1) resist (green), Niobium (blue), SiO wafer substrate (red). The individual step heights taken at each point are shown as dots, with the averages connected by the solid lines.

- PMMA resist etch rate:

$$R_{\text{resist}}^{(i)} = \frac{h_1 - h_2 + h_3}{t_i} \quad [\text{nm/min.}] \tag{B.2}$$

- Substrate/metal layer etch rate:

$$R_{\text{sub}}^{(i)} = \frac{h_3}{t_i} \quad [\text{nm/min.}] \tag{B.3}$$

Note that this procedure allows for a *direct* determination of substrate/metal layer etching rates. A comparison of all measured step heights at different time intervals is shown in Fig. B.2 and the resulting etch rates for the different materials are given in the following:

$$\langle R_{\text{Nb}} \rangle \pm \sigma = 3.20 \pm 0.24 \quad [\text{nm/min.}] \tag{B.4}$$

$$\langle R_{\text{SiO}_x} \rangle \pm \sigma = 6.20 \pm 0.55 \quad [\text{nm/min.}] \tag{B.5}$$

$$\langle R_{\text{PMMA}} \rangle \pm \sigma = 13.00 \pm 1.59 \quad [\text{nm/min.}]\,. \tag{B.6}$$

C Junction Characterization and DC Measurements

A crucial step in the fabrication and design of Josephson-junction based devices is the determination of the critical current densities from the current-voltage characteristics (see section 2.3. Although by now a standard experiment, measuring the voltage response of a junction can be quite challenging, especially when the critical currents are small.
In the framework of this thesis, a setup for standard four-point dc measurements of Josephson junctions and SQUIDs has been developed and implemented in a dilution refrigerator at a base temperature of 15 mK. A discussion of the cryogenic aspects is postponed until section 5.1 and here we will focus on the implemented circuitry. The four-port measurement setup is shown in Fig. C.1. At room temperature, control and measurement of the current and voltage signals is handled via a bias box which provides inputs, outputs, amplifiers and filtering circuits, see top in Fig. C.1. The bias box is connected to an A/D-interface by *National Instruments*, which converts the analog current and voltage signals into digital ones for the data acquisition card build into a computer. Here, the bias current can be swept through using a *Labview* program, which also records the voltage drop at each distinct bias point. This Labview code was implemented in the framework of a semester thesis, see Ref. [126], where also a more detailed description of the bias box can be found. The software-controlled bias current at the output of the data acquisition card is converted via the A/D interface into an analog signal that is transferred to the bias box via standard coaxial cables, see inputs at the top of Fig. C.1. In the following, the bias box is connected to a breakout box that contains low-cutoff RC filters and handles the input and output of the signals into the cryostat via shielded cables. The breakout box has two inputs and two outputs and two separate closed circuits are formed inside the cryostat. One is used for current-biasing the device under test, the other one for measuring the voltage drop across the device, which in total realizes a standard four-point measurement. Once inside the cryostat, Copper twisted pair cables are used to bring the signals down to the 15 mK stage. Since even small charge fluctuations or thermal noise can lead to currents significantly exceeding I_c, careful noise filtering is required at the lowest temperature stage for measuring small critical currents and protecting the junctions. A first step towards achieving this is done by means of using low-cutoff stainless steel powder filters (SSPF) on both upward and downward lines at base temperature. These filters are based on eddy current dissipation effects and closely resemble those presented in Ref. [127]. Several different versions of SSPFs have been constructed and tested during this thesis. Here, we use filters with constantan wires, embedded in a mixture of *Stycast* glue and stainless steel powder with additional 100 nF capacitances to ground at the input and output ports of the filter. The filters are characterized by a low cutoff of roughly 500 kHz and provide

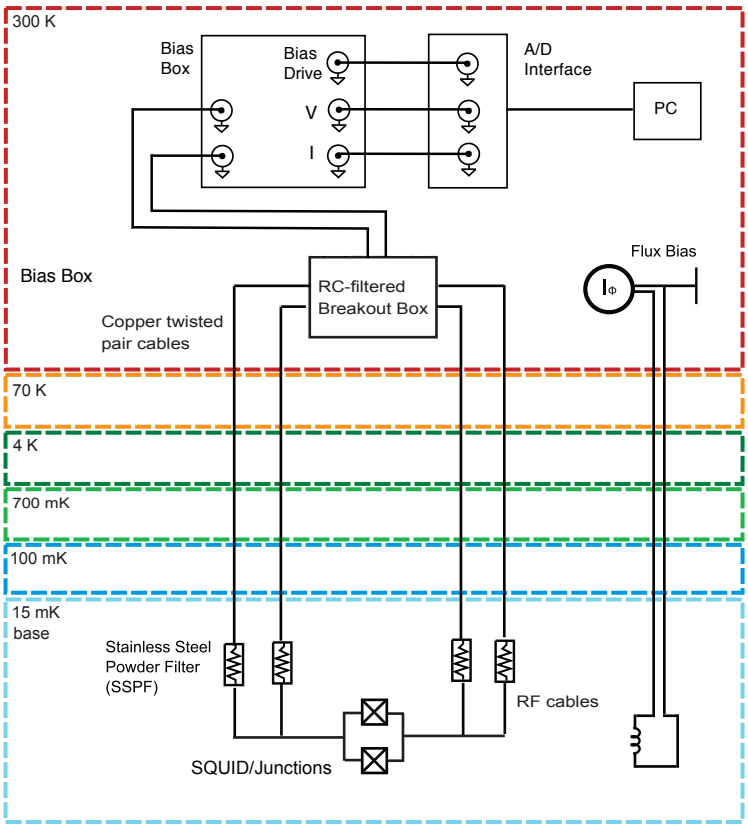

Figure C.1: Schematic setup of the implemented four-port DC circuit for Josephson junction characterization. Each line is filtered at base temperature using a stainless steel powder filter (see the discussion in the text). At room temperature, the signals are filtered by low-cutoff feedthrough RC filters built into a break out box.

for more than -60 dB attenuation in a range of up to 15 GHz. At base temperature, the sample is connected to the SSPFs via RF coaxial cables and mounted in a hermetic Copper box. Note that the circuitry inside the cryostat has been implemented twice in order to allow for measuring two devices per cooldown.

To test both the setup as well as the fabricated junctions, a series of measurements have been carried out on a set of SQUIDs. The test devices have been patterned using electron beam lithography and Al shadow-evaporation on a 2 x 7 mm Silicon substrate chip, mounted on a PCB board and each connected to two input and two output ports on the PCB using Al wire bonding. DC measurements were carried out by sweeping a bias current over several hundred nA and simultaneously monitoring the voltage drop across the junction. A typical measured IV curve is depicted in Fig. C.2. Although the essential features of the current-voltage characteristics are clearly observed, the results show a need for improving the setup. First, the curve as a whole is tilted, which means that there is a voltage drop somewhere in the circuit in parallel to the SQUID. The additional resistance that causes this drop has to be identified. Second, the extracted critical current is far lower than expected from the junction design. The SQUIDs

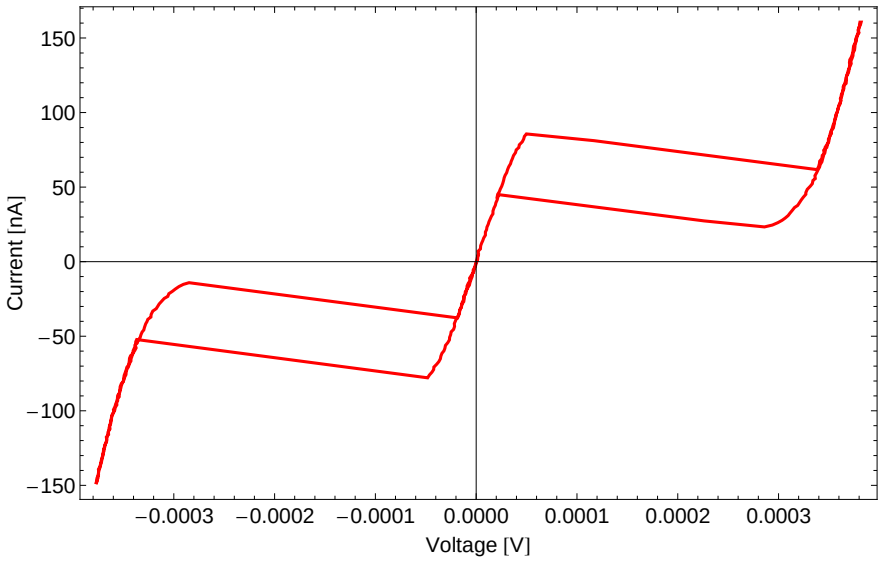

Figure C.2: Measured current voltage characteristics of a symmetric SQUID loop at zero flux bias. The essential features such as the switching from zero-voltage to voltage state are observed. However, the curve is tilted as a whole which hints at unidentified resistances in the setup (see the discussion in the text).

were fabricated with large junction sizes ($\sim 2\,\mu$m $\times$ 300 nm) and calculations predicted critical currents of 1-2 μA. The fact that the switching to the voltage state occurs in the nA range hints at a (so far unidentified) noise source that induces an additional current such that the critical current is exceeded before the actual measurement current reaches I_c. Unfortunately, the flux bias was not tested so far. A possible explanation for the low measured critical currents could also be magnetic offset fields such that at zero applied flux bias the SQUID is not at its maximum Josephson energy and critical current. The evident problems of the setup are currently being further investigated.